University of Alberta

ADC and T2 Response to Radiotherapy in a Human Tumour Xenograft Model

by

Matthew Penner Larocque

A thesis submitted to the Faculty of Graduate Studies and Research
in partial fulfillment of the requirements for the degree of

Doctor of Philosophy

in

Medical Physics

Department of Physics

Fall 2010

Edmonton, Alberta

Examining Committee

Dr. B. Gino Fallone, Physics & Oncology, University of Alberta

Dr. Alasdair Syme, Oncology, University of Alberta

Dr. Satyapal Rathee, Oncology, University of Alberta

Dr. Terence Riauka, Oncology, University of Alberta

Dr. Richard Marchand, Physics, University of Alberta

Dr. John Beamish, Physics, University of Alberta

Dr. L. John Schreiner, Physics & Oncology, Queen's University

Abstract

A 9.4 T magnetic resonance imaging (MRI) system was used to evaluate the response of a human tumour xenograft model to radiation therapy. The apparent diffusion coefficient (ADC) and the transverse relaxation time (T2) of human glioblastoma multiforme (GBM) tumour xenografts in NIH-iii nude mice were measured before, and at multiple points after, treatment of the tumours with 200 kVp x-rays. The response was characterized as a function of a number of variables of interest in the clinical treatment of cancer with external beam radiation therapy.

Mean tumour ADC and T2 responses after single fractions of radiation were investigated, with measurements being made until 14 days after treatment. Single fraction doses ranged from 50 cGy to 800 cGy. Fractionated treatments were used to deliver 800 cGy in two or three fractions with fraction spacings of 24 or 72 hours. The role of hypoxia on ADC and T2 response was investigated by using an externally-applied, suture-based ligature to induce a state of reduced oxygenation in tumours during treatment, after which ADC and T2 were measured using serial MRI. Finally, tumours were dissected in order to provide insight into possible pathophysiological mechanisms explaining the

observed responses. Tissue sections were prepared and reviewed by a pathologist.

This work adds to the body of literature describing tumour ADC and T2 response to anticancer therapy, and adds to the understanding of ADC and T2 response to radiation therapy in particular. This works supports that of others suggesting the use of ADC and T2 as potential biomarkers for tumour response to treatment.

Acknowledgements

I would like to acknowledge just some of the large number of people who have helped me during my time in grad school, and without whom the work in this thesis would not have been possible.

I would first like to thank my supervisors, Dr. B. Gino Fallone and Dr. Alasdair Syme. Both Gino and Alasdair both went above and beyond the call of duty in their roles as supervisors. Gino advocated for me, encouraged, taught, criticized when necessary, and gave me opportunities I could not have had otherwise. The influence of Alasdair on my research can hardly be understated. Alasdair discussed with me the big picture ideas and helped with the smallest of details, and together we celebrated victories big and small. My grad school experience would not have been nearly as enjoyable or rewarding without these two excellent supervisors.

Thank you to my supervisory committee, including Dr. Satyapal Rathee, Dr. Terry Riauka, Dr. John Beamish, and Dr. Richard Marchand, as well as Dr. L. John Schreiner of Queen's University who served as my external reader, all of whom provided several constructive comments and suggestions that improved and clarified many points in this thesis.

I was privileged to work with several collaborators including Dr. Joan Turner, Dr. Keith Wachowicz and Dr. Atiyah Yahya, Dr. Raymond Lai, and Dr. Jean Deschenes. In addition, I benefited from numerous other experts at the Cross Cancer Institute including Dan Doran from the medical physics technology management group, Dan McGinn and Gail Hipperson from the CCI vivarium, Bonnie Andrais from the cell culture lab, Gerry from the cell imaging facility, and Martine and Reanne from the pathology lab.

Sarah Derr, Cheryl Erickson, Jocelyn Martin, and Debbi Howorko made my life so much easier by helping me navigate the bureaucracies of the university and the hospital. The entire staff of the medical physics department, and particularly the graduate students of the department, who made grad school a great place to be – thank you.

I owe a huge debt to my family – my father, Richard, my mother, Janet, my brother Mike, and my friend, Rob, for their unconditional encouragement and support.

Finally, thanks to my loving fiancée, Andrée, who listened to me every day, constantly cheered me on, and shared in all of the highs and lows of my time as a graduate student. This would not have been possible without your help.

Table of Contents

List of Tables

List of Figures

List of Abbreviations

ADC	Apparent diffusion coefficient
BSF	Backscatter factor
BW	Bandwidth
CPMG	Carr-Purcell-Meiboom-Gill
CT	Computed tomography
dB	Decibels
DCE-MRI	Dynamic contrast enhanced magnetic resonance imaging
DW-SE	Diffusion-weighted spin-echo
EMF	Electromotive force
FID	Free induction decay
FOV	Field of view
GBM	Glioblastoma multiforme
GE	Gradient echo
GKS	Gamma Knife surgery

GUI	Graphical user interface
H&E	Hematoxylin and eosin
kVp	Peak kilovoltage
L+R	Ligation and radiation
LO	Ligation only
MR	Magnetic resonance
MRI	Magnetic resonance imaging
MRS	Magnetic resonance spectroscopy
MU	Monitor unit
NHL	Non-Hodgkin's lymphoma
NMR	Nuclear Magnetic Resonance
OER	Oxygen enhancement ratio
PAS	Periodic acid-Schiff
PAS+D	Periodic acid-Schiff diastase
PBS	Phosphate-buffered saline
PDD	Percent depth dose

RBC	Red blood cell
RECIST	Response evaluation criteria in solid tumors
RF	Radiofrequency
RIF	Radiation induced fibrosarcoma
RO	Radiation only
ROF	Relative output factor
RT	Radiation therapy
SE	Spin-echo
SGA	Sustained growth arrest
SNR	Signal-to-noise ratio
T1	Longitudinal relaxation time
T2	Transverse relaxation time
TE	Echo time
TMX	Theory-Model-Experiment
TR	Repetition time

Chapter 1: Overview

Apparent diffusion coefficient (ADC) and transverse relaxation time (T2) are two parameters which describe tissue being imaged using magnetic resonance imaging (MRI) techniques. Changes in both ADC and T2 have been shown to correlate with changes in tissue physiology following anticancer treatments. The work described in this thesis is based on a series of measurements of the ADC and T2 of tumours grown from human glioblastoma multiforme (GBM) cells implanted in mice. Measurements were taken before, and at multiple points after, radiation treatment. The dependence of these parameters on multiple aspects of treatment was investigated.

Chapter 2 provides the relevant background for the reading of this work, including an introduction to MRI (section 2.1), radiation therapy (section 2.5), theory relevant to ADC and T2 and how these parameters can be measured

using MRI (sections 2.3 and 2.4). A thorough review of the literature pertaining to the measurement of ADC and T2 in clinical subjects (section 2.6.2) and in animal models (section 2.6.3) is given.

Chapter 3 outlines the specific techniques used in this work, including details of the animal model of cancer used (section 3.1), specifics of how MRI images were acquired and analyzed (sections 3.2-3.5), and how radiation therapy was delivered to the tumours (section 3.6).

Subsequent chapters describe a series of related studies which have either been published after peer-review, or are currently in preparation for review. Portions of these publications have been reproduced in these chapters. Chapter 4 describes the behavior of ADC and T2 after various doses of single-fraction radiotherapy, with attention paid to the temporal and dose dependence of the observed responses. These results have been published (1). Chapter 5 extends this work to cases of fractionated radiotherapy, and compares the responses to multiple fractionation schemes. These results have also been published (2). In chapter 6, hypoxia is induced in tumours during radiotherapy treatment, creating a change in the radiosensitivity of tumours of the same cell line, and the relative responses of ADC and T2 are investigated further. These results have been accepted for publication (3). Finally, in chapter 7, observations from tumours sacrificed for histology are reported, and correlations between ADC and T2 responses and histological changes are discussed. The results of

chapter 7 are currently being prepared for submission for peer-review (4). Chapter 8 summarizes the conclusions of this work.

References

1. Larocque MP, Syme A, Yahya A, Wachowicz K, Allalunis-Turner J, Fallone BG. Temporal and dose dependence of T2 and ADC at 9.4 T in a mouse model following single fraction radiation therapy. *Med. Phys.* 2009: p. 2948-2954.

2. Larocque MP, Syme A, Yahya A, Wachowicz K, Allalunis-Turner J, Fallone BG. Monitoring T2 and ADC at 9.4 T following fractionated external beam radiation therapy in a mouse model. *Phys. Med. Biol.* 2010: p. 1381-1393.

3. Larocque MP, Syme A, Allalunis-Turner J, Fallone BG. ADC response to radiation therapy correlates with induced changes in radiosensitivity. *In press.*

4. Larocque MP, Syme A, Lai R, Allalunis-Turner J, Fallone BG. Histological findings correlated with ADC and T2 responses to radiotherapy. *In preparation.*

Chapter 2: Background

This chapter introduces the background information necessary for interpretation of the dissertation to follow. The chapter begins by giving an introduction to and classical overview of magnetic resonance imaging (MRI) in section 2.1. The role of MR in oncology is then discussed (section 2.2), with an emphasis on the use of MR in monitoring the response of tumours to therapy. Sections 2.3 and 2.4 introduce apparent diffusion coefficient (ADC) and transverse relaxation time (T2), which are frequently measured during the experiments described in this dissertation. These sections include an introduction to the nature and meaning of ADC and T2, followed by how that parameter can be quantitatively measured using MR techniques. Section 2.5 provides relevant background on radiation therapy. The chapter concludes by giving an in-depth review of the scientific literature related to the study of T2 and/or ADC changes in response to anticancer treatments (section 2.6).

2.1 Magnetic resonance imaging

The phenomenon of nuclear magnetic resonance (NMR) was independently discovered in 1946 by Felix Bloch and Edward Purcell, for which they shared the 1952 Nobel Prize for Physics. NMR was promptly developed by the chemistry and physics communities to study the structure of molecules. In the 1973, Paul Lauterbur published the first MRI image using linear gradient fields (1). Peter Mansfield made a major contribution to MRI by developing the Fourier-based imaging techniques most commonly used today. Lauterbur and Mansfield shared the 2003 Nobel Prize in Physiology or Medicine.

Raymond Damadian, another early developer of MRI, made the important observation that normal and malignant tissues have different relaxation rates (2), and eventually built the first full-body prototype MRI scanner. Damadian, and others on his behalf, vigorously protested his exclusion from the shared 2003 Nobel Prize.

Today, MRI scanners are an extremely powerful, non-invasive method of obtaining 3D images from inside the human body, with wide ranging applications in the field of medicine.

The principles of MRI are described in great detail in a large number of textbooks. Two in particular were drawn on heavily in the writing of this chapter. For the fundamentals of the MR system and the behavior of magnetic

spins, *Principles of Magnetic Resonance Imaging* (3) by Nishimura is an excellent resource, and on the details of image acquisition and pulse sequences *Handbook of MRI Pulse Sequences* (4) by Bernstein, King, and Zhou is encyclopedic.

2.1.1 Basic MR system

The basic components of an MR system are shown in Figure 2.1. There are three independently-operating sets magnetic fields, generated by sets of electromagnetic coils, whose purposes are described in subsections 2.1.2-2.1.4. The most powerful of the fields is generated by a superconducting magnet and is known as the main magnetic field, or B_0. The two other sets of fields are generated by coils that generally operate at room temperature and are associated with amplifiers which amplify the pulses of current into the coils. A digital receiver is in place to digitize the signal acquired by the system. Finally, there is an operator console which controls the operation of the MRI system. The specifics of the MRI system used for the work described in this dissertation are described in section 3.2.

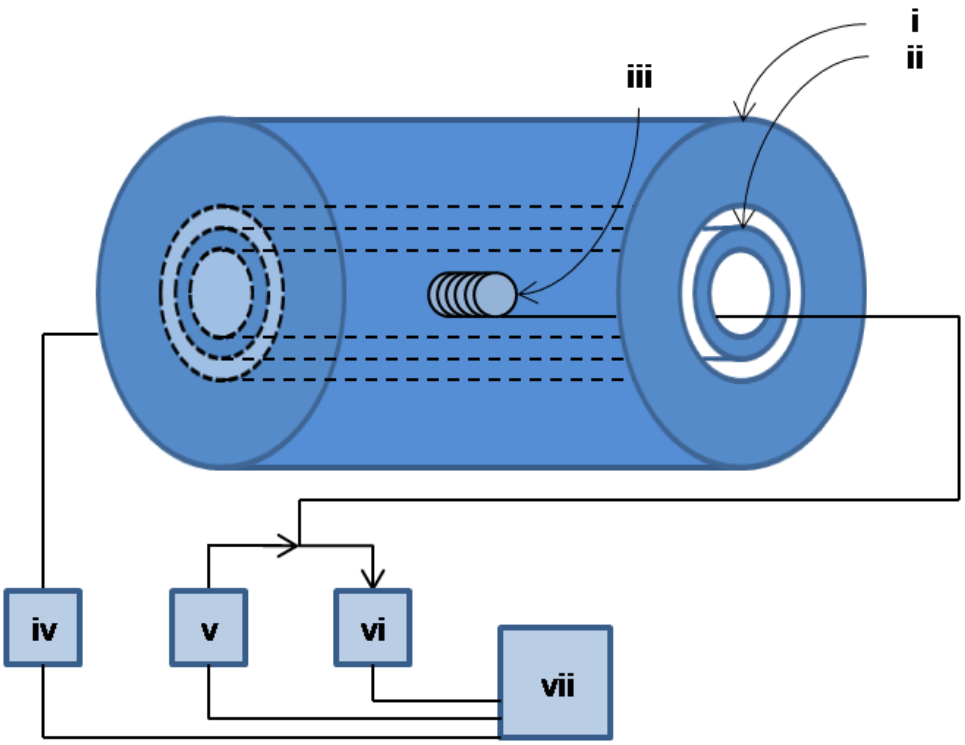

Figure 2.1. Diagram showing principal components of an MRI system: superconducting magnet (i), gradient set (ii), RF coil (iii), gradient amplifiers (iv), RF amplifier (v), RF receiver (vi), and MR console (vii).

2.1.2 Main field B_0, magnetization and precession

Nuclei possessing an odd number of protons and/or an odd number of neutrons are MR-viable, because they have spin angular momentum **S**. In descriptions of MRI, MR-viable nuclei are referred to as *spins*. Nuclei with spin angular momentum have a proportional nuclear magnetic moment **μ** given by

$$\boldsymbol{\mu} = \gamma \mathbf{S}, \tag{2.1}$$

where γ is known as the gyromagnetic ratio, which is different for different nuclei.

In a non-ferromagnetic sample, such as tissue, when no external magnetic field is present the magnetic moments of a body of spins are randomly oriented and there is no net macroscopic magnetic moment. When an external magnetic field is applied, such as the static main magnetic field B_0 of an MRI magnet, there is a potential energy E associated with each nuclear magnetic moment given by

$$E = -\boldsymbol{\mu} \cdot \mathbf{B} = -\mu_{\mathbf{Z}} B_0 = -\gamma S_z B_0, \tag{2.2}$$

where *z* is the direction of the magnetic field of the MRI system, known as the longitudinal direction, and μ_Z is the component of the nuclear magnetic moment that is parallel to the direction of the main magnetic field. The most commonly used B_0 field strengths in clinical practice are 1.5 T and 3.0 T. The *xy* plane perpendicular to the axis of this field is known as the transverse direction. For the ^{1}H atom, which is the most commonly used in MRI, S_Z is quantized to $\pm\hbar/2$. This translates to nuclei in one of two energy states – one lower energy state with S_Z parallel (n_+) to the applied magnetic field and one higher energy state with S_Z antiparallel (n_-) to B_0. The ratio of nuclei populating each state is given by the Boltzmann distribution

$$n_-/n_+ = e^{-\Delta E/kT} = e^{-\gamma\hbar B_0/kT}, \tag{2.3}$$

where k is Boltzmann's constant and T is the absolute temperature. The excess spins in the lower energy state result in a net macroscopic magnet moment **M** parallel to the applied magnetic field whose magnitude M_0 is given by

$$|\boldsymbol{M}| = M_0 = \frac{N\gamma^2\hbar^2 B_0}{4kT}, \tag{2.4}$$

where N is the volume density of spins. At equilibrium **M** aligns parallel to **B**. When not parallel to **B**, **M** experiences a torque τ from **B** given by

$$\boldsymbol{\tau} = \mathbf{M} \times \mathbf{B} = \frac{d\mathbf{L}}{dt}, \tag{2.5}$$

where d**L**/dt is the rate of change in angular momentum. Multiplying both sides by γ gives

$$\frac{d\mathbf{M}}{dt} = \mathbf{M} \times \gamma\mathbf{B}, \tag{2.6}$$

for which the solution is for **M** to precess about **B** with a frequency f given by

$$f_0 = \gamma B_0. \tag{2.7}$$

This frequency is known as the Larmor frequency. From equation 2.7, we see that the gyromagnetic ratio γ is so named because it is the ratio of the precessional frequency to the applied magnetic field for a particular nuclear species.

2.1.3 Radiofrequency (RF) field B_1 and RF excitation

Precessional motion is essential for measurement of an MRI signal. If there is a net transverse component of the bulk magnetic moment and there is

an RF coil tuned to the Larmor frequency placed near the MR sample, there will be an electromotive force (EMF) induced in the coil due to the changing magnetic flux caused by the precession of spins. This is the basic signal of an MRI experiment and is known as a free induction decay (FID).

The RF coil used for detection of the signal can also be used to perturb the net magnetization from its equilibrium position parallel to B_0 and make a transverse component available for detection. When an oscillating current at the frequency f_0 is driven through the coil, a time-varying transverse magnetic field is generated, denoted $\mathbf{B_1(t)}$. This applies a torque on **M** and tilts it away from its equilibrium position. By including $\mathbf{B_1(t)}$ in equation 2.6, it can be shown that the angular displacement of **M** (termed flip angle) is given by:

$$\theta = \gamma \int B_1 dt. \tag{2.8}$$

After the B_1 field is switched off, in general there will now be a transverse component to **M**, rotating at the Larmor frequency, f_0. This is not true in the special case where θ is a multiple of 180°, where **M** will be either parallel or antiparallel to *z*. It is common to use a flip angle of 90°, where the magnitude of the transverse component will be maximum (M_0), with no longitudinal component.

Figure 2.2(a) is a diagram depicting the rotation of this transverse component. The description of the system may be simplified by adopting a rotating reference frame at the Larmor frequency, also shown in Figure 2.2(b).

In this frame of reference, both $\mathbf{B_1}$ and the transverse component of **M** become non-rotating.

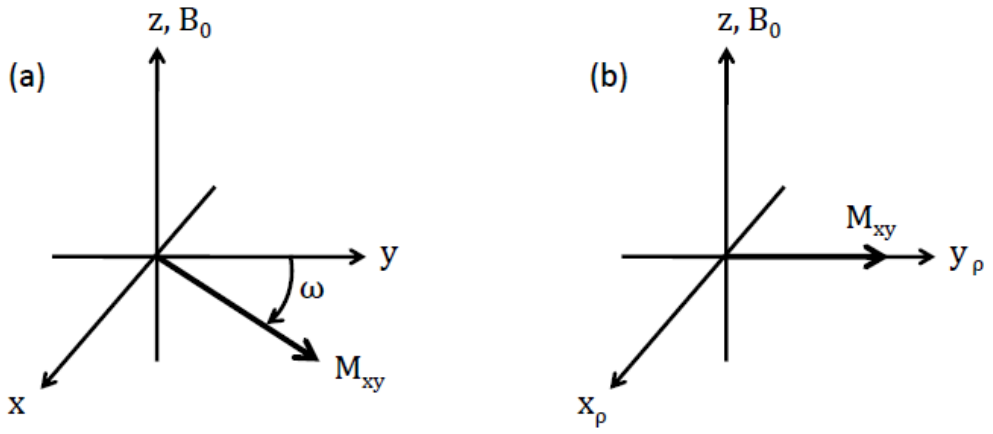

Figure 2.2. Diagram depicting the component of $\vec{M}$ perpendicular to the applied magnetic field B_0. M_{xy} rotates about z with at the Larmor frequency (a). M_{xy} does not rotate relative to an adopted rotating reference frame (b).

2.1.4 Gradient field G and selective excitation

If $\mathbf{B_1}$ is uniform over the entire sample, the resulting excitation will be uniform across the entire sample. For imaging purposes, it is desirable to be able to only selectively excite a controlled portion of the sample. Selective excitation of a slab of spins in a sample is known as "slice selection" and is used to isolate a single slice through a sample for imaging.

This is achieved by employing a third magnetic field (in addition to $\mathbf{B_0}$ and $\mathbf{B_1}$). This is a field that varies linearly in strength as a function of position and is called a gradient field, **G**. MR systems are equipped with electromagnetic coils which can generate gradient fields along the directions of the coordinate axes of the MR system, and can be combined vectorally to produce a gradient in an arbitrary direction. When **G** is applied in a particular direction, there is a resulting gradient in precessional frequencies along the same direction. When **G** is applied along the *z* direction, for example, equation 2.7 is transformed to become:

$$f_{eff} = \gamma B_{eff} = \gamma[B_0 + G(z)] = f_0 + \gamma G(z). \quad (2.9)$$

If an RF pulse of narrow bandwidth BW_{RF} is delivered while **G** is applied, only a narrow band of frequencies will be excited, corresponding to a thin slice of spins orthogonal to the applied direction of **G**, with the centre of that slice determined by the resonant frequency of the RF pulse. The slice thickness is given by

$$\Delta z = BW_{RF} / \gamma G_z, \quad (2.10)$$

where G_z is the spatial rate of change of **G** in mT/m along the z direction. This is known as the gradient strength, and is what is typically varied to achieve desired slice thickness. The slice profile is determined from the Fourier transform of the RF pulse. Typically, a "sinc" pulse, or some variation thereof, is used, as it produces a near rectangular profile. Although an infinitely-long sinc pulse would

produce a rectangular profile, in reality the duration of the pulse is limited. Truncation of the sinc pulse results in ringing in the slice profile. In practice, a smoothing filter may be applied to the RF pulse to reduce these types of artifacts. Two sample RF pulse envelopes and the resulting slice profiles are shown in Figure 2.3.

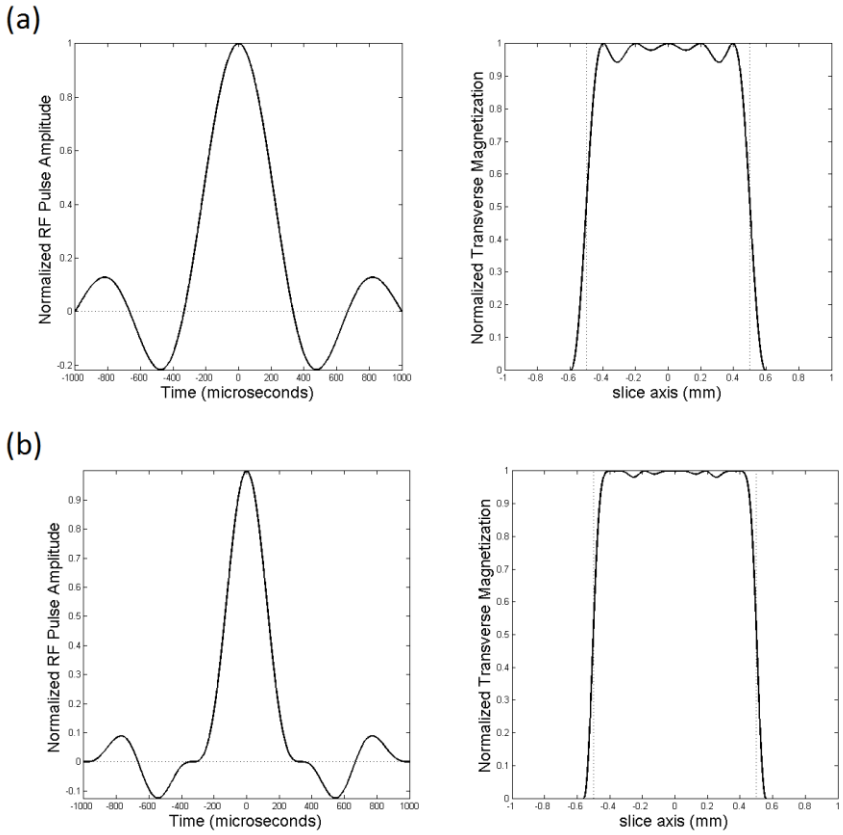

Figure 2.3. RF pulse shapes and resulting slice profiles. A 5-lobe sinc pulse produces an approximately rectangular slice profile with some ringing (a). Addition of a Hanning-filter to the sinc pulse reduces ringing and produces sharper slices edges (b). Amplitudes of RF pulse height and resulting magnetization are individually normalized.

2.1.5 Frequency and phase encoding

After excitation of a slice, knowledge of the spatial distribution of available transverse magnetization $m_{xy}(x,y)$ is required. This is achieved by the processes of frequency and phase encoding. As the terms imply, spatially-dependent frequency and phase differences are imparted to the spins within the excited sample. As will be shown, if this encoding is done in a particular manner, $m_{xy}(x, y)$ can be recovered from the 2D inverse Fourier transform of the acquired signal.

The process of frequency encoding is intuitively accessible. After slice selection, a gradient of strength G_x (typically on the order of 10-50 mT/m) is applied and signal is acquired during the length of the gradient pulse, t_{AQ} (typically on the order of ms). This signal s(t) will consist of a superposition of signals from all available magnetization in the transverse plane, with the frequency of each signal being dependent on its position along the x-axis, as given by

$$s(t) = \int m_{xy}(x) \cdot e^{-i\gamma G_x x t} \cdot dx, \tag{2.11}$$

in the rotating reference frame. It is possible to calculate $m_{xy}(x)$ from s(t) using

$$m_{xy}(x) = \gamma G_x \int s(t) \cdot e^{+i\gamma G_x x t} \cdot dt, \tag{2.12}$$

which is the scaled inverse Fourier transform of s(t) multiplied by a scaling factor (γG_x). This is the projection of m_{xy} along the x-axis.

A schematic diagram of the pulses used to produce an MR signal is known as a "pulse sequence diagram". A pulse sequence diagram used to produce the signal in equation 2.11 is shown in Figure 2.4.

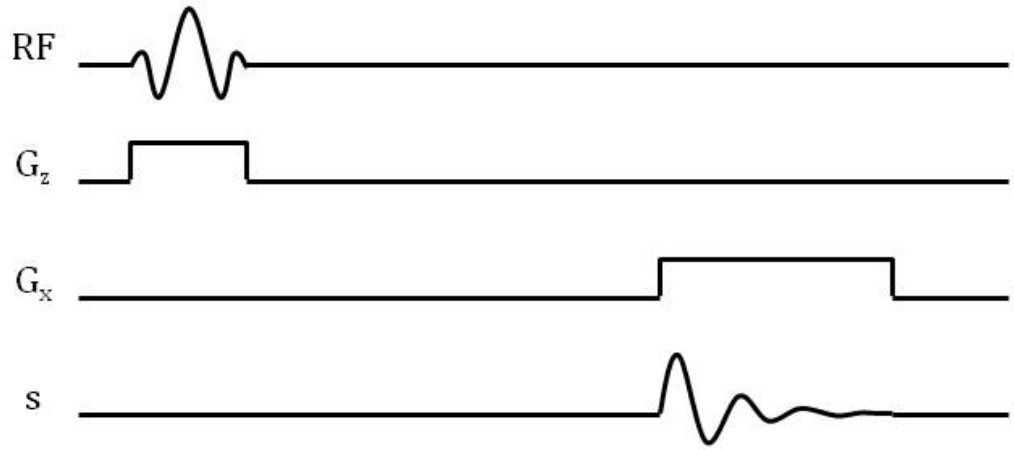

Figure 2.4. Pulse sequence showing RF pulse shape (RF) with slice selection gradient (G_z) applied, followed by frequency encoding gradient (G_x) applied during acquisition of signal (s).

Phase encoding is accomplished by adding a gradient pulse between slice selection and frequency encoding, in the direction orthogonal to the slice select and frequency encoding gradients. This pulse is of fixed length τ (typically on the order of ms), and no signal is acquired while it is turned on. This pulse has the effect of temporarily altering the precessional frequencies of spins in the excited slab in a spatially dependent manner, during which time the spins accumulate a phase angle φ given by

$$\varphi(y) = \gamma G_y y \tau, \tag{2.13}$$

where y is the direction of the phase encoding gradient. It is important to note that it is not possible to encode frequency and phase at the same time. If the frequency and phase encoding gradients are left on at the same time, the effect is not to encode both directions at once, but rather to measure a diagonal projection through the slice, with the vector sum of the two gradients effectively acting as a single frequency encoding pulse. While frequency encoding is done with constant gradient amplitude and sampling the signal over time, phase encoding is done by keeping the duration of the phase encoding gradient fixed, and performing iterative experiments with the amplitude of phase encoding gradient increased in fixed increments. The initial phase encoding gradient is usually applied in one direction, with subsequent gradients incrementally increased such that the final phase encoding gradient is of equal magnitude but opposite direction as the first. A sample pulse sequence diagram containing phase encoding gradients is shown in Figure 2.5.

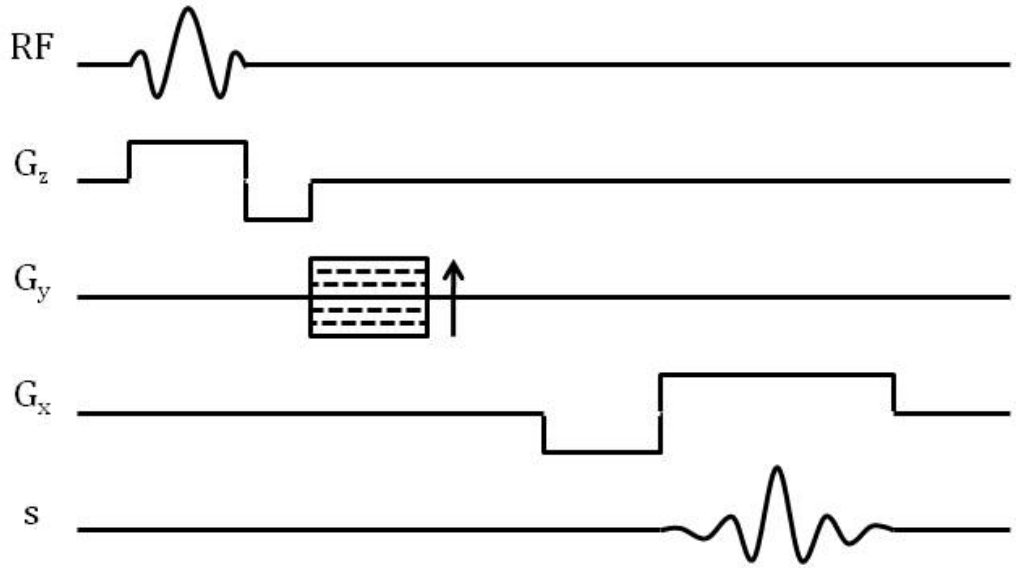

Figure 2.5. Pulse sequence showing RF pulse shape (RF) with slice selection gradient (Gz) applied, followed by a phase encoding pulse (Gy), followed by frequency encoding gradient (Gx) applied during acquisition of signal (s). The dashed lines and arrow are meant to indicate that multiple experiments are performed, with the amplitude of the phase encoding pulse increased by a fixed increment with each new experiment.

As well as the inclusion of a phase encoding pulse in Figure 2.5, two additional lobes are added. A slice-rephasing gradient is added immediately after the slice-selection gradient. This has an area of ½ the slice-selection gradient and counteracts phase dispersion of the transverse magnetization that occurs while the slice-selection gradient is on. A prephasing gradient is added immediately before the frequency encoding gradient. This has the effect of centering the FID during the acquisition window, which allows for more efficient sampling of the signal.

If the above pulse sequence is played out, the signal acquired will be described by

$$s(t) = \iint m_{xy}(x,y) \cdot e^{-i\gamma G_x x t} \cdot e^{-i\gamma G_y y \tau} \cdot dx \cdot dy, \tag{2.14}$$

which is known in MRI as the "signal equation". It is common to adapt what is known as "k-space" formalism where the following substitutions are made:

$$k_x(t) = \gamma G_x t, \tag{2.15}$$

and

$$k_y(G_y) = \gamma G_y \tau, \tag{2.16}$$

resulting in a simplified signal equation given by

$$s(t) = \iint m_{xy}(x,y) \cdot e^{-i(k_x x + k_y y)} \cdot dx \cdot dy, \tag{2.17}$$

where k_x and k_y are in units of spatial frequency. Equation 2.17 implies that s(t) is the 2D Fourier transform of $m_{xy}(x,y)$, and an image of the transverse magnetization can be reconstructed by taking the inverse Fourier transform of acquired signal:

$$m_{xy}(x,y) = \iint s(k_x, k_y) \cdot e^{+i(k_x x + k_y y)} \cdot dk_x \cdot dk_y. \tag{2.18}$$

The objective of MR imaging is to sufficiently sample the two-dimensional parameter space composed of k_x and k_y, known as k-space, in order to be able to faithfully reconstruct the object being imaged. This space is schematically represented in Figure 2.6. Each acquisition during a pulse of the frequency

encoding gradient samples one line of k-space parallel to k_x, with separation between samples Δk_x, given by:

$$\Delta k_x = \gamma G_x \Delta t = \gamma G_x / BW_{samp}, \quad (2.19)$$

where Δt is the time between samples and BW_{samp} is the sampling bandwidth used during acquisition of the signal. With successive acquisitions, the amplitude of the phase-encoding pulse is incremented so that successive lines through k-space are separated by Δk_y, given by:

$$\Delta k_y = \gamma \Delta G_y \tau, \quad (2.20)$$

where τ is the constant length of the phase-encoding gradient, and ΔG_y is the amplitude increment of successive phase-encode pulses.

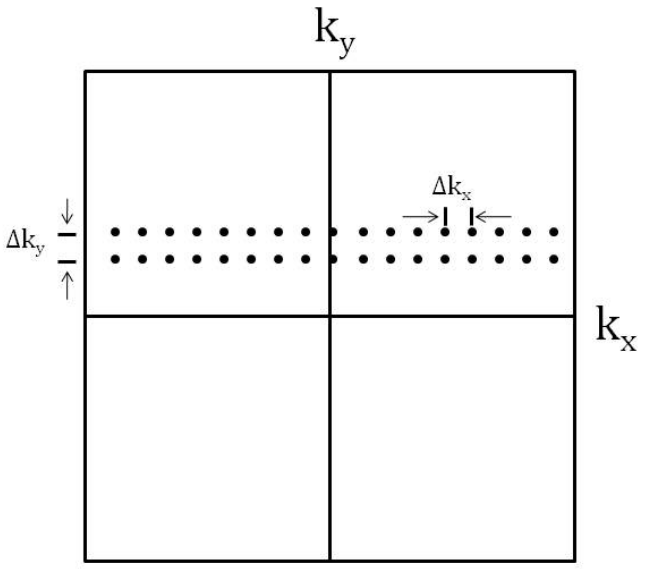

Figure 2.6. Schematic diagram of a partially sampled k-space, showing sampling of two lines. The sample spacings in k_x and k_y are highlighted.

Figure 2.7 shows a fully sampled k-space and the corresponding transverse image through a test tube filled with water.

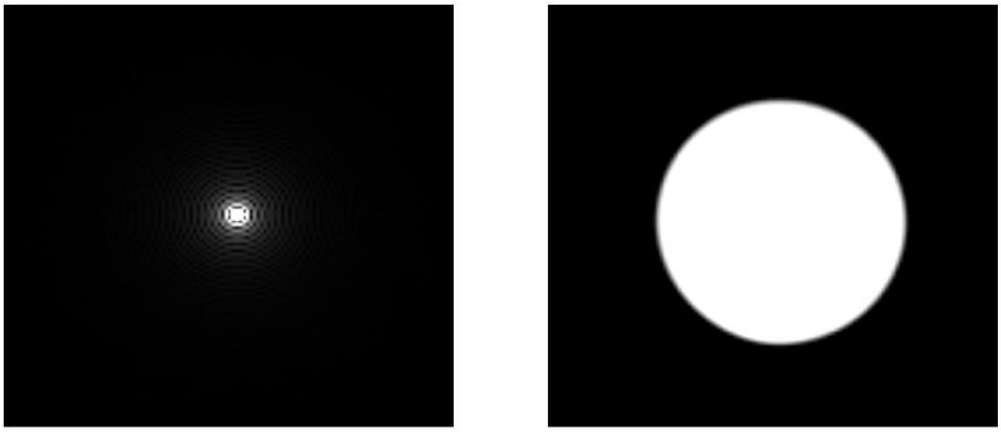

Figure 2.7. Sample k-space data (left) and corresponding image (right). The image is a transverse slice through a test tube filled with water.

2.1.6 k-space sampling requirements

The Nyquist sampling theorem says we must digitize the signal at a rate greater than or equal to twice the maximum frequency in the sample, in order to avoid aliasing artifacts. This is applicable in both the frequency and phase encoding directions. If the maximum width of the object we wish to image is the field of view (FOV), then

$$\frac{-\gamma \cdot G \cdot FOV}{2} \leq f_{max} \leq \frac{+\gamma \cdot G \cdot FOV}{2}. \tag{2.21}$$

The requirement on the sampling bandwidth BW_{samp} will then be

$$BW_{samp} \geq \gamma \cdot G \cdot FOV. \tag{2.22}$$

In the phase encoding direction, the same criteria requires

$$\Delta G \geq 1/\gamma \cdot \tau \cdot FOV. \quad (2.23)$$

Image resolution is also affected by sampling. The pixel size in both directions will be inversely proportional to the number of points sampled in the corresponding k-space directions:

$$\Delta x = FOV/N_{freq}. \quad (2.24)$$

and

$$\Delta y = FOV/N_{phase}. \quad (2.25)$$

Finally, while insufficient sampling rate can lead to aliasing artifacts, insufficient sampling extent can lead to ringing artifacts. If k-space is not sampled to sufficient range, higher spatial frequencies are not sampled and truncation at the edges of the sampled domain translates to ringing in the reproduced image. In practice, the necessary range can be determined experimentally, and k-space processing techniques can be used to reduce the magnitude of this artifact.

2.1.7 Relaxation and image contrast

At this point, the selective excitation and acquisition of an image of the available transverse magnetization $m_{xy}(x,y)$ in a single slice through an object has been described. It is differences in m_{xy} which produce contrast in MR images.

Immediately after a single RF excitation pulse, there will be a magnetization distribution $m_{xy}(x,y,t=0)$ proportional the volumetric density of spins, ρ(x,y), often referred to as proton density. In conventional MRI, these spins are ^1H molecules and tissues with high water or lipid content generally have relatively high ρ.

After the initial perturbation, the net magnetization will tend to return to its equilibrium position parallel to B_0, in a process known as relaxation. Recovery of the longitudinal magnetization $M_z(t)$ is called longitudinal relaxation, while the decay of transverse component $M_{xy}(t)$ is known as transverse relaxation.

Recovery of longitudinal magnetization is described by

$$M_z(t) = M_0 + [M_z(0) - M_0] \cdot e^{-t/T1}, \tag{2.26}$$

where T1 is known as the longitudinal relaxation time. T1 is also called the spin-lattice relaxation time, as this recovery is due to exchange of energy between spins and the surrounding lattice, which moves the perturbed system back to thermal equilibrium.

Decay of transverse magnetization is described by

$$M_{xy}(t) = M_{xy}(0) \cdot e^{-t/T2}, \tag{2.27}$$

where T2 is known as the transverse relaxation time. T2 is also known as the spin-spin relaxation time. T2 decay is caused by energy exchange between spins, which leads to a broadening of the distribution of resonant frequencies within a

given volume. This broadening results in dephasing of the spins, and decay of the signal.

Additional dephasing of spins and decay of M_{xy} is caused by static inhomogeneities in the magnetic field. If this were the only effect, the decay would be characterized according to the decay time T2'. The decays characterized by T2 and T2' are active together, for a decay with a composite characteristic time T2*, given by

$$\frac{1}{T2^*} = \frac{1}{T2} + \frac{1}{T2'}. \tag{2.28}$$

It can be shown that the dephasing due to static inhomogeneities can be reversed by application of a 180° refocusing RF pulse centered between the excitation pulse, and the acquisition window. With the addition of a refocusing pulse to the sequence shown in Figure 2.5, the sequence becomes known as a spin-echo (SE) pulse sequence, shown in Figure 2.8, and the acquired signal is known as a spin-echo. The time from the centre of the excitation pulse to the centre of the spin-echo is known as the echo time (TE).

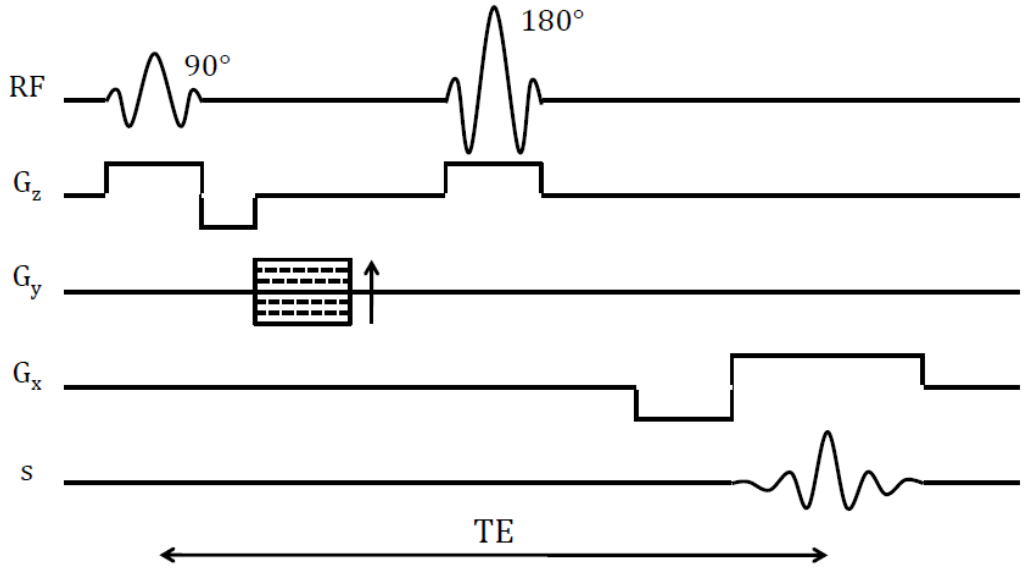

Figure 2.8. Typical spin-echo pulse sequence, showing a 90° excitation pulse, a phase encoding lobe, a 180° refocusing pulse, frequency encoding lobe, and acquired echo. Note the amplitude of the refocusing pulse is double that of the excitation pulse, achieving twice the flip angle.

After a single excitation pulse with flip angle θ followed by a refocusing pulse, the value of M_{xy} at the time of acquisition (TE) will be given by

$$M_{xy}(TE) = M_z(0) \cdot \sin\theta \cdot e^{-TE/T2}, \tag{2.29}$$

where $M_z(0)$ represents the longitudinal magnetization immediately *before* the excitation pulse. If the sequence is repeated at a later time TR, the longitudinal relaxation available to be excited will be given by

$$M_z(TR) = M_0 + [M_z(0) \cdot \cos\theta - M_0] \cdot e^{-TR/T1}, \tag{2.30}$$

where $M_z(0)$ is the longitudinal magnetization immediately before the first excitation pulse. The time between sequence repetitions is known as the repetition time (TR). After several repetitions of the sequence, the value of M_{xy} at time TE after an excitation pulse will reach a steady-state. This can be shown to be

$$M_{xy}(steady\ state) = \frac{M_0\left(1 - e^{-TR/T1}\right) \cdot \sin\theta}{1 - \cos\theta \cdot e^{-TR/T1}} \cdot e^{-TE/T2}. \quad (2.31)$$

Using equation 2.31, the expected contrast between any two tissues can be calculated for a given pulse sequence, assuming the values of T1 and T2 are known for each. Figure 2.9 shows the contrast between two hypothetical tissues (tissue A: T1 = 1500 ms, T2 = 60 ms; tissue B: T1 = 1300 ms, T2 = 55 ms) with equal proton density as a function of TE and TR. A spin-echo sequence with a 90° flip-angle is assumed for the purposes of the calculation. The figure shows two distinct regions of high contrast. The region of low TE and low TR shows what is known as T1-weighted contrast, where the contrast is primarily due to T1-differences between the tissues. The region of longer TE and long TR shows T2-weighted contrast, where contrast is primarily due to T2-differences between tissues. If differences in proton density were to exist, a sequence employing the longest TR and shortest TE possible would be best to generate contrast based on these differences.

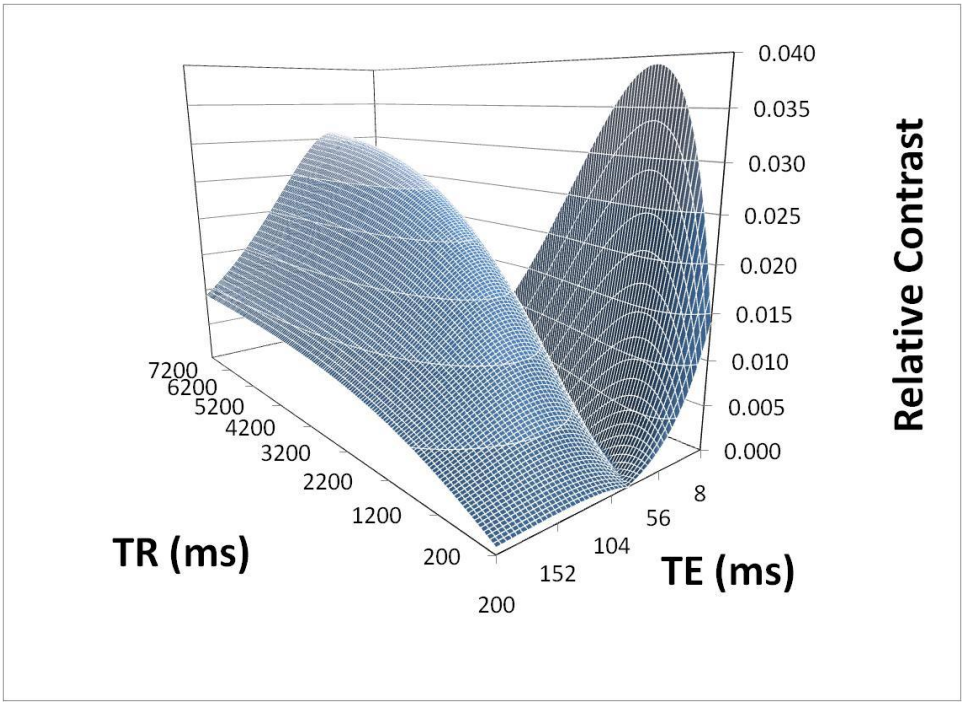

Figure 2.9. Plot of relative contrast between two hypothetical tissues as a function of TR and TE. One tissue has a T1 of 1500 ms and a T2 of 60 ms, and the other a T1 of 1300 ms and a T2 of 55 ms. It is assumed that the two tissues have equal proton density. Additionally, a spin-echo sequence with a 90° flip-angle is assumed.

2.1.8 SNR considerations

In addition to image contrast, image signal-to-noise ratio (SNR) is an important consideration for MRI. In addition to pulse sequence parameters such as flip angle, TE, and TR, a major factor in determining the SNR of an image is the strength of the main magnetic field B_0. From equation 2.7, we see that the resonant frequency f_0 increases proportional to increases in B_0. The EMF induced in the receiving RF coil is proportional to the rate of change of magnetic flux, which is proportional to resonant frequency:

$$\mathrm{EMF} = -\frac{\mathrm{d}\Phi}{\mathrm{dt}} \propto \mathrm{f}_0 \propto \mathrm{B}_0. \tag{2.32}$$

From equation 2.4, the amount of available magnetization is also linearly dependent on field strength. Finally, it is common practice in MRI to perform multiple imaging experiments and average the results to improve signal to noise ratio, with signal adding linearly with the number of averages N_{avg}. It can be shown that the available signal is

$$\mathrm{S} \propto \mathrm{f}_0 \cdot \mathrm{M}_0 \cdot \mathrm{N}_{\mathrm{avg}} \cdot \Delta\mathrm{x} \cdot \Delta\mathrm{y} \cdot \Delta\mathrm{z}, \tag{2.33}$$

where Δx, Δy, and Δz are the voxel dimensions; both f_0 and M_0 are proportional on B_0, leading to a B_0^2 signal dependence.

The dominant noise source in MRI is thermal noise present in the sample being imaged. The frequency spectrum of this noise is flat, due to the randomness of thermal motion. The standard deviation of the noise acquired from the body can be shown to be proportional to f_0. The contribution of this noise to the acquired signal is dependent on how the signal is sampled. As the sampling bandwidth (BW_{samp}) is widened, more noise is acquired and it can be shown the standard deviation of the noise grows proportional to $\sqrt{BW_{samp}}$. It can also be shown that when a signal undergoes the Fourier transform, the noise in the resulting image will be reduced by a factor of $\sqrt{N_{samp}}$ relative to the time domain signal, where N_{samp} is the number of samples in the original signal. Finally, when averaging experiments, although signal adds linearly, noise is not

correlated and only increases proportional to $\sqrt{N_{avg}}$. It can be shown that noise is:

$$\text{Noise} \propto f_0 \cdot \sqrt{BW_{samp} \cdot N_{avg} / (N_{freq} \cdot N_{phase})}. \quad (2.34)$$

Combining equations 2.33 and 2.34, SNR can be shown to have the following dependencies:

$$SNR \propto M_0 \cdot \Delta x \cdot \Delta y \cdot \Delta z \cdot \sqrt{N_{freq} \cdot N_{phase} \cdot N_{avg} / BW_{samp}}. \quad (2.35)$$

The linear dependence of M_0 on B_0 means SNR increases linearly with field strength. For this reason, MRI systems have been made available at higher and higher field strengths.

Use of high field does have drawbacks. These include increased artifacts from susceptibility differences at tissue interfaces and increased tissue heating from deposited RF energy. Although these problems can be overcome (for example, increasing BW_{samp} reduces susceptibility artifacts but reduces SNR), optimization of sequences is dependent on field strength and is an area of active study.

2.2 Role of MR in oncology

One of the first motivations for the development of MRI systems was the observation of different relaxation times between normal and tumor tissue during early NMR experiments (2). MRI plays an important role in the detection,

treatment, and monitoring of cancer. MRI is being tested as a cancer screening tool (5,6) and continues to play an evolving role in the detection, diagnosis, and staging of many cancers, including those of the brain (7), breast (8,9), rectum (10), and prostate (11,12). Inspired by the superior soft-tissue contrast offered by MRI over computed tomography (CT) methods, recent work has shown that MRI is a viable modality for the simulation of radiation therapy (13). Basic MR methods have been expanded to provide many tools for observing the behavior of tumors post-therapy (14,15).

Conventional imaging to assess therapeutic response based on volume changes is limited by the timeframe over which these changes occur. This in turn places a limit on the utility of this technique to guide patient therapy at an early stage of treatment (14-16). In addition to conventional imaging, a diverse selection of MRI techniques have been used to monitor the growth and treatment response of tumors to various therapies both in the laboratory and in the clinic. These techniques include the use of targeted contrast agents (17) (18), ^{1}H magnetic resonance spectroscopy (MRS) used to monitor the relative concentrations of metabolites in both tumor and surrounding tissue, and ^{31}P MRS which can be used to directly monitor the metabolic and pH status of the tumor and the surrounding microenvironment (19).

The quantitative measurement of relaxation times and water diffusion has been shown to be a powerful method of assessing tumor behavior and

evaluating the performance of different therapeutic approaches. A thorough review of the literature relating to the study of T2 and ADC as potential biomarkers of treatment response is given in section 2.6.

2.3 Diffusion

2.3.1 Theory

Diffusion is the net movement of particles down a concentration gradient due to Brownian motion. The diffusion coefficient D is a proportionality constant between a concentration gradient $d\Phi/dx$ along a particular direction and the resulting diffusion flux J. This relationship, given by equation 2.36, is known as Fick's first law of diffusion:

$$J = -D \cdot \frac{d\Phi}{dx}. \tag{2.36}$$

Diffusion coefficient is a property of a medium specific to a particular molecule. In MRI applications, the diffusion coefficient of water in different tissues is often of interest. The effect of diffusion on MR experiments has long been known, and initially presented itself as a confounding factor in attempts to measure T2 (20,21). Molecular diffusion during the application of imaging gradients was resulting in attenuated signal, which effected early measurements of T2.

When a gradient G is applied, the resonant frequencies of spins in the sample are altered and they accumulate a spatially-dependent phase φ, given by

equation 2.13 (this effect is exploited in the phase-encoding process). This expression can be generalized such that φ is given by

$$\varphi = \gamma \cdot \int_0^T \boldsymbol{G}(t) \cdot \boldsymbol{r}(t) \cdot dt \,, \tag{2.37}$$

where **r**(t) is the position of the spins. Here, the motion of spins during the duration of the gradient pulse is accounted for. When this motion is coherent this can be exploited, such as in the case of vascular flow where this effect is used for the purposes of phase-contrast angiography (4). When this motion is incoherent, such as in the case of molecular diffusion, the distribution of phase throughout the sample results in destructive interference and the MRI signal S is attenuated. It can be shown that the S is given by

$$S = S_0 \cdot e^{-bD}, \tag{2.38}$$

where b is known as the b-value and is given by

$$b = \gamma^2 \cdot \int_0^{TE} \left[\int_0^t \boldsymbol{G}(t') \cdot dt' \right]^2 \cdot dt. \tag{2.39}$$

The integral in equation 2.39 sums the contribution of phase dispersion from all gradients in a given sequence. Most imaging sequences are designed so that imaging-related pulses have little or no net contribution to b, and so deliberate diffusion-sensitizing pulses may be used when diffusion-weighting is desired (see section 2.3.2).

Theoretical models predict (22) and experiments have shown (23) that diffusion may not be isotropic in certain tissues. In the case of some tissues,

such as nervous or fibrous tissue, the anisotropy can be significant. Although mapping of this anisotropy is of interest in some applications, measurements of D are typically made in three orthogonal directions, and the results averaged to yield a value of ADC:

$$ADC = \frac{D_x + D_{y+} D_z}{3}. \quad (2.40)$$

The ADC is a non-directional measure of the freedom for diffusion to take place in a particular environment. The word "apparent" is retained to keep this quantity distinct from D, and to emphasize that ADC is sensitive to measurement technique. Any measurement of ADC with MR is effectively an estimate sensitive to the RMS diffusion distance of spins in the sample, not a direct measurement of diffusion coefficient. Tissue ADC is known to be sensitive to cellular size, extracellular volume, membrane permeability, and temperature (24).

2.3.2 Measurement of diffusion coefficient with MR

In 1964, Stejskal and Tanner described a method for measuring D using pulsed gradients in a spin echo sequence (25). This method involves repeated MR experiments where successive experiments involve gradient pulses incremented such that b-value increases. The resulting signal is measured and plotted as a function of b-value, and the value of D is extracted from the fit to the data. In practice, identical gradient pulses are placed on opposite sides of the refocusing pulse, as shown in Figure 2.10. This allows the use of large

amplitude pulses, and correspondingly large signal attenuations, while resulting in no net phase accumulated by stationary spins. There is also no net effect on the frequency and phase encoding processes. This pulse sequence is known as a diffusion-weighted spin-echo (DW-SE) and the resulting images are known as diffusion-weighted images. Images acquired with greater b-value are said to have greater diffusion-weighting.

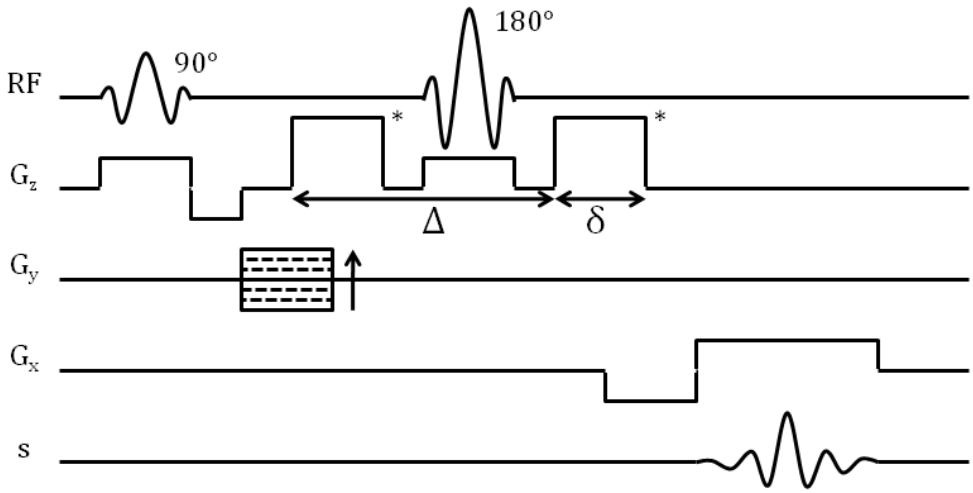

Figure 2.10. Spin-echo pulse sequence with diffusion lobes added (*). In this case, the diffusion lobes are applied along the z direction. The diffusion lobe separation Δ and duration δ are labeled.

For the common arrangement of paired rectangular diffusion-sensitizing pulses shown in Figure 2.10, the following expression for b is used:

$$b = \gamma^2 \cdot G^2 \cdot \delta^2 \cdot \left(\Delta - \frac{\delta}{3}\right), \tag{2.41}$$

where b is function of gradient amplitude G, diffusion lobe separation Δ, and diffusion lobe duration δ. In practice, the lobe may be trapezoidal or a similar shape, and pulse sequence design will compensate for the effects of imaging gradients (26).

Typically the gradient amplitude is incremented between diffusion measurement experiments while Δ, δ, and all other sequence parameters remain fixed. Gradient parameters are often chosen such that for the largest b-value used the gradient amplitude is at or near the maximum allowed by the MR system. This allows for the shortest TE possible for the sequence. Imaging with longer than necessary TE may create significant and undesirable T2-weighted contrast in the diffusion-weighted images, known as T2 shine-through (3,4). Additionally, if two subpopulations of spins are contributing to the signal in a given voxel (such as intracellular and extracellular water), and these two populations have significantly different T2 values, the population with shorter T2 will be increasingly attenuated with longer TE and will have a decreasing contribution to the measurement of D (22).

Proper selection of the b-values used in diffusion measurements is important. Signal attenuation as a function of b-value is generally monoexponential (equation 2.38), however, the behavior may be different at extremely high and extremely low b-values.

At low b-values, the effect of perfusion may influence the decay of signal. Perfusion is the incoherent flow, rather than diffusion, of water within voxels. This motion is incoherent as the organization of capillaries on the scale of voxels is approximately random (27). The signal decay as a function of b-value takes on the form:

$$S = S_0 \cdot [(1 - f) \cdot \exp(-b \cdot D) + f \cdot \exp(-b \cdot D^*)], \quad (2.42)$$

where f is known as the perfusion fraction, or the volume fraction of water flowing in perfused capillaries, and D* is known as the pseudodiffusion coefficient. The perfusion factor is typically on the order of 1% (27), and D* is typically an order of magnitude greater than D. It is possible to separate the contributions of perfusion and diffusion, and for this reason diffusion measurements will often start with a non-zero b-value, sufficiently large such that the second term in equation 2.42 is approximately zero.

Signal attenuation has also been found to deviate from monoexponential behavior at extremely large b-values. The majority of studies performing ADC measurements use b-values at or below 1000 s/mm^2. Studies that use b-values of up to 4000 s/mm^2 have found biexponential decay when the higher ranges of b-values are used (28,29). This is due to the presence of extremely slowly diffusing molecules. Over the time of a typical diffusion pulse, these molecules do not diffuse a great enough distance to significantly contribute to signal decay when normal b-values are used.

Measurement of these slowly diffusing molecules is difficult, as large b-values result in large signal attenuations and poor SNR images. Additionally, to achieve large b-values requires longer Δ, which in turn requires longer TE, leading to further signal loss by T2 relaxation.

ADC is typically measured by acquiring images at two different b-values (30-35), although in some studies up to 42 b-values have been used (36). Comparison between two b-value and six b-value method found no significant differences in measured ADC values (37).

2.4 T2

2.4.1 Theory

As introduced in section 2.1.7, the T2 relaxation time is the characteristic time of the exponential decay of the magnetization in the xy-plane (equation 2.27). It is also known as the transverse relaxation time, or the spin-spin relaxation time. T2 relaxation is a result of the magnetic dipole-dipole interaction between spins. Thermal motion of the spins randomly changes the distances between spins, which in turn changes the interaction energies, leading to energy exchange between spins. This energy exchange results in broadening of the resonant frequencies of the spins in the system. This broadening leads to dephasing of the spins, which results in destructive interference and decay of the signal.

The relaxation mechanism is tied to random motion of spins; therefore it is not surprising that relaxation rate has been found to be related to relative mobility of spins. Spins associated with larger macromolecules are associated with extremely rapid decay, while more mobile spins such as those in water are associated with slower decay. (3) T2 has been shown to be sensitive to multiple aspects of tissue physiology including free water abundance, macromolecular content, and necrotic fraction (38,39). These factors influence T2 by influencing the frequency of fluctuating magnetic fields caused by vibrating spins. Protons in water molecules bound to large proteins, for example, result in slower fluctuations and a large resonant frequency broadening effect and thus rapid T2 decay (3), while more mobile spins, like those found in free water or acellular necrotic tissue, are associated with much longer T2 times.

2.4.2 Measurement of T2 with MR

T2 can be measured using spin-echo images acquired with a range of echo times, and applying a fit to the images of the form of equation 2.27.

Images for T2 mapping are commonly acquired using one of two methods. The first is repeated application of the conventional spin-echo sequence seen in Figure 2.8, with increasing TE in successive applications (16, 40,41). Alternatively, a modified spin-echo sequence can be used, where multiple echoes over a range of TEs are acquired simultaneously (36,42). One such sequence that is often used is the Carr-Purcell-Meiboom-Gill (CPMG)

sequence, where a chain of 180° refocusing pulses follow the initial echo (43). A sample CPMG pulse sequence is shown in Figure 2.11. The CPMG sequence has the principal advantage of speed, as only one sequence application is required to obtain all echoes needed for T2 mapping. A disadvantage of the CPMG sequence is that it is sensitive to RF pulse non-uniformities and slice-profile imperfections, both of which may cause decay faster than predicted by $e^{-t/T2}$ (4), and the CPMG method is generally considered less accurate than the multiple acquisition method (44).

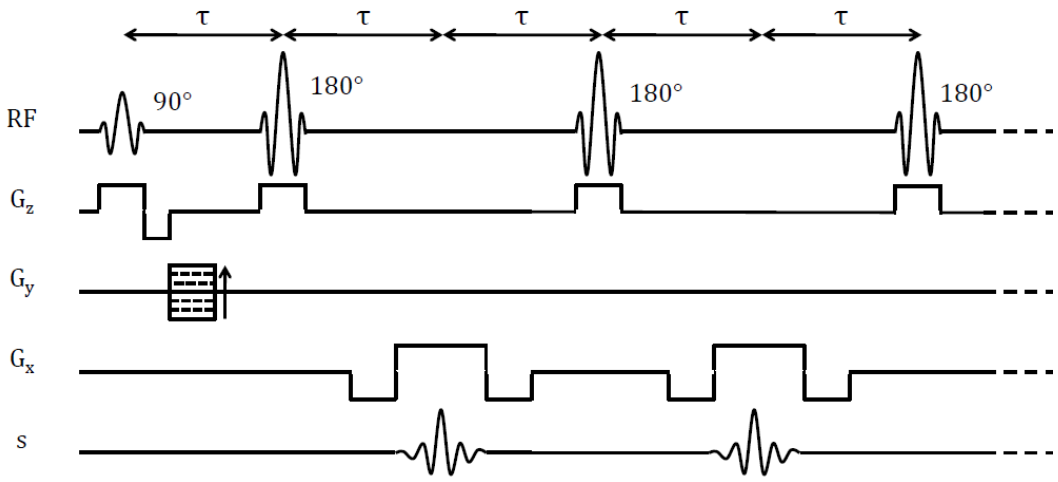

Figure 2.11. Pulse-sequence diagram for a CPMG sequence, employing a 90° excitation pulse, followed by a 180° refocusing pulse after time τ. A chain of refocusing pulses follows, with each pulse separated by 2τ. TE values are (2n + 1)τ.

After acquisition of images at multiple TEs using either method, a fit is made to the data to extract the T2 value of each voxel. In general, a monoexponential decay of the form of equation 2.27 is used (3,16,36,39-42).

Some groups have identified biexponential behavior in tumour tissues where physically segmented populations of spins with significantly different T2 values exist within the same voxels (45). Additionally, as noise in magnitude MR images has a non-zero mean, when very long TE values are used, signal does not go completely to zero. Some groups have added a constant term to the fit when measuring T2 in cases where tissue with very long T2 (such as cerebrospinal fluid) are present (44). In section 3.5.2 a comparison is made between a simple monoexponential fit and a monoexponential fit using a constant offset term, and it is found that the simple monoexponential is more appropriate for the measurements made in the work included in this thesis.

2.5 Radiation therapy

Multiple text books were used as general references in the writing of this section, and would serve as excellent resources for further reading. In particular, the topic of radiation therapy in general is extensively covered by *Principles and Practices of Radiation Oncology* (46) by Halperin, Perez, and Brady, while *Radiobiology for the Radiologist* (47) by Hall and Giaccia provides a thorough introduction to the field of radiobiology.

2.5.1 Introduction to radiation therapy

Radiation therapy (RT) is one of the major modalities used in the treatment of cancer. RT may be used for solid tumours when the location or geometry of the tumour indicates against surgery (46). RT may also be used in

order to shrink tumours before surgery (neoadjuvant RT), or to eliminate any residual cancer cells after surgery (adjuvant RT). RT is often used on patients who are also receiving chemotherapy.

The most common form of RT uses high energy photons to create ionization events within cells. Electrons from these events move through tissue and cause damage to cells as they deposit their energy, and may cause cell kill if DNA is sufficiently damaged. Damage caused by the electrons may be direct, resulting from high kinetic energy electrons breaking bonds in DNA, or indirect, resulting from high kinetic energy electrons interacting with water, producing free radicals which go on to damage DNA (47). RT relies on a variety of techniques to deliver the highest possible radiation dose to the tumour tissue, while minimizing dose to surrounding healthy tissues.

After DNA is damaged, there are a variety of pathways an individual cell can follow. Cells have a variety of mechanisms for detecting and responding to damage. Cells may repair sublethal or potentially lethal damage. Damage that cannot be properly repaired may lead to clonogenic death which, in cancer cells, is the ultimate goal of RT. Clonogenic death occurs when the cell in question can no longer divide and produce additional cells, though the cell itself may continue to survive for an extended period of time. This is distinct from absolute destruction of the cell. While clonogenic death can occur via apoptosis (where the cell detects damage and undergoes a programmed disassembly) or necrosis

(destruction due to extreme trauma to the cell), it can also result from sustained growth arrest (SGA), where radiation damage triggers signals in the cell that prevent the cell from moving through the cell cycle and reproducing, but while still remaining viable as an individual cell.

Clonogenic death via apoptosis and necrosis may have significant effects on tissue extracellular water content as cells are destroyed, and therefore may be important in influencing changes in ADC and T2 after treatment. Sustained growth arrest may have less immediate effect on tissue physiology, but will limit the ability of the tumour to grow.

2.5.2 Role of fractionation

The upper limits of radiation dose that can be delivered to tumour tissue are defined by the tolerances of surrounding normal tissue to radiation. It is well known that the tumourcidal effect of RT is lessened when the same dose is delivered in several fractions as opposed to a single fraction, due to the ability of tumour tissue to repair sublethal damage between fractions. In general, normal tissues exhibit repair kinetics that benefit more from a fractionated delivery than do tumours. By delivering a small dose per fraction (approximately 2 Gy) for a large number of fractions, it is possible to maximize the therapeutic ratio for this treatment modality.

Fractionation has many other complicated implications in radiobiology. A cell's location in the cell cycle is known to influence radiosensitivity, and allowing

time between fractions allows time for surviving cells to redistribute themselves into more sensitive phases of this cycle. Cells that were hypoxic at the time of irradiation may be reoxygenated between fractions, either by reversal of incidences of transient hypoxia, or preferential destruction of well-oxygenated cells, leading to improved oxygen and nutrient supply to the remaining cells. This increase in oxygenation may have a sensitizing effect on the tumour (see section 2.5.3). While redistribution and reoxygenation may increase the sensitivity of tumour cells to radiation, time between fractions allows tumour cell repair and repopulation. Dosage and fractionation scheme choice made by a radiation oncologist balances these factors.

Standard protocols for total dose and fractionation scheme vary by tumour type and location, but it is not unusual for treatments to involve 30 or more fractions of approximately 200 cGy delivered on a daily basis, with total doses of upwards of 7700 cGy (41). Other treatment strategies involve delivering the total dose in a reduced number of fractions (48) (hypofractionation), or increasing the number of fractions and reducing the time interval between fractions (49) (hyperfractionation). A technique known as radiosurgery (50) uses a high-dose single fraction of radiation for treatment.

2.5.3 Role of hypoxia

Cells that are hypoxic are considerably more resistant to conventional RT than well-oxygenated cells. This effect is described by a term known as the

oxygen enhancement ratio (OER) – the ratio of doses without and with oxygen required to produce the same biological effect. One of the main mechanisms by which oxygen sensitizes cells is the fixation of DNA damage produced by free radicals (47), preventing repair. Figure 2.12 is a plot of cell survival curves for cells irradiated in pure nitrogen versus irradiated in air. For cells irradiated in air, a given dose results in a significantly smaller fraction of cells surviving the treatment. Only small quantities of oxygen are required for radiosensitization. This is illustrated in Figure 2.13, in which the relative radiosensitivity of cancer cells is plotted as a function of oxygen tension.

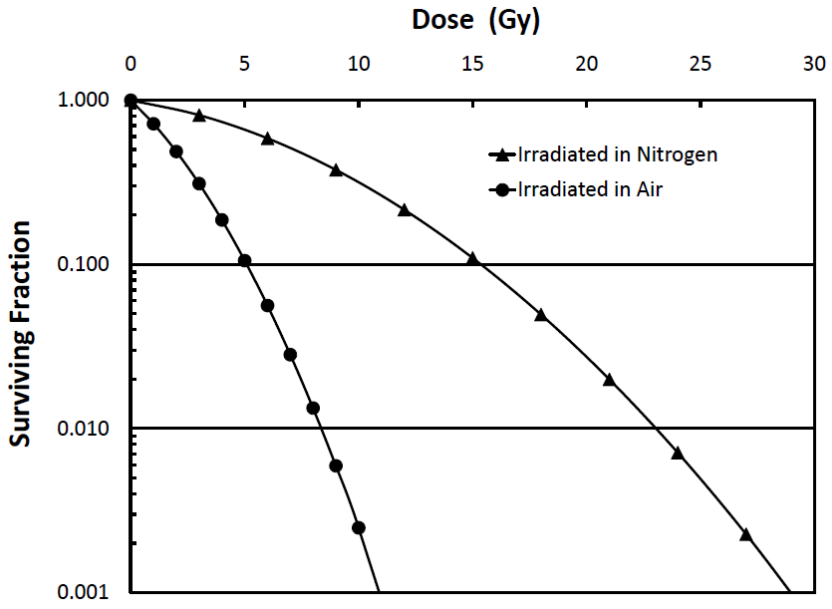

Figure 2.12. Surviving fraction of cells as a function of dose for populations irradiated either in the absence of oxygen (pure N_2) or in air. For any given dose, there is significantly higher level of cell kill and less surviving cells when treatment is given in air. This figure was generated using data from Barendsen et al (51).

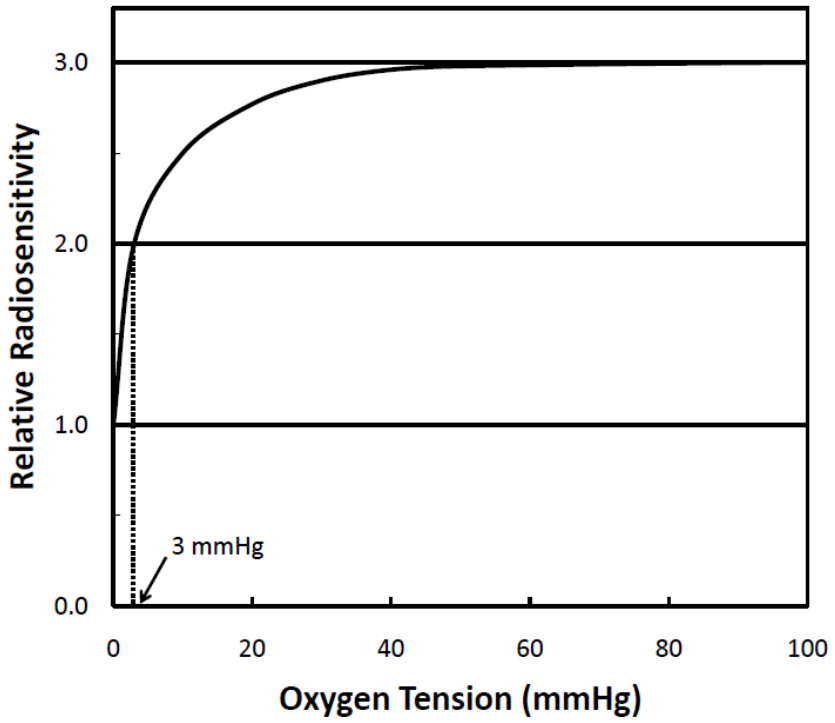

Figure 2.13. Relative radiosensitivity of a sample cancer cell line as a function of oxygen tension. Of note is the very small quantity of oxygen required for sensitization. The presence of 3 mm Hg of oxygen is sufficient to double the radiosensitivity of oxygen, relative to that under anoxic conditions. Note that atmospheric oxygen tension is approximately 155 mmHg.

There is evidence that presence of hypoxia may lead to survival of clonogenic cancer cells and be a significant cause of failure of RT (52-55).

2.6 Literature review

2.6.1 Call for expansion of techniques for monitoring post-treatment response

MR has a large role in monitoring treatment response in oncology. Use of MRI is primarily driven by the superior soft-tissue contrast offered by MRI in comparison to other imaging modalities, such as CT. Conventionally, assessing tumor response using MRI has consisted of monitoring tumor volume changes over time. The RECIST (Response Evaluation Criteria in Solid Tumors) guidelines (56) were a prominent attempt to standardize the assessment and classification of tumor response in the clinic, and noted the importance of accurate response evaluation when clinician and patient are making decisions regarding continuation or alteration of treatment course. This is primarily achieved by providing standards for imaging parameters for multiple modalities, guidelines for objective interpretations of images such as determining tumor volumes, and suggestions for timing frequency of imaging studies. However, the report also noted that "objective tumor response" as measured by volume change may be distinct from "clinical improvement". Jaffe has suggested that these methods are not sufficient to address the complexities of tumor response to treatment (57). Although citing the simplicity and "pragmatic adequacy" of these tools, he describes current assessment criteria as not taking advantage of advancements in technology, and Jaffe and others have noted that the timeframe over which

tumor volumes change may limit this method of assessment for informing clinical decision making at earlier stages of treatment.

In 2004, the National Cancer Institute of the United States convened a workshop calling for the expansion of the use of MR in the assessment of tumor response to therapy (58). Although the focus of the workshop was on dynamic contrast-enhanced (DCE)-MRI and MRS, the workshop report noted that there may be therapeutic effects which are of more interest to an oncologist than tumor shrinkage, and that MR-based techniques have the potential to predict patient response to therapy and enhance survival.

In 2006 Sorensen (59) addressed the use of MR as a cancer imaging biomarker and identified stages of biomarker development. This publication described the use of ADC in assessing treatment response as a pre-biomarker, meaning that "proof of concept establishing technical performance" has been demonstrated. Emphasis was made of its potential for development, and further research was called for in order to establish the utility and reproducibility of the technique for determining the early effects of therapy.

2.6.2 Use of ADC and T2 measurements in human patients

Publications which focus solely on changes in the T2 relaxation time in human patients are not common in the literature. There are, however, several publications addressing the use of T2 and/or ADC to assess response in a clinical setting. Among the most prominent have been a series of reports from the

Department of Radiology at the University of Michigan, investigating the response of brain tumours to treatment. A publication (60) from 2000 reported the results of an investigation involving two brain tumour patients, both of which received a combination of chemotherapy and radiation therapy. ADC maps were produced using a two b-value method (b-values of 100 and 1000 s/mm^2). One patient was classified as having stable disease after treatment, and a 10% increase in ADC was measured 12 weeks after the start of therapy. This was followed by a 30% ADC decrease below baseline during tumour regrowth 48 weeks after treatment. The second patient showed a peak ADC increase of 86% 6 weeks after treatment, and showed greater tumour shrinkage than did the first patient. Later publications from the same group (30,32) continued to focus on brain tumour response while still using a two b-value method for calculating ADC. These studies found that change in mean tumour ADC after treatment was predictive of overall survival, but used image registration to map ADC changes in individual pixels, and found that localized volumes within tumours showing increased ADC was had more predictive power than the average ADC change of the entire tumour. Explaining their repeated use of a two b-value method, this group cites findings from Burdette *et al* (37) which found no statistically significant differences in ADC values measured by faster two b-value methods compared to those measured using six b-values.

In another study involving brain tumours, Goldman *et al* (61) used Gamma Knife surgery (GKS) (ie. single-fraction radiation therapy) to treat 15 patients with a total of 25 brain metastases. Radiation dose ranged from 1200 to 2500 cGy, with a mean dose of 1800 cGy. ADC measurements were made using a three b-value method (b-values of 0, 500, and 1000 s/mm^2) with measurements pretreatment, and at mean time points of 54 and 100 days post-GKS. Relative ADC at the initial follow-up ranged from 0.90 to 3.13 times the initial value. All tumours with reduced ADC (relative ADC < 1.00) later became recurrent tumours. All tumours that showed increased ADC were later independently judged to have responded to treatment. The three tumours with the highest relative ADC (2.01, 2.96, 3.13) were classified as radionecrosis.

There are several studies that have examined ADC, and in some cases T2, response of tumours in a number of other sites. A study by Kim *et al* (41) of squamous cell carcinomas of the head and neck measured both ADC and T2 pretreatment, one week after the start of treatment, and two weeks after the end of treatment. Patients received a total dose of 7040 cGy delivered in 32 x 220 cGy fractions combined with chemotherapy. ADC calculation was done based on three b-value method (b-values of 0, 500, and 1000 s/mm^2). T2 calculation was done using four echo times of 13, 53, 80, and 110 ms. It was reported that ADC changes after the first week of chemoradiation were more sensitive than T2 measurements for sorting complete responders from partial

responders. Complete responders showed an average relative ADC increase of approximately 30%, while partial responders on average showed no ADC change. While neither group showed significant changes in T2 after the first week of therapy, the complete responders show a reduced T2 in measurements taken one week after the completion of treatment.

In the liver, Eccles *et al* (62) measured ADC using a two-point method (b-values of 0 and 600 s/mm^2) pretreatment, during weeks one and two of treatment, and one month post-treatment. Patients were treated with six fractions of radiation therapy delivered over two weeks, with the prescribed mean dose to tumour ranging from 2880 to 5400 cGy. Change in ADC after the first week of therapy was found to be associated with sustained tumour response. Additionally, a dose-dependent correlation was found between mean tumour dose and observed ADC change.

In cases of rectal carcinoma, Hein *et al* (63) used a three b-value method (b-values of 30, 300, 1100 s/mm^2) to measure ADC pretreatment and once weekly for four consecutive weeks during treatment for nine patients receiving combination chemotherapy and radiation therapy. Total radiation doses ranged from 3830 cGy to 4400 cGy with doses of 110 cGy delivered twice daily. In all nine patients, tumour ADC had decreased by the end of treatment, on average by approximately 30%. All patients had surgical resection of the tumour after chemoradiation, and the investigators found decreased ADC correlated with

increased interstitial fibrosis – accumulation of fibrotic connective tissue in the intercellular space. It is also significant to note that when defining tumour volumes, this study limited volume definition to regions believed to have viable tumour tissue, and necrotic volumes were purposefully excluded.

In cases of advanced cervical cancer, Harry *et al* (64) measured tumour ADC using a two b-value method (b-values of 0 and 1000 s/mm^2) pretreatment, after two weeks of treatment, and at the conclusion of treatment. All patients received a total dose of 4000 cGy delivered in 25 fractions accompanied by weekly chemotherapy. There was a single case of decreased ADC (relative ADC = 0.80). The mean relative ADC in all other cases ranged from approximately 1.1 to 1.8. Relative ADC measured after two weeks of treatment was found to correlate with clinical response, while no such correlation was found between changes in tumour volume measured after two weeks and eventual clinical response.

2.6.3 Use of ADC and T2 measurements in animal models of cancer

A limitation of many clinical studies is that the number of imaging sessions is small due to the required resources and demands on patient time. These factors make it difficult to study the time dependence of treatment response in humans with reasonable temporal resolution. The use of an animal model allows greater flexibility for serial MRI measurements, as well as allowing a more direct study of treatment response by controlling factors which might

influence tumor sensitivity such as tumor type, tumor cell line, tumor location, and tumor volume at the start of treatment. Summarized here are several notable studies of T2 and/or ADC response in animal models of cancer.

In 1996, Zhao *et al* (65) were one of the first to attempt to measure tumour response to treatment using diffusion measurements, inspired by reports of diffusion change associated with pathophysiological changes in the brain. Radiation-induced fibrosarcoma 1 (RIF-1) tumours were implanted subcutaneously in the backs of mice. When tumours had reached a volume of 200-600 mm^3, they were treated with one of two doses of chemotherapy (n = 6 per dose), with six mice left untreated to serve as a control. ADC measurements were performed using an eight b-value method, with b-values ranging from 100 to 2600 s/mm^2. Measurements were taken pretreatment, and 1, 2, 3, 4, 7, 8, and 9 days post-treatment. Peak relative ADCs of 1.9 and 1.5 were observed for the high and low dose groups, respectively. Peak ADC was observed four days post-treatment for both dose groups, with relative ADC dropping to 1.5 and 1.2 nine days after treatment.

A group from the University of Michigan followed with a series of papers examining the response of gliomas to a variety of chemotherapies. In one study (36), rat glioma cells were injected into the brains of 20 adult rats. A total of 13 rats were treated with a single dose of chemotherapy, with the other 7 serving as untreated controls. Four of the treated rats were sacrificed for histology.

Rats were imaged every 2 days until 22 days after treatment. ADC measurements were made using a 42 b-value method (b-values ranging from 87 to 1669 s/mm^2). T2 was measured using an 8 TE method (TE ranging from 20 to 160 ms). T1 was measured using an inversion recovery-based method. Maximum relative response was measured at 6 days post-treatment for ADC, T2, and T1 with relative values of 1.55, 1.27, and 1.16, respectively. ADC fell below baseline 16 days after treatment but T2 and T1 did not. Further reports from the same group showed similar increases in ADC for the same tumour model after gene therapy (33), and for the same treatment with the same cell line grown as subcutaneous tumours over the right hindquarter of rats (34). The use of an intracranial mouse model of glioma showed early increases in tumour ADC corresponded to tumour growth delay in response to chemotherapy (35). In this case, ADC calculations were made using a two b-value method (b-values of 100 and 1248 s/mm^2).

Jennings *et al* (66) measured ADC in tumours formed using human prostate cancer cells injected subcutaneously over the right flank of mice, which were treated using three doses of chemotherapy. ADC values were calculated using a three b-value method (b-values of 200, 400, and 800 s/mm^2). Mice were imaged pretreatment, as well as two and four days post-treatment. Tumours at all doses showed an approximately 35% increase in mean ADC two days after treatment. Tumours receiving the lowest two doses had mean relative ADC

values of approximately 1.45 by four days post-treatment, while the highest dose group had a mean relative ADC of greater than 1.55 at this time point.

Fei *et al* (67) measured T2 in human prostate tumour xenografts grown in mice. They measured tumour T2 immediately before and immediately after photodynamic therapy, followed by a final measurement 24 hour after treatment, with a total of 13 mice used. T2 values were calculated using four TE values (TEs of 28, 56, 84, and 111 ms). They found no significant difference in T2 values between the immediately pre- and post-treatment measurements, but found a statistically significant 22% increase in T2 24 hours after treatment.

Huang *et al* (40) modeled non-Hodgkin's lymphoma (NHL) in mice by injecting human NHL cells subcutaneously over the right thigh of mice. Five tumour-bearing mice were treated weekly with chemotherapy for four consecutive weeks and five mice were reserved as controls. Measurements of tumour ADC and T2 were made pretreatment and after completion of each cycle of chemotherapy. ADC values were calculated using a four b-value method (b-values of 0, 149, 596, 1342 s/mm^2) and T2 values were calculated using four TEs ranging from 15 to 75 ms. A maximum mean relative ADC of approximately 1.17 was measured after the third treatment. A decrease in mean relative T2 was observed after the first treatment, with a minimum relative T2 of approximately 0.90 being measured after the third treatment.

Finally, Henning *et al* published a two-part study (16,68) where RIF-1 tumours, grown subcutaneously over the right hind leg, were treated with 1000 cGy of 6 MeV electrons. Animals were imaged 1 day before treatment, 5 hours after treatment, 1 and 2 days after treatment, and then 2 days thereafter until the tumours had doubled in volume, to a maximum of 14 days after treatment. ADC values were calculated using a six b-value method (b-values of 15, 60, 140, 390, 560, and 760 s/mm^2) and T2 values were calculated using six TEs (TEs of 12.2, 20.0, 35.0, 50.0, 65.0, and 90.0 ms). This study also mapped proton density, and attempted to segment tissues based on clustering in the 3D space with dimensions of ADC, T2, and proton density. While concluding that proton density did not add sensitivity to the clustering method, it was found that differences in ADC could separate viable from necrotic tissue, and differences in T2 could further segment these populations. In response to radiotherapy, increases in ADC were seen in regions preclassified as both viable and necrotic. No significant change in T2 was observed in any subpopulations, although mean tumour T2 showed a slight increase (~ 6%) five hours post-treatment, followed by a decrease one and two days post-treatment (~8%), before returning to baseline at later time points.

The goal of the work described in this dissertation is to address limitations in the existing literature. Limitations of many clinical studies include limited numbers of imaging sessions due to required resources and demands on

patient time, limited numbers of patients accrued to studies, and inherent variations in tumours between individuals. Additionally, clinical studies are not able to use untreated controls for obvious ethical reasons, and similarly cannot easily investigate the dose-dependence of response. The use of mice in our work allows a more direct study of treatment response by controlling factors which might influence tumor sensitivity such as tumor type, tumor cell line, tumor location, and tumor volume at the start of treatment. Additionally, factors such as dose, fractionation, and tumour oxygenation can be varied in ways not possible in clinical studies. Investigation of the response of ADC and T2 to radiation is currently not well covered in the literature, and the following work attempts to improve the understanding of these responses to radiation under a variety of treatment schemes and conditions.

References

1. Lauterbur P. Image formation by induced local interactions: examples employing nuclear magnetic resonance. *Nature.* 1973: p. 190-191.

2. Damadian R. Tumor detection by nuclear magnetic resonance. *Science.* 1971: p. 1151-1153.

3. Nishimura DG. Principles of Magnetic Resonance Imaging. Palo Alto, CA: *Stanford University Press*; 1996.

4. Bernstein MA, King KF, Zhou XJ. Handbook of MRI pulse sequences. Burlington, MA, USA: *Elsevier Academic Press*; 2004.

5. Elmore JG, Armstrong K, Lehman CD, Fletcher SW. Screening for breast cancer. *J. Am. Med. Assoc.* 2005: p. 1245-1256.

6. Kriege M, Brekelmans CTM, Boetes C, Besnard PE, Zonderland HM, Obdeijn IM, et al. Efficacy of MRI and mammography for breast-cancer screening in women with a familial of genetic predisposition. *N. Engl. J. Med.* 2004: p. 427-437.

7. DeAngelis LM. Brain Tumors. *N. Engl. J. Med.* 2001: p. 114-123.

8. Orel SG, Schnall MD. MR imaging of the breast for the detection, diagnosis, and staging of breast cancer. *Radiology.* 2001: p. 13-30.

9. Harms SE. MRI in breast cancer diagnosis and treatment. *Curr. Probl. Diagn. Radiol.* 1996: p. 192-215.

10. Weitz J, Koch M, Debus J, Hohler T, Galle PR, Buchler MW. Colorectal cancer. *Lancet.* 2005: p. 153-65.

11. Jani AB, Hellman S. Early prostate cancer: clinical decision-making. *Lancet.* 2003: p. 1045-1053.

12. Coakley F, Qayyum A, Kurhanewicz J. Magnetic resonance imaging and spectroscopic imaging of prostate cancer. *J. Urol.* 2003: p. S69-S76.

13. Stanescu T, Jans HS, Pervez N, Stavrev P, Fallone BG. A study on the magnetic resonance imaging (MRI)-based radiation treatment planning of intracranial lesions. *Phys. Med. Biol.* 2008: p. 3579-3593.

14. Ross BD, Moffat BA, Lawrence TS, Mukherji SK, Gebarski SS, Quint DJ, et al. Evaluation of cancer therapy using diffusion magnetic resonance imaging. *Mol. Cancer Ther.* 2003: p. 581-586.

15. Hamstra DA, Rehemtulla A, Ross BD. Diffusion magnetic resonance imaging: a biomarker for treatment response in oncology. *J. Clin. Oncol.* 2007: p. 4104-4109.

16. Henning EC, Azuma C, Sotak CH, Helmer KG. Multispectral quantification of tissue types in a RIF-1 tumor model with histological validation. Part I. *Mag. Reson. Med.* 2007: p. 501-512.

17. Yezhelyev MV, Gao X, Xing Y, Al-Hajj A, Nie S, O'Regan RM. Emerging use of nanoparticles in diagnosis and treatment of breast cancer. *Lancet Oncol.* 2006: p. 657-667.

18. Zhao M, Beauregard DA, Loizou L, Davletov B, Brindle KM. Non-invasive

detection of apoptosis using magnetic resonance imaging and a targeted contrast agent. *Nature Med.* 2001: p. 1241-1244.

19. Gillies R, Morse D. In vivo magnetic resonance spectroscopy in cancer. *Annu. Rev. Biomed. Eng.* 2005: p. 287-326.

20. Hahn EL. Spin echoes. *Phys. Rev.* 1950: p. 580-594.

21. Carr HY, Purcell EM. Effects of diffusion on free precession in nuclear magnetic resonance experiments. Phys. Rev. 1954: p. 630-638.

22. Szafer A, Zhong J, Anderson AW, Gore JC. Diffusion-weighted imaging in tissues: theoretical models. *NMR in Biomed.* 1995: p. 289-296.

23. Basser PJ. Inferring microstructural features and physiological state of tissues from diffusion-weighted images. *NMR in Biomed.* 1995: p. 333-344.

24. Le Bihan D. Molecular diffusion, tissue microdynamics and microstructure. *NMR in Biomed.* 1995: p. 375-386.

25. Stejskal EO, Tanner JE. Spin diffusion measurements: spin echoes in the presence of a time-dependent field gradient. *J. Chem. Phys.* 1965: p. 288-292.

26. Mattiello J, Basser PJ, LeBihan D. Analytical expressions for the b matrix in

NMR diffusion imaging and spectroscopy. *J. Mag. Reson*. 1994: p. 131-141.

27. Le Bihan D, Breton E, Lallemand D, Aubin ML, Vignaud J, Laval-Jeantet M. Seperation of diffusion and perfusion in intravoxel incoherent motion MR imaging. *Radiology.* 1988: p. 497-505.

28. Mardor Y, Pfeffer R, Spiegelmann R, Roth T, Maier SE, Nissim O, et al. Early detection of response to radiation therapy in patients with brain malignancies using conventional and high b-value diffusion-weighted magnetic resonance imaging. *J. Clin. Oncol.* 2003: p. 1094-1100.

29. Roth Y, Tichler T, Kostenich G, Ruiz-Cabello J, Maier SE, Cohen JS, et al. High-b-value diffusion-weighted MR imaging for pretreatment prediction and early monitoring of tumor response to therapy in mice. *Radiology.* 2004: p. 685-692.

30. Hamstra DA, Galban CJ, Meyer CR, Johnson TD, Sundgren PC, Tsien C, et al. Functional diffusion map as an early imaging biomarker for high-grade glioma: correlation with conventional radiologic response and overall survival. *J. Clin. Oncol.* 2008: p. 3387-3394.

31. Lee KC, Moffat BA, Schott AF, Layman R, Ellingworth S, Juliar R, et al. Prospective early response imaging biomarker for neoadjuvant breast cancer chemotherapy. *Clin. Cancer Res.* 2007: p. 443-450.

32. Moffat BA, Chenevert TL, Lawrence TS, Meyer CR, Johnson TD, Dong Q, et al. Functional diffusion map: a noninvasive MRI biomarker for early stratification of clinical brain tumor response. *Proc. Natl. Acad. Sci. USA.* 2005: p. 5524-5529.

33. Stegman LD, Rehemtulla A, Hamstra DA, Rice DJ, Jonas SJ, Stout KL, et al. Diffusion MRI detects early events in the response of a glioma model to the yeast cytosine deaminase gene therapy strategy. *Gene Therapy.* 2000: p. 1005-1010.

34. Schepkin VD, Chenevert TL, Kuszpit K, Lee KC, Meyer CR, Johnson TD, et al. Sodium and proton diffusion MRI as biomarkers for early therapeutic response in subcutaneous tumors. *Mag. Res. Imaging.* 2006: p. 273-278.

35. McConville P, Hambardzumyan D, Moody JB, Leopold WR, Kreger AR, Woolliscroft MJ, et al. Magnetic resonance imaging determination of tumor grade and early response to temozolomide in a genetically engineered mouse model of glioma. *Clin. Cancer Res.* 2007: p. 2897-2904.

36. Chenevert TL, McKeever PE, Ross BD. Monitoring early response of experimental brain tumors to therapy using diffusion magnetic resonance imaging. *Clin. Cancer Res.* 1997: p. 1457-1466.

37. Burdette JH, Elster AD, Ricci PE. Calculation of Apparent Diffusion

Coefficients (ADCs) in Brain Using Two-Point and Six-Point Methods. J. *Comput. Assist. Tomogr.* 1998: p. 792-794.

38. Mitchell DG, Burk DLJ, Vinitski S, Rifkin MD. The biophysical basis of tissue contrast in extracranial MR imaging. *Am. J. Roentgenol.* 1987: p. 831-837.

39. Rofstad EK, Steinsland E, Kallhus O, Chang YB, Hovik B, Lyng H. Magnetic resonance imaging of human melanoma xenografts in vivo: proton spin-lattice and spin-spin relaxation times versus fractional tumour water content and fraction of necrotic tumour tissue. *Int. J. Radiat. Biol.* 1994: p. 387-402.

40. Huang MQ, Pickup S, Nelson DS, Qiao H, Xu HN, Li LZ, et al. Monitoring response to chemotherapy of non-Hodgkin's lymphoma xenografts by T2-weighted and diffusion-weighted MRI. *NMR in Biomed.* 2008: p. 1021-1029.

41. Kim S, Loevner L, Quon H, Sherman E, Weinstein G, Kilger A, et al. Diffusion-weighted magnetic resonance imaging for predicting and detecting early response to chemoradiation therapy of squamous cell carcinomas of the head and neck. *Clin. Cancer Res.* 2009: p. 986-994.

42. Sun Y, Mulkern RV, Schmidt K, Doshi S, Albert MS, Schmidt NO, et al. Quantification of water diffusion and relaxation times of human U87 tumors in a mouse model. *NMR in Biomed.* 2004: p. 399-404.

43. Meiboom S, Gill D. Modified spin-echo method for measuring nuclear relaxation times. *Rev. Sci. Instrum.* 1958: p. 688-691.

44. Pell GS, Briellmann RS, Waites AB, Abbott DF, Lewis DP, Jackson GD. Optimized clinical T2 relaxomtery with a standard CPMG sequence. *J. Mag. Reson. Imaging.* 2006: p. 248-252.

45. Schad LR, Brix G, Zuna I, Harle W, Lorenz WJ, Semmler W. Multiexponential proton spin-spin relaxation in MR imaging of human brain tumors. *J. Comput. Assist. Tomogr.* 1989: p. 577-587.

46. Halperin EC, Pereze CA, Brady LW. Principles and Practice of Radiation Oncology. 5th ed. Philadelphia: *Lippincott, Williams & Williams;* 2008.

47. Hall EJ, Giaccia AJ. Radiobiology for the Radiologist. 6th ed. Philadelphia, PA: *Lippincott, Williams & Williams;* 2006.

48. Muriel VP. Hypofractionation in radiotherapy. *Clin. Transl. Oncol.* 2007: p. 21-27.

49. Jeremic B, Shibamoto Y, Milicic B, Nikolic N, Dagovic A, Aleksandrovic J, et al. Hyperfractionated radiation therapy with or without concurrent low-dose daily Cisplatin in locally advanced squamous cell carcinoma of the head and neck: a prospective randomized trial. *J. Clin. Oncol.* 2000: p. 1458-1464.

50. Andrews DW, Bednarz G, Evans JJ, Downes B. A review of 3 current radiosurgery systems. *Surg. Neurol.* 2006: p. 559-564.

51. Barendsen GW, Koot CJ, van Kersen GR. The effect of oxygen on impairment of the proliferative capacity of human cells in culture by ionizing radiations of different LET. *Int. J. Rad. Biol.* 1966: p. 317-327.

52. Moulder JE, Rockwell S. Tumor hypoxia: its impact on cancer therapy. *Cancer Metastasis Rev. 1987*: p. 313-341.

53. Koutcher JA, Alfieri AA, Devitt ML, Rhee JG, Kornblith AB, Mahmood U. Quantitative changes in tumor metabolism, partial pressure of oxygen, and radiobiological oxygenation status postradiation. *Cancer Res.* 1992: p. 4620-4627.

54. Moeller BJ, Richardson RA, Dewhirst MW. Hypoxia and radiotherapy: opportunities for improved outcomes in cancer treatment. *Cancer Metastasis Rev.* 2007: p. 241-248.

55. Vaupel P, Mayer A. Hypoxia in cancer: significance and impact on clinical outcome. *Cancer Metastasis Rev.* 2007: p. 225-239.

56. Therasse P, Arbuck SG, Eisenhauer EA, Wanders J, Kaplan RS, Rubinstein L, et al. New guidelines to evaluate the response to treatment in solid tumors. *J.*

Natl. Cancer Inst. 2000: p. 205-216.

57. Jaffe CC. Measures of response: RECIST, WHO, and New Alternatives. *J. Clin. Oncol.* 2006: p. 3245-3251.

58. Evelhoch J, Garwood M, Vigneron D, Knopp M, Sullivan D, Menkens A, et al. Expanding the use of magnetic resonance in the assessment of tumor response to therapy: workshop report. *Cancer Res.* 2005: p. 7041-7044.

59. Sorensen AG. Magnetic resonance as a cancer imaging biomarker. *J. Clin. Oncol.* 2006: p. 3274-3281.

60. Chenevert TL, Stegman LD, Taylor JMG, Robertson PL, Greenberg HS, Rehemtulla A, et al. Diffusion magnetic resonance imaging: an early surrogate marker of theapeutic efficacy in brain tumors. *J. Natl. Cancer Inst*. 2000: p. 2029-2036.

61. Goldman M, Boxerman JL, Rogg JM, Norén G. Utility of apparent diffusion coefficient in predicting the outcome of Gamma Knife-treated Brain metastases prior to changes in tumor volume: a preliminary study. *J. Neurosurg*. 2006: p. 175-182.

62. Eccles C, Haider EA, Haider MA, Fung S, Lockwood G, Dawson LA. Change in diffusion weighted MRI during liver cancer radiotherapy: preliminary

observations. *Acta Oncol.* 2009: p. 1034-1043.

63. Hein PA, Kremser C, Judmaier W, Griebel J, Pfeiffer KP, Kreczy A, et al. Diffusion-weighted magnetic resonance imaging for monitoring diffusion changes in rectal carcinoma during combined, preoperative chemoradiation: preliminary results of a prospective study. *Eur. J. Radiol.* 2003: p. 214-222.

64. Harry VN, Semple SI, Gilbert FJ, Parkin DE. Diffusion-weighted magnetic resonance imaging in the early detection of response to chemoradiation in cervical cancer. *Gynecol. Oncol.* 2008: p. 213-220.

65. Zhao M, Pipe JG, Bonnett J, Evelhoch JL. Early detection of treatment response by diffusion-weighted 1H-NMR spectroscopy in a murine tumour in vivo. *Br. J. Cancer.* 1996: p. 61-65.

66. Jennings D, Hatton BN, Guo J, Galons JP, Trouard TP, Raghunand N, et al. Early response of prostate carcinoma xenografts to docetaxel chemotherapy monitored with diffusion MRI. *Neoplasia.* 2002: p. 255-262.

67. Fei B, Wang H, Meyers JD, Feyes DK, Oleinick NL, Duerk JL. High-field magnetic resonance imaging of the response of human prostate cancer to Pc 4-based photodynamic therapy in an animal model. *Lasers Surg. Med.* 2007: p. 723-730.

68. Henning EC, Azuma C, Sotak CH, Helmer KG. Multispectral tissue characterization in a RIF-1 tumor model: monitoring the ADC and T2 responses to single-dose radiotherapy. Part II. *Mag. Reson. Med.* 2007: p. 513-519.

Chapter 3: Methods and Materials

The experiments outlined in this dissertation involved a number of distinct stages. This chapter discusses key procedures and equipment used in each of these stages, beginning with the animal model of cancer used in these experiments (section 3.1). The bulk of the chapter discusses the MRI system used (section 3.2) and the procedure for acquiring and processing the MR images (sections 3.3-3.5). The method of delivering radiation to the tumour model is summarized in section 3.6, a method for inducing hypoxia in tumours is described in section 3.7, and finally the process of *ex vivo* analysis of tumours by histological methods is described in section 3.8.

3.1 Animal Model

An animal model of cancer is used to study the response of cancerous tissue to therapeutic radiation. A model is used in which mice carry a tumour

grown from human glioblastoma multiforme (GBM) cells. When tissues from one species of animal are implanted into an animal of a different species, such as in this case, the grafted tissue is known as a xenograft.

All animal procedures were approved in advance by the Cross Cancer Institute's Animal Care Committee, and all procedures involved ongoing consultation and supervision by laboratory animal technicians.

3.1.1 Host animal

For a xenograft to be successful, management of the immune response of the host animal is crucial. In cancer research using xenografts, it is common to use rodents that have little or no natural immune response. Our model uses a specific strain of mouse known as the NIH-iii nude (Charles River Laboratories, MA, USA). A key feature of the NIH-iii nude is the presence of the nude gene (1), which results in the absence of the thymus and therefore absence of T-cell immune response. Additionally, the mouse has two other mutations that reduce the overall function of the immune system. The extremely weakened immune system of this strain of mouse makes it an ideal host for human tumour xenografts, as the animal's immune system is unable to attack injected cancer cells with sufficient force to limit tumour formation and growth.

3.1.2 Cancer cell line

An additional factor that affects the success of a cancer xenograft is the choice of cell line to be injected into the host animal. Different cell lines from the

same type of cancer can express widely varying abilities to grow within host animals. Additionally, individual cell lines have been shown to lose malignancy with increasing time spent *in vitro*. This in turn reduces the cell line's tumourgenecity (ability to produce tumours *in vivo*) (2).

A specific human GBM cell line, M006xLo (3), was chosen for these studies, because it had been previously been studied both *in vitro* and using *in vivo* animal models by the Turner Lab at the Cross Cancer Institute. Cells are chosen from frozen samples which have had different numbers of cycles of growth on culture plates, followed by replating. Each cycle is known as a passage. Initial observations of M006xLo tumour growth in the NIH-iii nude mice were used to choose the optimal passage of cells to use in order to produce both a high tumour production rate and an appropriate growth rate. First attempts yielded extremely low tumour production rates. Subsequent attempts with earlier passages of cells yielded high tumour production rates, but tumours that took too long to reach a usable size. Finally, even earlier passages of the cell line were used, and the high tumour production rates were maintained, while producing tumours that grew sufficiently fast to produce usable tumours quickly, without being unmanageable. Specific tumour production rates and tumour growth rates are discussed in section 3.1.3.

Female nude mice at 6 weeks of age were ordered from Charles River Laboratories approximately three weeks before cell injections were planned.

With a typical delivery time of one week, this allowed the mice approximately two weeks to acclimatize to their new surroundings in the Cross Cancer Institute's vivarium. Upon arrival, mice were moved to temperature and humidity controlled cages in a conventional animal holding facility as described by the Canadian Council on Animal Care guidelines (4). The animals were not stored in more strictly controlled areas (ie. a microbiological barrier facility), because they would be transported outside of the vivarium for MR imaging and doing so would risk bringing contaminants from the MR area into the barrier facility. Mice were given 350 cGy of total body irradiation in a ^{137}Cs irradiator one week prior to cancer cell injection, in order to minimize any residual immune response present in the animals.

Cells used for injections have been incubated in conditions that facilitate exponential growth. This helps enhance the likelihood that the cells will proliferate once they are injected into the host animal. The cells were collected and repeatedly washed with phostphate-buffered saline (PBS) and centrifuged, removing all trace of growth serum from the cells. Finally, the cells were resuspended in a smaller volume of PBS to produce a concentration of 3 million cells per 0.1 mL of PBS. The resulting suspension was the final product which was injected into the mice.

The cell suspension was taken to the vivarium where the cell injections take place. A 25-gauge hypodermic needle affixed to a 1.0 mL syringe was used

for each injection. Use of larger gauge (smaller bore) needles is desirable for subcutaneous injections to prevent leakage of the injected material from the injection site. In the case of cell injections, if the inner diameter of the needle is too small, cells may lyse during ejection from the syringe, resulting in failure for a tumour to form. A 25-gauge needle is a compromise between the two demands.

Each mouse was anesthetized using 2% isoflurane dissolved in oxygen gas, delivered via nosecone. With the mouse anesthetized, the skin over the outside of the right thigh was pinched to form a "tent", into which 0.1 mL of the cell suspension was injected subcutaneously. This injection site was chosen for numerous reasons. The leg can be immobilized and is distant from the heart and lungs, which minimizes the appearance of artifacts related to cardiac and respiratory motion in MR images of the tumour. The superficial location on a limb permits easy observation and measurement of tumour growth, and makes direct irradiation possible with minimal radiation dose to critical structures in the abdomen. Finally, the skin over the thigh is sufficiently loose as to allow the tumour to grow to a size that is sufficient for our purposes. At an injection site further down the limb, for example, growth of the tumour would strain already tightly-stretched skin and cause the mouse pain, requiring much earlier termination of the experiment and euthanasia of the mouse.

During anesthesia, each mouse had a small hole punched in its ear to facilitate identification of specific animals within the same cage. The punch was

made at a unique location for each animal, corresponding to an in-house identification key. After the ear was punched, the mouse was allowed to recover from anesthesia.

Approximately three days after cell injection, small tumours appeared at the injection site. At first, these tumours were only detectable by palpation, giving the impression of a grain of sand underneath the skin. By one week after injection, most tumours had grown to a size where they are visible to the naked eye and their dimensions physically measured. At this point, tumours were measured using a digital caliper. Tumour volumes were estimated by assuming the tumour shape to be ellipsoid and using the equation

$$volume = \frac{4}{3} \cdot \pi \cdot \frac{x}{2} \cdot \frac{y}{2} \cdot \frac{z}{2}, \tag{3.1}$$

where *x*, *y*, and *z*, are the tumour dimensions in the left-right, anterior-posterior, and superior-inferior directions, respectively.

Tumour dimensions were measured on a daily basis until they had reached a predetermined volume of 150 mm^3, after which they were slated for MR imaging and radiation treatment. This volume was chosen after experimentally determining that this volume could be easily visualized by conventional scans using the 9.4 T system. This volume was also early enough in the tumour growth to allow sufficiently long observation time after the start of treatment or observation (at least 2-3 weeks). We are obligated to euthanize

mice once the tumour has grown to sufficient size to burden or distress the animal. If treatment and observation had started at larger volumes, the tumour may have become a significant burden before full post-treatment observations were complete, particularly for control animals, or animals receiving low dose treatments.

Once the animal model had been finalized, 100% of injections resulted in formation of a tumour. Not all tumours, however, were determined to be suitable for experimental purposes. Extreme outliers in growth rate were excluded from the experimental sample. Tumours that took longer than 4 weeks to reach 150 mm^3 were excluded, as were tumours that reached 150 mm^3 in less than ten days. While most tumours developed in a roughly spherical shape over the right thigh, some tumours developed in a "string of pearls" formation, where several distinct tumours formed in a line, starting at the thigh and moving up the side of the mouse's abdomen. These tumours were also rejected from the sample as they were difficult to image due to respiratory motion artifacts in images, difficult to treat because of their extended shapes, and because they differed significantly from the average geometry of the tumours, which may affect the characteristics of their response to treatment. Overall, 77.3% of cell injections resulted in usable tumours for experimental purposes. Table 3.1 contains a summary of growth behaviors for the tumours used in this study. Average tumour growth after cell injection was roughly linear. A plot of tumour

growth for untreated tumours is shown in Figure 3.1. A least-squares fit of a straight line to the untreated growth curve yields a linear growth rate of (14.6 ± 0.4) mm^3 / day.

Table 3.1. Summary of tumour growth behavior and frequency of reasons for tumour rejection from experimental sample.

Description	#	% Total
Good growth rate / shape/location	75	77.3%
Growth too slow	8	8.2%
Growth too fast	7	7.2%
Bad location / shape	7	7.2%

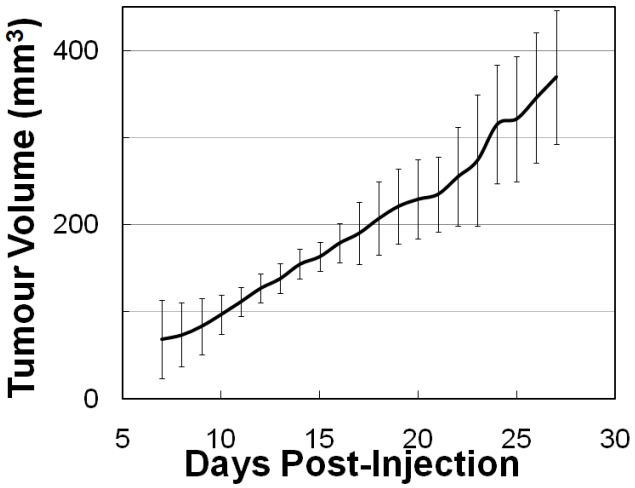

Figure 3.1. Average tumour growth for six untreated tumour xenografts as a function of time after M006xLo cell injection. Error bars represent standard deviation in volume.

3.2 The 9.4 T MR System

The 9.4 T MR system at the Cross Cancer Institute is comprised of a commercially available (Magnex Scientific, Oxford, UK) superconducting magnet and gradient system interfaced to a TMX (theory-model-experiment) console, built by the National Research Council of Canada Institute for Biodiagnostics – West (NRC-IBD-West, Winnipeg, MB).

The magnet structure that provides the B_0 field has a roughly cylindrical shape, with an inner diameter of 210 mm, with a length of 1.47 m. In addition to the primary coils, there are superconducting shim coils that are used to make slight adjustments to the B_0 field in order to improve magnetic field uniformity. These coils are energized at the time of magnet commissioning via a long probe which connects to an interface submerged within the helium bath and cannot be readily altered once the magnet is put into service. At the time of commissioning, a B_0 field homogeneity of 4.56 ppm (peak-to-peak) was measured over a 10 cm sphere of air at the centre of the magnet.

Further refinement of B_0 homogeneity can be made by adjustment of room temperature (ie. non-superconducting) shim coils. These shim coils, unlike the superconducting shims, can be adjusted at any time, as they are each connected to an external power supply, which can be controlled from the operator station. In practice, just prior to an MRI experiment, the MR operator adjusts the room temperature shims, determining the optimal settings either

experimentally (see section 3.4) or with the aid of a field-mapping sequence, such as FASTERMAP (5).

A smaller cylinder containing the gradient coils is located coaxially within the larger magnet housing. The outer diameter of the gradient housing is slightly smaller than the inner diameter of the magnet housing. The gradients are carefully positioned so that the centers of both the superconducting magnet and gradient coils are identical. The gradient coils used in the Cross Cancer Institute's 9.4 T MRI system have a peak gradient strength of 400 mT/m. The coils are connected to an external set of current amplifiers which are in turn controlled by the TMX console. Gradient cooling is achieved by a circulating water system.

The magnet is passively shielded within a large steel vault. There is a large door at the front of the vault, with copper "edging" to seal the edges of the door when closed (see Figure 3.2). There is a large filter-plate at the rear of the vault for passing power for shim, gradient, and RF coils, as well as lighting, into the vault. There are fittings for passing water cooling supply and return lines into and out of the vault. There are wave guides at both front and back for animal monitoring and anesthesia equipment.

Figure 3.2. Exterior photographs of magnet vault. Front view (left) shows view through vault door including cryostat (i), magnet bore (ii), front wave-guide (iii), and vault door (iv). Rear view shows rear RF filter panel (v) and rear wave guide (vi).

During regular MR imaging, various RF coils can be used for RF excitation and reception. For all work contained within this dissertation, a birdcage-style quadrature volume coil was used for both RF excitation and reception during imaging. This coil had an inner diameter of 44 mm and was produced by NRC-IBD West.

Outside of the magnetic field and RF shielding cage there is an electronics rack which holds a 4 kW RF amplifier, six gradient amplifiers (two each for x, y, and z gradients), and the power supply and controlling computer for the room temperature shim coils. This electronics rack is shown in Figure 3.3.

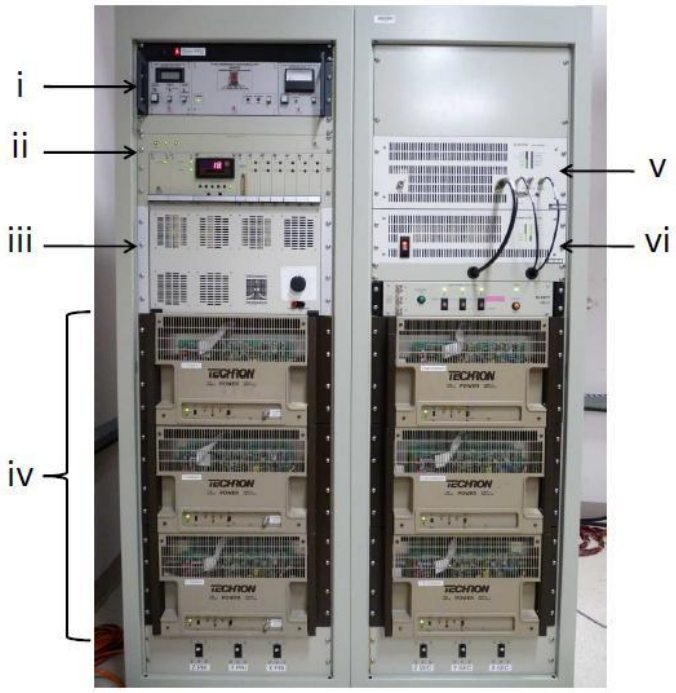

Figure 3.3. Photograph of amplifier electronics rack showing cryogen monitoring system (i), gradient monitoring system (ii), room temperature shim coil power supply (iii), six gradient amplifiers (iv), RF amplifier power supply (v), and RF amplifier (vi).

A second electronics rack is located in an adjacent temperature- and humidity-controlled closet. This rack holds key components for both the generation of RF and gradient pulse shapes that make up MRI pulse sequences, and reception of RF signal received during the signal acquisition phase of MRI sequences. Transmission components include computers which generate the desired pulse shapes and control sequence timings, a frequency synthesizer which generates an oscillating signal at the desired NMR frequency and variable gain amplifiers which are used to scale the amplitude of RF pulses before they are sent to the high-power amplifier rack.

Finally, the MR operator controls the entire MRI system from a PC station just outside the magnetic and RF shielding vault. The graphical user interface (GUI) program was written by NRC-IBD West employees based out of Calgary, AB. The GUI gives the user control over all pulse sequence parameters as well as manual control of all shim settings and RF amplification settings on both the reception and transmission sides, all of which is frequently automated in commercial systems. The process of calibrating / optimizing these settings is described in detail in section 3.4.1. The high degree of access gives a high degree of customizability, but can also make initial operation difficult.

3.3 Mouse setup and monitoring for MRI

A MR-compatible small animal monitoring system (Model 1025, SA Instruments, Inc., Stony Brook, NY, USA) is used to monitor the body temperature and respiration rate of each mouse at all times during MR imaging. Electrocardiograph monitoring can be done, but was deemed not necessary for these experiments and is not used. The system outputs to a PC positioned next to the MR operator station. A simplified schematic of the system is shown in Figure 3.4.

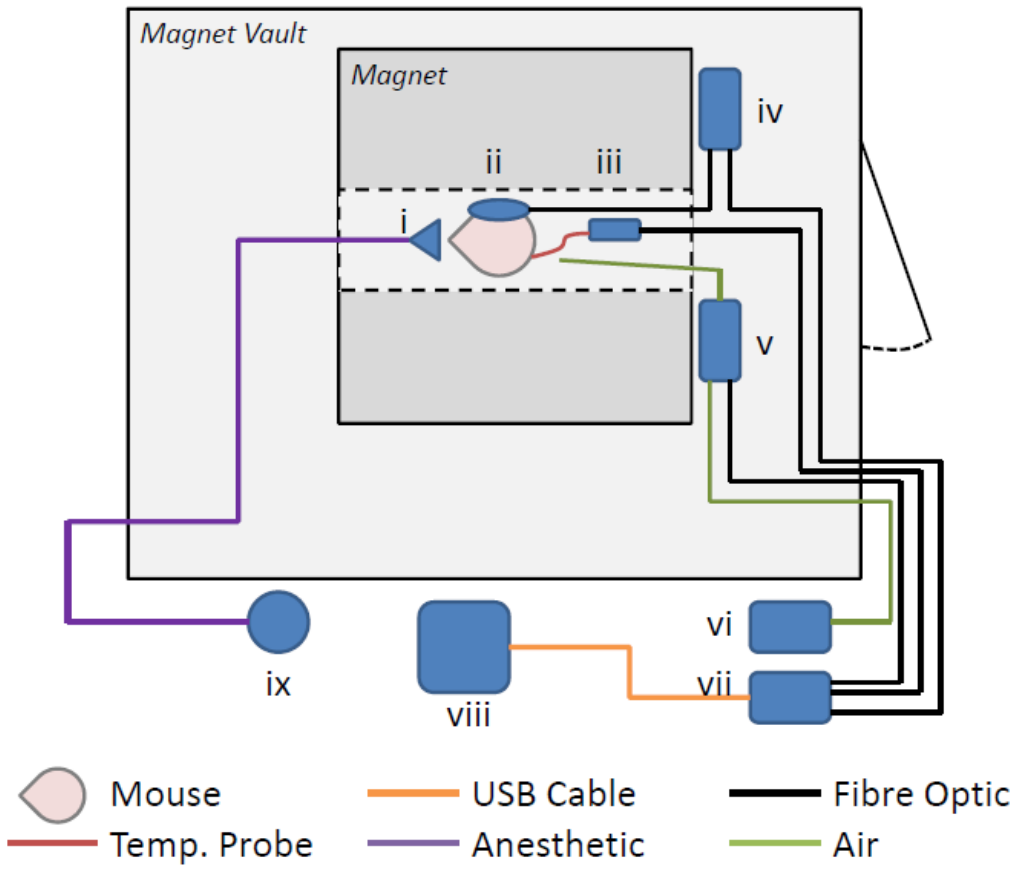

Figure 3.4. Simplified schematic showing key components of the animal monitoring system. In addition to cables and tubing, the following structures are identified: anesthetic nose cone (i), respiration sensor pillow (ii), ECG/temperature module (iii), respiration/blood pressure module (iv), heater module (v), fan module (vi), control module (vii), animal monitoring PC (viii), and anesthetic delivery unit (ix).

Care is taken to ensure consistent setup, monitoring, and maintenance of mice being imaged. When mice require imaging, the following procedure is used:

1) Mice are transferred from the vivarium facility to the 9.4 T lab in HEPA filtered cages.

2) The mouse to be imaged is placed in a clear acrylic “knock-out box” where the initial dose of gas anesthesic is administered. An initial mixture of 5 % isoflurane in oxygen is delivered to the box. This high concentration of anesthetic quickly (elapsed time ≈ 1 min) causes the mouse to lose its ability to keep its balance, after which the anesthetic concentration is reduced to 2.0 %. The respiration rate of mice at this point is typically in the range of 200-250 breaths per minute, or 3-4 breaths per second.

3) Once the rate has slowed to approximately 60 breaths per minute, or 1 breath per second, the mouse is transferred to the semi-cylindrical polystyrene couch MR imaging couch and maintained under anesthetic via a nose-cone delivery device which is placed over the nose and mouth. Isofluorane administration continues at 2%.

4) A small amount of Lacri-lube lubricating ophthalmic ointment (Allergan, Inc., Markham, ON) is applied to the eyes of the mouse. Care is taken to avoid applying lubricant to the snout of the animal as this might obstruct normal breathing.

5) At this time, a heatlamp above the setup area is turned on to keep the mouse warm during imaging preparation. The lamp is positioned approximately 50 cm away from the mouse to ensure comfortable heating without burning.

6) A pneumatic pillow is placed on the mouse's abdomen and secured in place with a strip of Durapore surgical tape (3M Health Care, St. Paul, MN, USA) which wraps over the pillow and completely around the couch. The pneumatic tube which connects to the pillow runs the length of the acrylic platform and is not yet connected to monitoring devices.

7) A thermistor-type temperature probe, covered with the fingertip from a latex glove and lubricated with Lacri-lube, is inserted into the mouse's rectum. Once in place, the probe is secured with a strip of Durapore tape perpendicular to the probe lead and mouse's tail, securing both to the couch. The probe lead is then connected to a battery-powered relay module which converts the measured temperature to a light signal, which will be carried via fiber-optic cable to the animal monitoring station next to the MR operator console.

8) The tumour-bearing limb of the mouse is secured in place by one or two strips of Durapore tape, being careful to not restrict bloodflow to the limb or the tumour. The position of the tumour relative to the end of the

couch is measured and noted. A photograph of a fully-prepared mouse, at this point of the setup is shown in Figure 3.5.

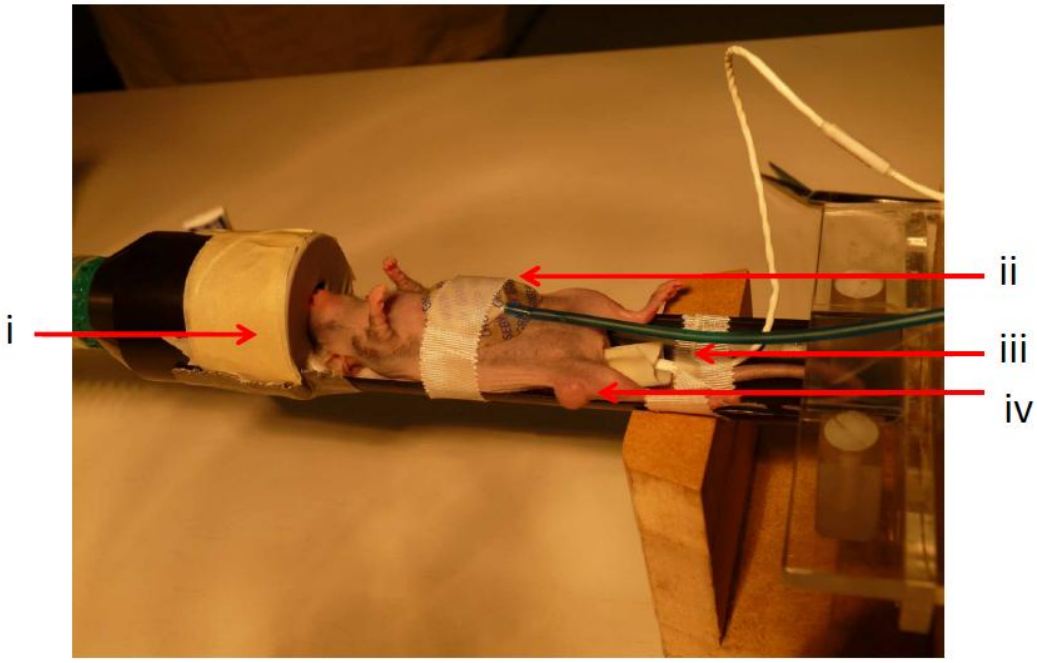

Figure 3.5. Photograph of anesthetized mouse prepared for MR imaging. The mouse is positioned supine on a polystyrene couch while isoflurane anesthetic is delivered via nosecone (i). A pneumatic respiration sensor pillow is placed on the mouse's abdomen (ii), while a thermistor temperature probe is shown (iii) positioned in the mouse's rectum. The tumour xenograft is also visible (iv).

9) The polystyrene couch / acrylic platform complete with mouse and supporting monitoring equipment is transferred into a clear, acrylic cylinder (11 cm inner diameter, 100 cm total length), inside which the 44 mm RF coil is mounted. The cylinder has been designed so that it fits

securely inside the bore of the gradient set, and when fully inserted into the bore the centre of the sensitive volume of the RF coil is located at the centre of the gradient set. The cylinder is also marked in 1.0 cm increments, so that the couch and platform can be translated and the tumour or area of interest in the mouse can be centered within the sensitive volume of the RF coil and in turn the gradient set.

10) The cylinder, containing the platform, monitoring equipment, and mouse positioned within the RF coil, is transferred into the magnet bore. During transfer, flow of anesthetic is interrupted. Immediately after placement in the magnet, anesthetic tubing is reconnected to the nose cone. The anesthetic tubing in the magnet vault originates via the rear wave-guide from a second isoflurane vaporizer, positioned next to the animal monitoring station. This vaporizer mixes anesthetic with both nitrogen and oxygen, with nitrogen run at approximately 150 mL / min and oxygen at 350 mL / min, for a total volume flow rate of approximately 500 mL / min. Isoflurane concentration is controlled manually and is generally within the range of 1.5% - 2.0%.

11) Once the cylinder is positioned within the magnet and anesthesia resumed, final connections for the animal monitoring equipment are made:

a. The pneumatic respiration pillow is connected to the respiration module, just outside of the magnet bore, which communicates the respiration signal via fibre-optic to the animal monitoring station.

b. The hot air tube is connected to the heater located just outside the magnet bore, with the other end near the animal inside the magnet. A fan located outside the magnet vault blows air through tubing fed through the front wave-guide, through the heater, and through the hot air tube to the animal. Power to the heater is controlled by software operating on a feedback loop with the rectal temperature probe.

c. Fibre-optic cables carrying respiration and temperature signals are connected to a control module, which converts the signals for USB input to the PC running the monitoring software.

12) Animal temperature and respiration are now available on the PC at the animal monitoring station. Anesthetic concentration may be increased in response to high respiration rates or decreased in response to low respiration rates.

Typically, a few minutes at the start of monitoring are allowed for the body temperature of the mouse to stabilize at 37^{o}C and for changes in anesthetic concentration to take effect. Refinement is often required over the course of imaging. Target respiration rates are between 60 and 90 breaths per minute.

3.4 Image Acquisition

3.4.1 Imaging preparation: navigation, shimming, and RF calibration

With the mouse anesthetized and positioned such that both the sensitive volume of the RF coil and the tumour are centered relative to the axis of the bore of the gradient set, the RF coil is "tuned and matched" using a RF sweeper probe tuner (Morris Instruments, Inc., Ottawa, ON). Tuning refers to adjusting the resonant frequency of the RF coil to be equal to that of the experimentally determined ^{1}H NMR frequency of the magnet (~400.45 MHz). The frequency is adjusted for both channels of the quadrature coil by means of adjusting sliding contacts which control variable capacitors within the RF coil. Matching refers to impedance matching both channels to match the impedance of the external RF circuits (50 ohms), in order to prevent losses of signal. This is also accomplished by adjusting sliding contacts which control variable capacitors within the RF coil.

Once both tuned and matched, both channels of the RF coil are connected to the RF transmission and reception circuits. The door to the magnet vault is closed.

A localizer scan is run to confirm the position of the tumour and to be used as a guide for navigation of subsequent scans. This sequence consists of three interleaved heavily-T1-weighted (TR = 400 ms, TE = 3 ms) gradient echo (GE) scans, with one 5 mm thick slice each in the transverse, sagittal, and coronal planes. The FOV is large (50 x 50 mm^2, 128 x 128 matrix size). No adjustment of room temperature shim coils is done in advance of this scan, and amplification of transmitted and received RF signals is not optimized, but left at initial settings known to be near optimal for this scan (linear scaling of generated RF pulse shapes = 1.00, amplification of transmitted RF pulses = 20 dB, amplification of received RF signal = 20 dB).

Navigating using the set of localizer images as a guide, a T1-weighted (TR = 1250 ms, TE = 13ms) transverse SE scan is prepared (20 x 1 mm thick slices, no gap between slices, FOV = 35 x 35 mm^2, 128 x 128 matrix size). The centre of the pack of slices is centered on the tumour in the superior-inferior direction, and the FOV is adjusted in the anterior-posterior and left-right directions to ensure the entire mouse and tumour are included. Offsets in all three orthogonal directions are noted. Shimming using room temperature shim coils has still not been done, and RF scaling / amplification settings are still only estimated. This scan, having much thinner slices and a longer TE, generates significantly less RF signal than the localizer sequence, so amplification of the received RF signal is set at 39 dB, which is the maximum available amplification. The scan is then run.

The images acquired with the T1-weighted SE are examined to confirm the tumour is fully within the FOV and centered relative to the slice pack. Another SE scan is then generated, with identical parameters at the previous one. The following parameters are then adjusted: the number of slices is reduced to one, the TR is increased to 3000 ms, and both frequency- and phase-encoding gradients are turned off. The function of the sequence at this point is to apply an excitation pulse to the central 1 mm slice, followed by a refocusing pulse and then acquisition of the echo. Shimming on this central slice is then performed.

The sequence is run in "setup" mode, which allows on-the-fly adjustment of room temperature shim settings and RF scaling and transmit settings. As the shim settings are adjusted, the magnetic field becomes more homogeneous within the sample, and the distribution of resonant frequencies within the sample becomes more homogeneous. This can be visualized by watching the Fourier transform of the acquired signal, which shows the distribution of resonant frequencies within the sample. As the shimming improves, the width of the distribution narrows (see Figure 3.6). Shim settings are adjusted iteratively until the operator deems the sample sufficiently shimmed. Typically, for imaging purposes, only first-order shims are used, initially adjusting the shims in 50 μT/m increments, and later by finer 5 or 10 μT/m increments.

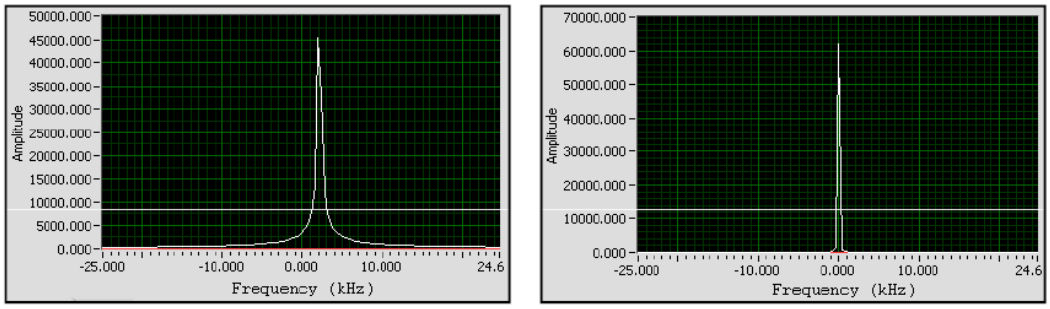

Figure 3.6. Fourier transforms of acquired RF signals from unshimmed (left) and shimmed (right) samples. Signal amplitude is in arbitrary units. The frequency distribution narrows significantly in the shimmed sample and peak amplitude increases (y-axis scale is adjusted). Also note that the receiver frequency is adjusted to centre on the peak of the frequency distribution after shimming.

After shimming is complete, adjustments to the RF transmission and reception circuits are made. First, the NMR frequency used by the system is adjusted to match the peak of the distribution of frequencies within the sample, as determined from viewing the Fourier transform of the acquired signal. This is done by adjusting the "NMR frequency" setting at the user console, which changes the frequency output by the frequency synthesizer.

Secondly, the amplitudes of transmitted RF pulses are calibrated. This ensures that the programmed angle of excitation or refocusing is equal to the angle achieved by the delivered pulse. This can be done in two ways – the pulse shapes can be linearly scaled during preparation of the pulses at the MR console, or the amplification of the output pulse shapes can be adjusted by a variable-

gain amplifier through which the signals pass before reaching the 4 kW RF amplifier. Adjustment of both of these settings is available to the MR operator.

The excitation flip angle of the sequence is set to 90°. The acquired signal should be maximum when the transmitted RF pulse is properly calibrated, as a 90° produces maximum transverse magnetization. In practice, adjustment of the variable gain amplifier is used for a coarse adjustment of the RF pulses, and linear scaling of the pulses is used as a fine adjustment.

After RF calibration is complete on the transmission side, the amplification of the acquired signal is adjusted. This is done by adjusting the setting of a variable gain amplifier through which the signal passes before entering the receiver, so the signal is amplified as much as possible without overloading the receiver. The frequency encoding gradient is turned back on, while leaving the phase encode gradient off. The function of the sequence now is to apply a calibrated 90° excitation pulse, followed by a 180° refocusing pulse, and then acquire the echo while a frequency encoding gradient is applied. This produces a projection through the sample, equivalent to the central line of k-space. The amplifier gain is set to maximum (39 dB) and then reduced as necessary. If the gain is too high and the receiver is being overloaded, the baseline of the projection is affected, creating the appearance of signal where there should be none, as is shown in Figure 3.7. The operator reduces the gain

setting until no distortion of the baseline is visible. The system is now calibrated and ready for quantitative measurement of T2 and ADC.

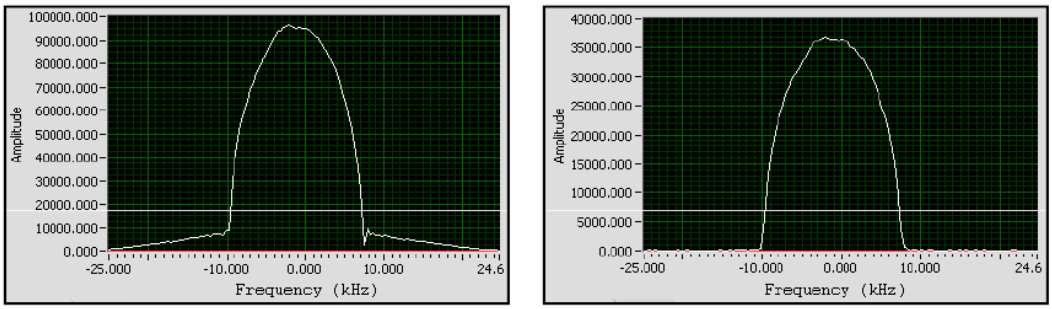

Figure 3.7. Fourier transforms of received RF signals from transverse projections through a spherical object. On the left, receiver amplifier gains are set too high and the receiver is overloaded, resulting in distortion of the baseline on either side of the object. On the right, receiver amplifier gains are properly set.

3.4.2 Acquisition of diffusion-weighted images

A transverse diffusion-weighted spin-echo sequence is prepared with the same geometric parameters that were used in the previous sequence. The DW-SE sequence allows acquisition of multiple scans with different b-values to be run consecutively. The sequence is set to acquire two DW images – the first with a b-value of 50 s/mm^2 and the second with a b-value of 450 s/mm^2.

As discussed elsewhere (6), as well as in Chapter 2, use of a non-zero b-value allows separation of perfusion-related incoherent motion from the calculation of ADC. According to the typical values of perfusion pseudodiffusion coefficient and perfusion fraction, using 50 s/mm^2 as the lower b-value should result in a perfusion contribution to the calculation of ADC of less than 2%.

The choice of 450 s/mm^2 as the higher b-value balances a need for sufficient diffusion-weighted attenuation between low and high b-value images, and a need to retain sufficient SNR in the more heavily weighted images. Additionally, by using longer diffusion times and keeping signal attenuations small, the sensitivity of ADC to measurement technique is reduced (7).

To change b-values, the amplitude of diffusion-sensitizing gradient is varied, keeping diffusion lobe separation Δ and duration δ constant at 10 and 5 ms, respectively. A TR of 3000 ms and a TE of 20 ms are used. 20 ms was used as the TE value because it was the shortest possible TE that could be used and still accommodate the diffusion-sensitizing pulses within the sequence. The shortest possible TE was important for two reasons. One reason is that a short TE results in less T2-weighted attenuation in the image and therefore higher SNR. In both sets of images there will already be diffusion-weighted attenuation reducing SNR, and any unnecessary loss of signal should be minimized. The second reason is that increasing TE increases the degree to which T2-weighting affects the calculation of ADC. The effect of T2-shine-through is well known (8), where in images resulting from DW sequences with longer TEs, tissues with shorter T2 values will appear hypo-intense due to T2-weighted attenuation, which may be mistaken for diffusion-weighted attenuation. Calculation of an ADC map eliminates this effect at the inter-voxel level, but if different tissue compartments within a single voxel (ie. intra vs. inter-cellular water) have

different T2 values, long TE sequences will bias the calculation of ADC for that voxel towards the value of ADC for the tissue with longer T2 (7).

The sequence is run, collecting sets of images at both 50 and 450 s/mm^2, with the diffusion sensitizing gradient in the left-right (*x*) direction. Two more identical sequences are run, with the diffusion-sensitizing gradient in the anterior-posterior (*y*) and superior-inferior (*z*) directions.

3.4.3 Acquisition of T2-weighted images

After all DW images have been acquired, a SE sequence is prepared with the same geometry as the DW sequences. A long TR (3000 ms) and a short TE (13 ms) are set. As with all previous sequences, an imaging bandwidth (BW) of 50 kHz was used. Low imaging bandwidths have the advantage of producing high SNR images. As discussed in Chapter 2, SNR is related to BW according to

$$SNR \propto \frac{1}{\sqrt{BW}}. \tag{3.2}$$

Low imaging bandwidth can be disadvantageous when it increases the minimum achievable TE for a sequence by extending the total time required for frequency-encoding, and when it produces increased distortions related due to susceptibility artifacts in images. The choice of 50 kHz was made as a compromise between these factors after initial imaging experiments.

The sequence with a TE of 13 ms is run, and two identical sequences are produced, with their TEs altered to be 26 and 39 ms. The reasoning for choosing

39 ms as the highest TE value was similar to that used for choosing the highest b-value for the DW-SE images. 39 ms provides strong T2-weighted signal attenuation in the images, but also retains enough signal intensity to produce images of satisfactory SNR. The intermediate image was simply chosen as the midpoint between the high and low TE images. Finally, these last two TE images are acquired, the mouse is removed from the magnet, allowed to recover from the anesthesia and returned to its cage.

3.5 Image analysis

3.5.1 Calculation of ADC values

Image analysis was performed using computer code written in the MATLAB programming language (The MathWorks, Natwick, MA, USA). All DW-SE images were imported, and a voxel-by-voxel analysis was made of the monoexponential decay of the signal S expected as function of increasing b-value of the form

$$S(b) = S(0) \cdot \exp(-b \cdot D). \tag{3.3}$$

Since our method only used two b-values in the calculation of ADC, as has been done by others (6,8-11), the following expression for the measured diffusion coefficient can be derived from Eq. 3.3:

$$D_i = \frac{1}{b_2 - b_1} \cdot ln\left[\frac{S(b_1)}{S(b_2)}\right], \quad i = x, y, z, \tag{3.4}$$

where D_i is the measured diffusion coefficient in a single voxel, along the axis of the applied diffusion sensitizing gradient, which in our case corresponds to either the *x*, *y*, or *z* axes of the magnet system. b_2 is the larger b-value, b_1 is the lesser b-value, and $S(b_2)$ and $S(b_1)$ are the voxel intensities measured for the voxel at two different b-values. The ADC is the linear average of the three directional diffusion coefficients along three orthogonal axes:

$$ADC = \frac{1}{3} \cdot \sum_{i=x,y,z} D_i. \tag{3.5}$$

After this method has been used to calculate ADC for all voxels, ADC maps are produced where voxel intensities are equal to the calculated ADC values in units of $\mu m^2/s$.

It has been demonstrated (12) that there is no statistically significant difference between ADC values measured using two-point diffusion methods compared to techniques using six b-values. The two b-value method was chosen because it reduces the total time required for image acquisition while still providing a reproducible measurement of ADC values.

It is understood that ADC values are dependent on measurement technique, and that the specific methods used to measure ADC can be altered in order to affect the significance of the measured values (7), including the use of higher-than-standard b-values to identify slow-diffusing water molecules bound to macromolecules (13). For the purposes of our experiments, however, our

principle concern was a fast, reproducible measurement of ADC for assessing relative changes in response to therapy, for which the method used was most appropriate.

3.5.2 Calculation of T2 values

T2 values were calculated using MATLAB in a manner similar to that used for ADC values, described in section 3.5.1. Image analysis was performed on a voxel-by-voxel basis, with a fit to the data made of the form

$$S(TE) = S(0) \cdot \exp(-TE/T2), \tag{3.6}$$

where S(TE) is the signal intensity of a given voxel as a function of the echo time in that image S(0) is the signal intensity for the same pixel that would be expected with an echo time of zero. The T2 of every voxel was determined from the least-squares fit of a monoexponential curve to the data, which can be directly calculated. After calculation of T2 for every voxel, T2 maps were produced where voxel intensities were equal to the calculated T2 values in units of ms.

The use of a simple monoexponential fit is consistent with other investigations that have measured T2 response after anticancer therapy (9,14,15). Although it is common to model noise in magnitude MR images as conforming to a normal distribution, the true noise distribution is Rician (16), and therefore signal intensity is not expected to decay to zero with infinite TE, as implied by equation 3.6. Noise in the complex data can add or subtract to signal

magnitude when signal is sufficiently high, but will only add to signal as the signal decays to zero. Gaussian noise in the complex signal translates to Rician noise in the corresponding magnitude image. We have investigated the potential use of other fits, such as the use of a monoexponential fit with a constant offset term C such as

$$S(TE) = S(0) \cdot \exp(-TE/T2) + C, \tag{3.7}$$

to account for this feature of the data but have found fits of this type tend to over-respond to noise in the data and yield less accurate T2 estimates. The echo times used in our measurements are sufficiently short, and the signal in the regions of interest sufficiently high, to make the use of a simple monoexponential fit the most appropriate fit to the data.

To test this conclusion, three uniform images were simulated corresponding to the T2 images we collect at echo times of 13, 26, and 39 ms. The uniform intensity in successive images was adjusted to simulate a uniform object with a T2 of 35.0 ms, which is a typical T2 value for observed tumours. Rician noise was then added to the images. Two curves were then fit to each series of pixels, one using a two-variable fit (equation 3.6), and one using a three-variable fit (equation 3.8). A least-squares fit was used, and in both cases the fit was determined using the "lsqcurvefit" function from the MATLAB optimization toolbox. The resulting distributions of calculated T2 values is

shown in Figure 3.8. Both distributions are centered at 35.0 ms, but the distribution resulting from the two-variable fit is much narrower.

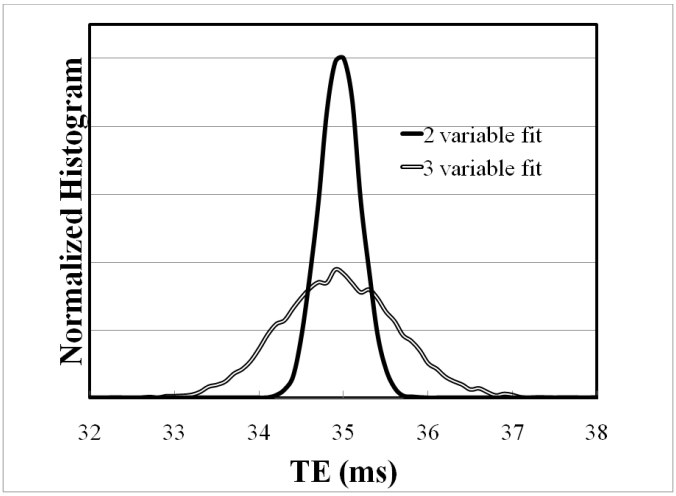

Figure 3.8. Normalized histograms of calculated T2 values for a series of simulated images. The original series of images had a T2 of 35.0 ms. Rician data was added to the images. The distribution resulting from the two variable fit has a mean of 35.0 ms and a standard deviation of 0.24 ms. The distribution resulting from the three variable fit has a mean of 35.0 ms and a standard deviation of 0.68 ms.

3.6 Delivery of radiation treatment

Care is taken to ensure that animal radiation treatments are done in a reproducible manner that delivers an accurate dose to the tumour, maximizing uniformity of dose within the tumour while minimizing dose to critical organs.

3.6.1 Animal setup

When a mouse requires radiation treatment, it is transported in a HEPA filtered cage from the Cross Cancer Institute's vivarium to a Pantak orthovoltage

x-ray unit (Pantak, Inc, Brantford, CT). The following procedure is used for setup of all mice that receive radiation treatment:

1) The mouse to be treated is moved to the same "knock-out box" used in the setup for MR imaging described in section 3.3. Once in the box, a mixture of 5% isoflurane in oxygen is delivered to the box. After approximately one minute, the mouse loses its ability to keep its balance, and the anesthetic concentration is reduced to 2.0%.

2) Once respiration has slowed to approximately 60 breaths per minute, the mouse is removed from the box and placed prone on top of a 10 cm stack of Solid Water (Best Medical, Nashville, TN, USA), a plastic material designed to be radiologically equivalent to water. The Solid Water is wrapped with Saran-Wrap for purposes of hygiene. A heatlamp is positioned approximately 50 cm away from the Solid Water to keep the animal warm during setup and radiation treatment.

3) A small amount of Lacri-lube lubricating ophthalmic ointment is applied to the eyes of the mouse. This step must be done quickly as the mouse is not breathing anesthetic during this time.

4) For the duration of treatment, the animal is maintained on 2% isoflurane delivered via a nose cone.

5) The tumour-bearing leg of the mouse is extended away from the body and held in place using Durapore surgical tape. A 1 mm-thick sheet of lead is placed under the body of the mouse, in order to reduce body dose from scattered radiation.

6) Small pieces of Superflab plastic bolus material (Radiation Products Design, Albertville, MN, USA) are placed horizontally around the tumour. The purpose of the bolus material is to provide material off of which radiation can scatter, improving the uniformity of dose to the tumour.

7) The treatment unit is positioned for radiation delivery:
    a. A 200 kVp filter is placed within the filter tray of the unit. This consists of a 0.35 mm layer of copper and a 1.5 mm layer of aluminum.
    b. A collimating cone with a 2.2 cm diameter base is fitted to the unit below the filter tray. The length of the cone is such that the base of the cone is exactly 30 cm from the x-ray target.
    c. The unit is rotated so that the central axis of the photon beam will be vertically downward. The unit is translated so that the

base of the cone is directly over top of the tumour to be treated.

d. It is visually confirmed that the tumour falls completely under the span of the base of the cone. The distance between the surface of the tumour to the base of the cone should be as small as possible. This distance is visually estimated. A photograph of a mouse in the final stages of pretreatment positioning is shown in Figure 3.9.

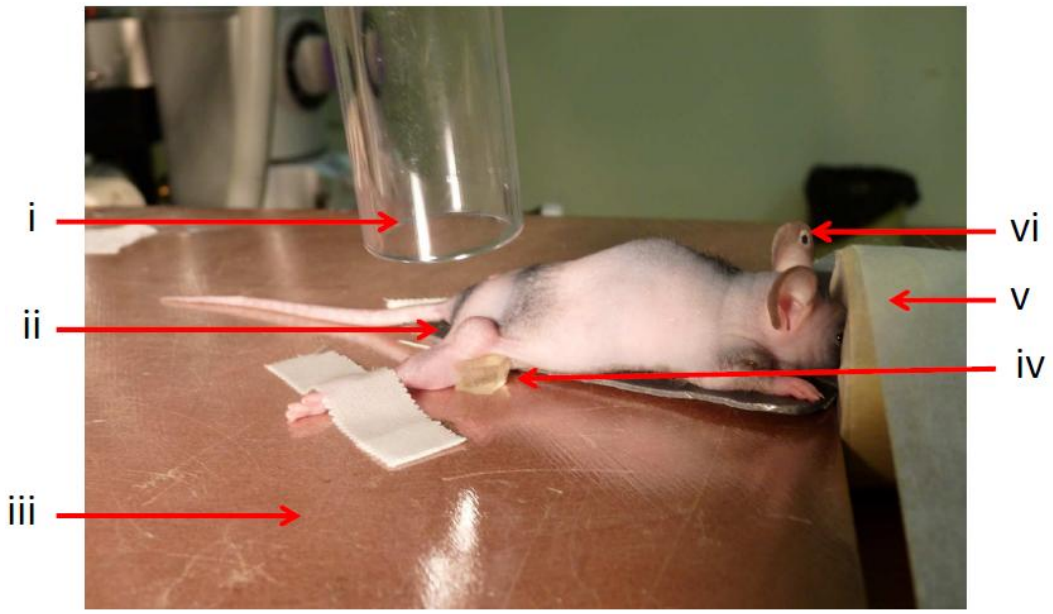

Figure 3.9. Photograph of mouse being prepared for radiation treatment. The 2.2 cm diameter collimating cone (i) is being lowered into place above the tumour (ii), with the mouse positioned prone on a 10 cm-thick stack of solid water (iii). A single piece of Superflab bolus material is in place (iv). More will be added before radiation delivery. The anesthetic nosecone is visible (v), as is the identifying ear-punch on the mouse's left ear (vi).

8) The door to the radiation treatment vault is closed. At this point, the mouse is observed via an in-vault video. Knowing the desired dose to the tumour, and the offset distance between the tumour surface and base of the collimating cone, the required number of monitor units (MUs) are determined from a precalculated table (see section 3.6.2).

After the full dose has been administered, delivery of anesthetic is stopped and the mouse is allowed to recover, placed in its cage, and returned to the vivarium.

3.6.2 Dosimetry calculations

Calculations of radiation dose delivered to the tumour xenografts are based on dosimetry measurements made by medical physicists at the Cross Cancer Institute. The orthovoltage unit used in the treatments described in section 3.6.1 is calibrated to deliver dose at a rate of 1 cGy per monitor unit (MU) to a piece of tissue in air, at the end of a 10 x 10 cm^2 applicator, 30 cm from the x-ray source. To calculate the dose to tissue under a different collimator, at a certain depth, surrounded by tissue, not air, and at distances other than 30 cm, this dose rate must be multiplied by several measured factors that relate the various geometries.

Relative output factor (ROF) is the ratio of dose to tissue in air under a given applicator or collimator to the reference dose under a 10 x 10 cm^2

applicator. Backscatter factor (BSF) is the ratio of dose to tissue for a given field size when directly on top of a water-equivalent scattering material to the reference dose to tissue in air at the same field size. Percent depth dose (PDD) is the ratio of dose to a piece of tissue at a given depth in water for a given field size to the dose to a piece of tissue at a reference depth in water for the same field size. The reference depth is the depth at which the dose is maximum. For a 200 kVp field, the reference depth at the surface, or zero depth. Finally, the dose rate falls off proportional the inverse square of the distance from the radiation source to the surface of the irradiated body. The formula to calculate the dose rate D' for a piece of tissue, submerged in water at a given depth d, is given by:

$$D'\left[\frac{cGy}{MU}\right] = 1\ \frac{cGy}{MU} \cdot ROF \cdot BSF \cdot PDD(d) \cdot \left(\frac{30\ cm}{30\ cm + x}\right)^2, \tag{3.8}$$

where *x* is the distance from the end of the applicator to the surface of the water, and ROF, BSF, and PDD are all dependent on the beam energy and applicator used.

Values of ROF, BSF, and PDD were taken from clinical dosimetry measurements. The measured ROF for the 2.2 cm applicator with a 200 kVp beam is 0.936. A plot of 200 kVp backscatter factors as a function of field size is shown in Figure 3.10. Interpolating from this plot gives a backscatter factor for a 2.2 cm diameter conical applicator of 1.08.

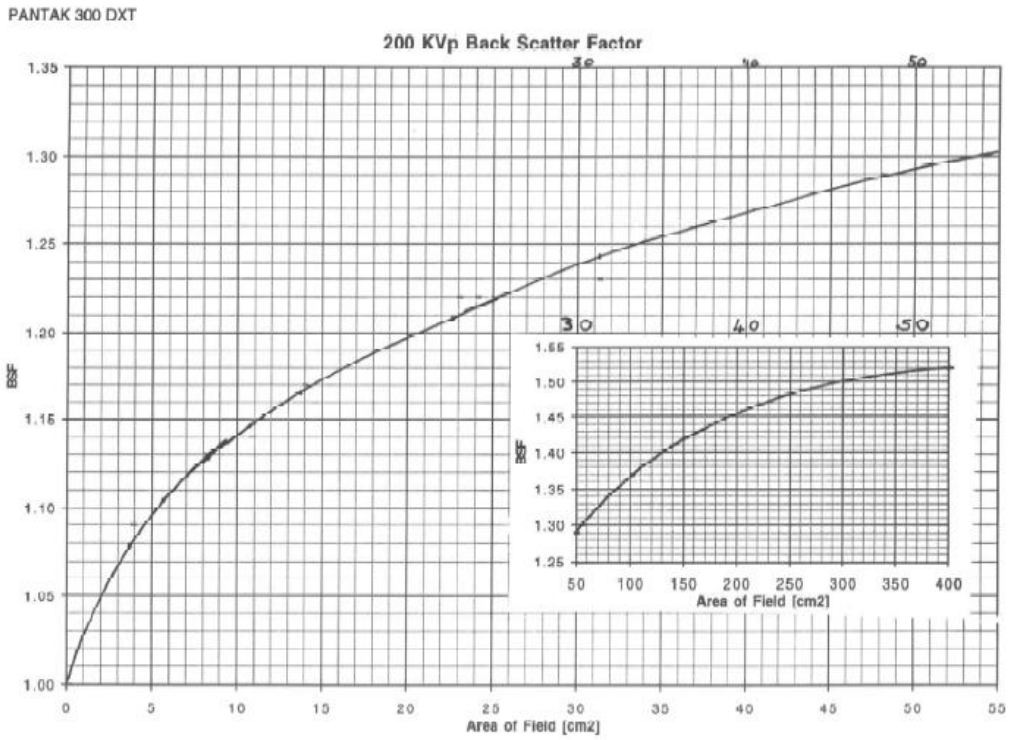

Figure 3.10. A plot of measured backscatter factor (BSF) for a 200 kVp x-ray beam as a function of field size.

A plot of PDD curves for a 200 kVp beam using various applicators is shown in Figure 3.11. Since the average treated tumour has a total thickness of approximately 5-6 mm at the time of treatment, a PDD value of 0.97 was interpolated assuming a depth to the centre of the tumour to be approximately 2.5 mm.

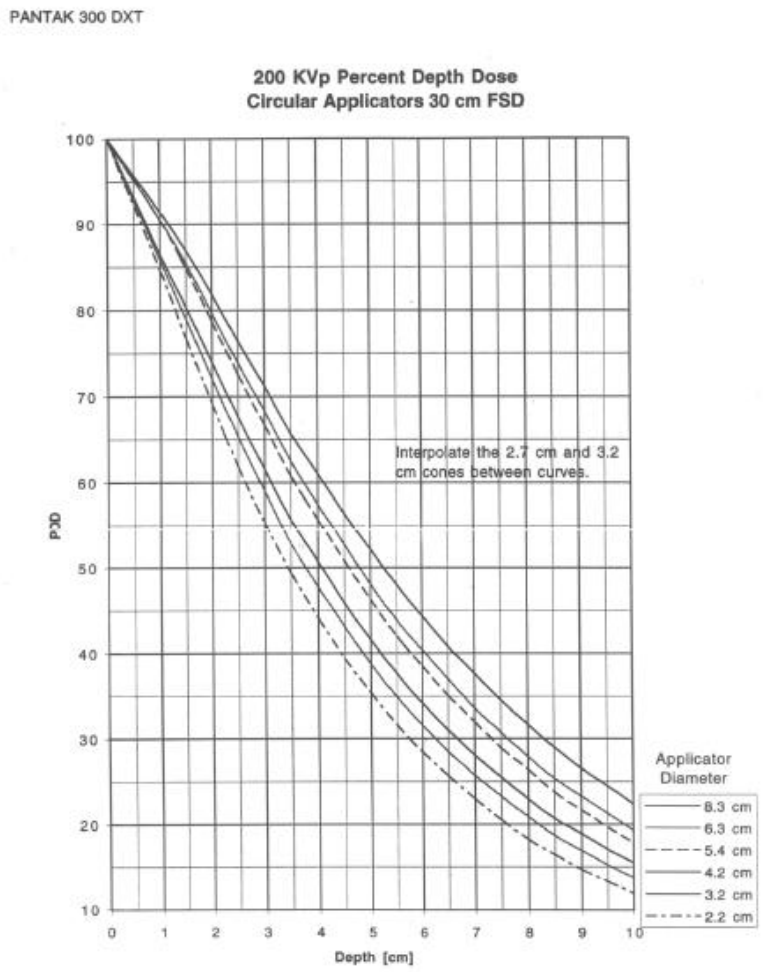

Figure 3.11. Percent depth dose (PDD) curves for a 200 kVp photon beam using various applicators.

Using these values for ROF, BSF, and PDD, dose rate to the centre of the tumour was calculated for the 200 kVp beam using the setup as described in section 3.6.1, and the required number of monitor units to deliver various doses of interest was calculated for various applicator-to-surface separations. These results are summarized in Table 3.2, and were used for dose delivery during the course of these radiation experiments.

Table 3.2. Required number of monitor units (MUs) to deliver different doses to the centre of a tumour at various applicator-to-surface distances. Calculation assumes a tumour diameter of 5 mm, use of 200 kVp beam with a 2.2 cm diameter conical applicator. Monitor units actually delivered during treatment were rounded to the nearest integer, as fractions of MUs cannot be delivered.

Distance	Desired Dose (cGy)				
(mm)	50	200	267	400	800
0	51.0	204.0	272.0	407.9	815.9
1	51.2	204.6	272.9	409.3	818.6
2	51.3	205.3	273.8	410.7	821.3
3	51.5	206.0	274.7	412.0	824.0
4	51.7	206.7	275.6	413.4	826.7
5	51.8	207.4	276.5	414.7	829.5

3.7 Special case: application of ligature

Experiments were performed where ischemia (reduced blood flow) and hypoxia (reduced tissue oxygenation) were induced by application of a suture-based ligature around the tumour bearing leg above the tumour. This technique has been widely used and has been well-documented (17-23).

3.7.1 Technique development and safety

The technique for application of the ligature was developed in consultation with veterinary technicians and a veterinary pathologist. Prior to

attempting the technique, the veterinary pathologist identified three days after treatment as the most important time point for assessing damage to the mouse leg from the ligature. Earlier than the three day mark, temporary damage such as bruising would be most prominent, and more serious biochemical damage would have yet to manifest itself physically.

Two healthy mice were selected and each had a ligature applied while under anesthesia using the technique described below (section 3.7.2). Three days later the mice were euthanized in the presence of a veterinary pathologist. The mice were dissected and both legs of each mouse were examined and compared. Tissue samples from legs above and below the ligature location were taken for histological examination.

After gross inspection and microscopic examination, the pathologist was unable to discriminate between healthy muscle and muscle taken from below the point at which the ligature was applied. The pathologist concluded that the application of the ligature for 15 minutes did no long-term damage to the leg of the mouse.

3.7.2 Ligature Procedure

The following procedure is used for application of the ligature:

1) The mouse on which the procedure is to be performed is anesthetized on 2.0 % isoflurane in oxygen gas. Depth of anesthesia is confirmed by

visual observation of mouse respiration rate, as well as manual testing of the pedal reflex, where a sharp pinch is applied to a foot of the mouse. Any reflexive pull of the foot indicates anesthesia is too light.

2) A sliding, noose-style knot is tied around the leg to be ligated using a sterile polypropylene suture. The noose is positioned as high up the leg as possible, and loosely tightened to hold it in position.

3) The standing end of the suture is wrapped around the index and middle fingers of one hand, a pair of forceps is used to slide the knot and tighten the ligature as much as possible. A photograph of the ligature before and after being tightened is shown in Figure 3.12.

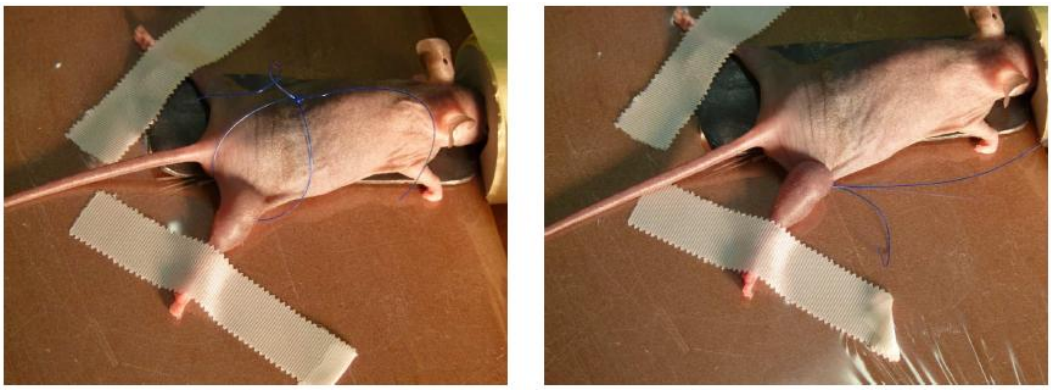

Figure 3.12. Photographs before (left) and after (right) application of suture ligature. The loop of suture is moved into place around the tumour-bearing leg above the tumour (left), and then cinched tight (right).

4) After tightening of the ligature, the leg below the ligature becomes cyanotic within one minute. The ligature is left in place for 15 minutes. In cases where radiation is being delivered while the ligature is in place,

10 minutes is allowed between application of the ligature and radiation delivery, to reduce the supply of oxygen available to the tumour cells.

5) After the ligature has been in place for 15 minutes, it is removed using a #11 stainless steel scalpel blade. This blade is triangular in shape with a pointed end, which is carefully slid underneath the ligature. When the blade is twisted away from the skin, the suture is cut and the ligature can be removed.
6) The mouse is kept under anesthesia for 5 minutes after the removal of the ligature, and then allowed to recover from the anesthesia and returned to its cage.

3.8 Extraction of tumours for histology

A number of tumours were excised for histological analysis after euthanization. The purpose of this work is to further our understanding of the mechanisms responsible for the parametric changes observed in our MR studies. Due to the temporal evolution of these changes, tumours were harvested at various time points after treatment and prepared for a number of histological evaluations.

3.8.1 Hypoxyprobe-1 injection

Prior to euthanization, the mouse to be euthanized is injected with a chemical agent that binds to hypoxic tissues. Sufficient time is allowed for unbound agent to be cleared from the body before euthanization to prevent

non-specific binding after death. The agent forms covalent bonds with hypoxic cells. Specifically, adducts are formed with thiol groups within proteins, peptides, and amino acids when sufficiently low oxygen concentrations are present (pO_2 < 10 mmHg) (24). Bound agent is cleared from tissue when metabolized. Use in dogs has shown only a 10% decrease in binding between 24 hours and 72 hours after injection (25). When the tumour is sectioned on to microscope slides, hypoxic regions can be stained for and identified.

A solution of Hypoxyprobe-1 hypoxia marker (pimonidazole hydrochloride; HPI, Inc., Burlington, MA, USA) was prepared at a concentration of 3.0 g/L. The manufacturer's recommendation for dose in mice is approximately 60 mg per kg of body weight, injected 1-2 hours prior to euthanization (24). Average mouse body weight was in the range of 23-25 g, requiring injection of 0.46-0.50 mL of the 3 g/L solution. For the sake of simplicity, each mouse to be euthanized was given an injection of 0.50 mL of Hypoxyprobe-1 via intraperitoneal injection using a 1.00 mL syringe with a 31-gauge hypodermic needle. The injected marker was allowed to circulate for 90 minutes prior to euthanization. This allows the marker to bind to hypoxic tissues, and allows the body of the mouse to clear residual marker from the body. Residual systemic presence of Hypoxyprobe-1 at the time of euthanization could result in binding to tissues that only become hypoxic after euthanization.

3.8.2 Euthanization and tumour removal

When 90 minutes have elapsed after the injection of the hypoxia marker, the mouse euthanized in a carbon dioxide chamber, where a slow flow of CO_2 results in rapid loss of consciousness followed by death.

The carcass is then transferred to a biosafety hood for removal of the tumour. The carcass is placed supine, in a position mimicking that used for MR imaging. A #11 stainless steel scalpel is used to make a tumour-spanning incision through the skin. The thin membrane encapsulating the tumour is carefully cut away, being careful to not damage the tumour. Any connective tissue holding the tumour in place is cut. Finally, the tumour is sliced in half with the scalpel, with the plane of the cut matching the transverse plane from MR imaging as closely as possible. The tumour halves are then placed in a plastic histology cassette with the cut-face down. The cassette is snapped closed and submerged in a neutral-buffered 10% Formalin (3.7% formaldehyde; Fisher Scientific, Pittsburgh, PA, USA) solution, which serves as a fixative, halting ongoing biochemical reactions in the tissue. The tissue cassette is stored in the Formalin solution for a minimum of 24 hours before being transferred to the pathology lab for wax embedding and preparation of microscope slides.

3.8.3 Wax embedding and slide preparation

After a minimum of 24 hours of exposure to the Formalin fixative, the cassette containing the tumour tissue is transferred to the pathology lab at the

Cross Cancer Institute. The tissue is placed in a tissue processor (Somagen Diagnostics, Edmonton, AB) where it is dehydrated before being embedded in a block of paraffin wax. The effects of the fixation and embedding process include shrinkage of tissue and removal of fat.

Tissue sections are cut from the paraffin as required. Beginning at the surface of the scalpel cut-plane, a rough cut is performed using a microtome (Thermo Fisher Scientific, Waltham, MA, SA) until the entire face of tissue is exposed, to avoid only sectioning the leading edge of the tumour. Multiple 4 μm thick sections are then cut, and sections mounted on electrostatically charged glass slides (Thermo Fisher Scientific, Waltham, MA, SA).

One section of each tumour is stained with a hematoxylin and eosin (H&E) stain using an automated staining process. This is the most widely used stain for medical diagnostic purposes. H&E stains structures containing nucleic acids blue, and structures containing proteins red.

Remaining slides are dried on a ventilated rack at room temperature and are placed in an oven at 60°C for 2 hours, before being sent for further staining as requested by a consulting pathologist.

Additional staining was performed by the pathology department. A periodic acid-Schiff (PAS) stain was performed which stains for carbohydrate macromolecules (26). A PAS diastase (PAS+D) stain was performed, where the

addition of diastase digests glycogen in the sample, serving as a negative control (glycogen will stain positive in a PAS section, but will not show in a PAS+D section) (26). Finally, one section of each tumour is stained with an antibody which recognizes the presence of Hypoxyprobe-1 adducts within cells. This stain is used to identify which regions of a section were hypoxic.

References

1. Charles River NIH-iii Nude Mouse Overview. [Online]. Cited 2009. Available from: *http://www.criver.com/SiteCollectionDocuments/rm_rm_c_NIH_III_nude_mice.pdf*.

2. Ossowski L, Reich E. Changes in malignant phenotype of a human carcinoma conditioned by growth environment. *Cell.* 1983: p. 323-333.

3. Franko A, Parliament M, Allalunis-Turner J, Wolokoff B. Variable presence of hyypoxia in M006 human glioma spheroids and in spheroids and xenografts of clonally derived sublines. *Br J Cancer.* 1998: p. 1261-1268.

4. Olfert ED, Cross BM, McWilliam AA. Guide to the Care and Use of Experimental Animals. Saskatoon, SK: *Canadian Council on Animal Care;* 1993.

5. Shen J, Rycyna RE, Rothman DL. Improvements on an in vivo automatic shimming method (FASTERMAP). *Mag Reson Med.* 1997: p. 834-839.

6. Le Bihan D, Breton E, Lallemand D, Aubin ML, Vignaud J, Laval-Jeantet M. Seperation of diffusion and perfusion in intravoxel incoherent motion MR imaging. *Radiology.* 1988: p. 497-505.

7. Szafer A, Zhong J, Anderson AW, Gore JC. Diffusion-weighted imaging in tissues: theoretical models. *NMR in Biomed.* 1995: p. 289-296.

8. Nishimura DG. Principles of Magnetic Resonance Imaging. Palo Alto, CA: *Stanford University Press*; 1996.

9. Sun Y, Mulkern RV, Schmidt K, Doshi S, Albert MS, Schmidt NO, et al. Quantification of water diffusion and relaxation times of human U87 tumors in a mouse model. *NMR in Biomed.* 2004: p. 399-404.

10. Chenevert TL, Stegman LD, Taylor JMG, Robertson PL, Greenberg HS, Rehemtulla A, et al. Diffusion magnetic resonance imaging: an early surrogate marker of theapeutic efficacy in brain tumors. *J Natl Cancer Inst.* 2000: p. 2029-2036.

11. Schepkin VD, Chenevert TL, Kuszpit K, Lee KC, Meyer CR, Johnson TD, et al. Sodium and proton diffusion MRI as biomarkers for early therapeutic

response in subcutaneous tumors. *Mag Res Imaging.* 2006: p. 273-278.

12. Burdette JH, Elster AD, Ricci PE. Calculation of Apparent Diffusion Coefficients (ADCs) in Brain Using Two-Point and Six-Point Methods. J *Comput Assist Tomogr.* 1998: p. 792-794.

13. Roth Y, Tichler T, Kostenich G, Ruiz-Cabello J, Maier SE, Cohen JS, et al. High-b-value diffusion-weighted MR imaging for pretreatment prediction and early monitoring of tumor response to therapy in mice. *Radiology.* 2004: p. 685-692.

14. Henning EC, Azuma C, Sotak CH, Helmer KG. Multispectral quantification of tissue types in a RIF-1 tumor model with histological validation. Part I. *Mag Reson Med.* 2007: p. 501-512.

15. Henning EC, Azuma C, Sotak CH, Helmer KG. Multispectral tissue characterization in a RIF-1 tumor model: monitoring the ADC and T2 responses to single-dose radiotherapy. Part II. *Mag Reson Med.* 2007: p. 513-519.

16. Gudbjartsson H, Patz S. The Rician distribution of noisy MRI data. *Mag. Reson. Med.* 1995: p. 910-914.

17. Moulder JE, Rockwell S. Hypoxic fractions of solid tumors: experimental

techniques, methods of analysis, and a survey of existing data. *Int. J. Radiat. Oncol. Biol. Phys.* 1984: p. 695-712.

18. Stevens G, Joiner M, Joiner B, Johns H, Denekamp J. Radiosensitization of mouse skin by oxygen and depletion of glutathione. *Int. J. Rad. Oncol. Biol. Phys.* 1995: p. 399-408.

19. Kataoka T, Mizuguchi Y, Yoshimoto M, Taguchi T, Yamaoka K. Inhibitory effects of prior low-dose x-irradiation on ischemia-reperfusion injury in mouse paw. *J. Radiat. Res.* 2007: p. 505-513.

20. Lu X, Hamilton JA, Shen J, Pang T, Jones DL, Potter RF, et al. Role of tumor necrosis factor-a in myocradial dysfunction and apoptosis during hindlimb ischemia and reperfusion. *Crit. Care Med.* 2006: p. 484-491.

21. Kuroda M, Inamura K, Tahara S, Kurabayashi Y, Akagi T, Asaumi J, et al. A new experimental system for irradiating tumors in mice using a linear accelerator under specific pathogen-free conditions. *Acta. Med. Okayama.* 1999: p. 111-118.

22. Urano M, Nishimura Y, Kuroda M, Reynolds R. Are hypoxic cells critical for the outcome of fractionated radiotherapy in a slow-growing mouse tumor? *Radiother. Oncol.* 1998: p. 221-228.

23. Moulder JE, Rockwell S. Tumor hypoxia: its impact on cancer therapy. *Cancer Metastasis Rev.* 1987: p. 313-341.

24. Hypoxyprobe. [Online]. Cited 2009. Available from:

http://www.hypoxyprobe.com.

25. Azuma C, Raleigh JA, Thrall DE. Longevity of pimonidazole adducts in spontaneous canine tumors as an estimate of hypoxic cell lifetime. *Radiat. Res.* 1997: p. 35-42.

26. Bancroft JD, Cook HC. Manual of histochemical techniques and their diagnostic application New York, NY: *Churchill Livingstone*; 1994.

Chapter 4: ADC and T2 Response after Single Fraction Radiotherapy

Magnetic resonance imaging was used to study the response of human glioma tumour xenografts to single fraction radiotherapy, with investigation of both temporal and dose dependence of induced changes in volume, ADC, and T2. This chapter discusses the results of these experiments. A summary of these findings has been published after peer-review (1).

4.1 Introduction

Conventional imaging to assess therapeutic response based on volume changes is limited by the time frame over which these changes occur. This in turn places a limit on the utility of this technique to guide patient therapy at an early stage of treatment (2-4). In addition to conventional imaging, a diverse

selection of MRI techniques have been used to monitor the growth and treatment response of tumours to various therapies both in the laboratory and in the clinic. These techniques include the use of targeted contrast agents (5,6), ^{1}H magnetic resonance spectroscopy (MRS) which can be used to monitor the relative concentrations of metabolites in both tumour and surrounding tissues, and ^{31}P MRS which can be used to directly monitor the metabolic and pH status of the tumour and the surrounding microenvironment (7).

The quantitative measurement of relaxation times and water diffusion has been shown to be a powerful method of assessing tumour behavior and evaluating the performance of different therapeutic approaches. Transverse relaxation time (T2) of tissue has been shown to change in response to physiological changes in tissue (8,9). The apparent diffusion coefficient (ADC) is a measure of diffusion in tissue and has been shown to be sensitive to changes in tissue physiology including changes in cellular size, extracellular volume, and membrane permeability (2,3,8,10). In animal models, changes in both T2 and ADC have been reported to correlate with positive tumour response to various anticancer therapies (2,3,9-16) and in the case of certain chemotherapies, dose-dependent changes in ADC have been observed (10-12). Recent human studies have sought to determine whether ADC changes can be used to distinguish response versus nonresponse (2,3,17-20). Investigations into the

pathophysiological causes leading to changes in T2 and diffusion values are also underway (4,21).

The objectives of this work were to use MRI methods to detect and quantify changes induced in tumour tissue after single fraction radiotherapy. Specifically, changes in mean tumour T2 and ADC were measured after different doses of radiation, with attention to the temporal and dose dependence of these parameters.

4.2 Methods

NIH-iii nude mice of approximately 6 weeks of age were obtained from Charles River Laboratories (Wilmington, MA, USA). Human glioblastoma multiforme (GBM) cells of the line M006xLo (22) were used to initiate tumour xenografts as described in section 3.1.

Tumours were measured using digital caliper and tumour volumes were estimated assuming the tumour shape to be ellipsoid. Tumours were allowed to grow until they reached a volume of approximately 150 mm^3, at which point the tumours (six per group) were treated with a single dose (50, 200, 400, or 800 cGy) of 200 kVp x-rays from a Pantak orthovoltage unit (Pantak, Inc., Brantford, CT, USA) according to the procedure described in section 3.6.

Mice underwent MRI pretreatment and at multiple time points after treatment according to the imaging procedure described in detail in sections 3.3

and 3.4. Two series of images were acquired. The first series collected diffusion-weighted spin-echo (DW-SE) images with both low and high b-value. DW-SE images were acquired with the diffusion-sensitizing gradient applied along the three orthogonal axes of the magnet coordinate system. The second series of images were spin-echo (SE) images with increasing echo times (TEs) (increasing T2-weighting).

All MRI experiments were performed using the 9.4 T MRI system at the Cross Cancer Institute described in section 3.2 – a 21.5 cm horizontal bore magnet equipped with a 12.0 cm inner diameter gradient set capable of producing 400 mT/m peak gradient strength (Magnex Scientific, Oxford, UK) interfacted to a TMX console (National Research Council of Canada Institute for Biodiagnostics – West, Calgary, AB). A 44 mm inner diameter birdcage coil was used for RF excitation and reception.

The first experimental group was treated with the highest radiation dose – a single fraction of 800 cGy – to confirm that there was an observable effect before proceeding with the other treatment groups. This group was imaged immediately before treatment and 24, 48, and 72 h post-treatment, spanning the time frame over which we expected to see T2 and ADC response. A final, long-term follow-up exam was performed at 14 days post-treatment. Subsequent treatment groups had the spacing of exams adjusted based on results from the initial group to better resolve treatment response. The 400 cGy

group had images taken pretreatment and at 1, 2, 3, 5, and 14 days after treatment. The final three groups (200 cGy, 50 cGy, and untreated control) had images taken pretreatment and at 1, 3, 5, 7, 11, and 14 days after treatment. The data resulting from the above examinations were used for publication purposes (1). Afterwards, when frequent comparisons were needed to the 800 cGy data, an additional group of six mice were treated with 800 cGy and with this group the timing of imaging sessions was chosen to match the schedule used for the 200 cGy, 50 cGy, and control groups. This data is presented in this chapter.

Image analysis was performed using code written in the MATLAB programming language (The MathWorks, Natwick, MA, USA) as described in section 3.5. ADC and T2 maps were generating by performing a pixel-by-pixel analysis. ADC maps were produced by fitting DW-SE data with a monoexponential decay of the form

$$S(b) = S(0) \cdot \exp(-b \cdot D), \tag{4.1}$$

where S(b) is the signal in a given pixel as a function of b-value, S(0) is the signal intensity expected in the pixel for an image with no diffusion-weighting (b = 0), and D is the diffusion coefficient measured in the voxel, along the axis of the applied diffusion sensitizing gradient. The ADC is then the linear average of the measured diffusion gradient in three orthogonal directions.

T2 maps were produced by fitting the T2-weighted data with a monoexponential decay of the form

$$S(TE) = S(0) \cdot \exp(-TE/T2), \quad (4.2)$$

where S(TE) is the signal in a given pixel as a function of TE, S(0) is the signal expected in the voxel for an image with TE = 0.

Each set of maps was studied qualitatively and contours were drawn on the SE images with shortest TE to define the volume of each tumour. These images were used for tumour delineation because they allowed good visualization of the tumour and did not unnecessarily bias the placement of the contours toward exclusion of regions of high ADC or low TE, as might have been the case with the use of diffusion- or T2-weighted images. The contour can be viewed overlaid on top of images from each acquired image. At no time was significant tumour movement and / or need to refine the contours between images detected.

The MATLAB program then extracted ADC and T2 values for all voxels within the tumour so that the characteristics of the distributions could be analyzed.

4.3 Results

Tumour growth measurements showed a roughly linear increase in volume prior to radiation treatment. Figure 4.1 shows the average tumour

volumes as a function of time for the five different treatment groups. Post-treatment growth rate was dose dependent, but remained approximately linear as demonstrated in Figure 4.2. Average growth rates as determined by the slope of the approximating linear functions for each treatment group are given in Table 4.1. Not surprisingly, the control group showed the highest growth rate, as the growth of that group was not checked by therapeutic intervention. Dose groups at 50 cGy, 200 cGy, and 400 cGy showed inhibited growth, while the 800 cGy group showed shrinkage in the average tumour volume over time.

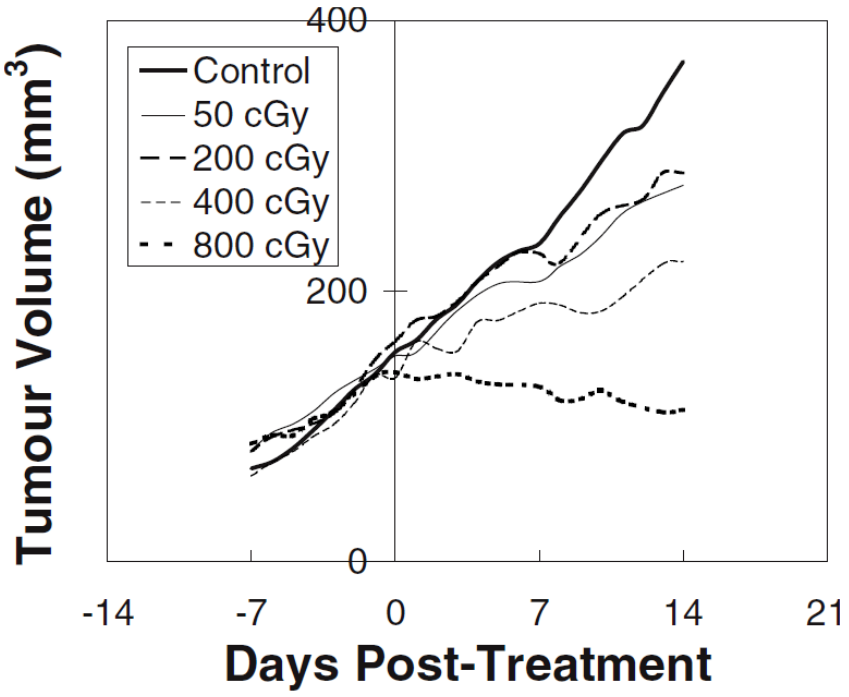

Figure 4.1. Caliper-measured tumour volume for five different treatment groups for the period beginning 7 days prior to treatment and ending 14 days after treatment with radiation.

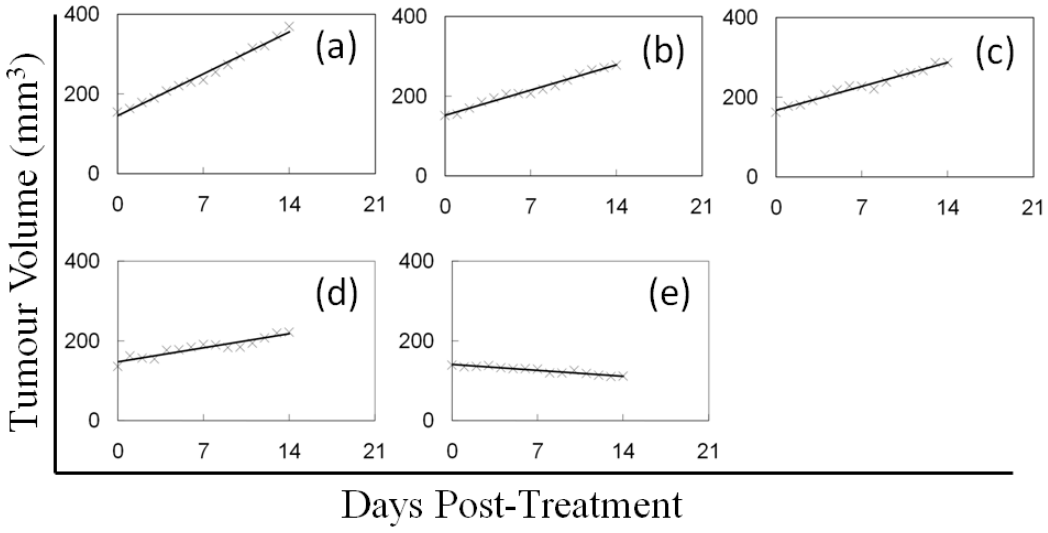

Figure 4.2. Tumor volumes from time of treatment to 14 days post-treatment. Measured data is shown with symbols (×), and linear approximations are given by the solid lines. (a) Untreated group, (b) 50 cGy group, (c) 200 cGy group, (d) 400 cGy group, (e) 800 cGy group.

Table 4.1. Linear growth rates and standard error post-treatment for the five treatment groups as determined by a least-squares fit to the caliper-measured tumour volume data.

Delivered radiation dose (cGy)	Linear growth rate ± SE (mm^3 / day)	R^2 value from fit
0	15.0 ± 2.0	0.987
50	9.1 ± 1.3	0.983
200	8.6 ± 1.5	0.973
400	5.0 ± 1.2	0.886
800	-2.0 ±0.5	0.903

Figure 4.3 compares a proton density image and T2 and ADC map representations of the same transverse slice through a tumour. Based on a qualitative, visual inspection of images and T2 and ADC maps, it is clear that both maps show more heterogeneity than the proton density image, and that while there are features present in both the proton density map and corresponding parameter maps, there are also features unique to a given map.

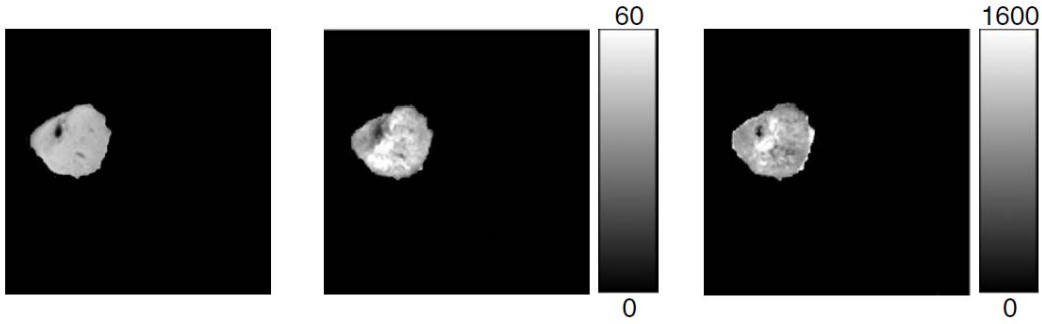

Figure 4.3. Three images of the same transverse slice through an untreated control tumour. All images were masked using the contour of the tumour drawn on the first image. From left to right: Proton density image (TE = 13 ms, TR = 3000 ms), T2 map, ADC map. The FOV for each image is 35.0 × 35.0 mm2 (128 ×128 pixels), with a slice thickness of 1.0 mm. The color bar for each map is linear. The T2 map is in units of ms and the ADC map is in units of μm2 / s.

Figure 4.4 shows the mean time-dependent change in T2 measured for each treatment group. There was a statistically significant ($p < 0.05$) increase in relative T2 for the highest dose group (800 cGy) at 1, 3, and 5 days after treatment, with the T2 appearing to peak at 3 days after treatment with a relative increase in T2 of 7.5%. At 14 days after treatment, the mean T2 of the 800 cGy-treated tumours had dropped to 7.9% below the pre-treatment

average. The 200 cGy group showed a statistically significant elevation in T2 relative to the control at 1, 5, and 7 days after treatment, and a significant drop in T2 at 14 days post-treatment. Statistical significance was tested using multiple two-sample t-tests to compare each treated group to the control.

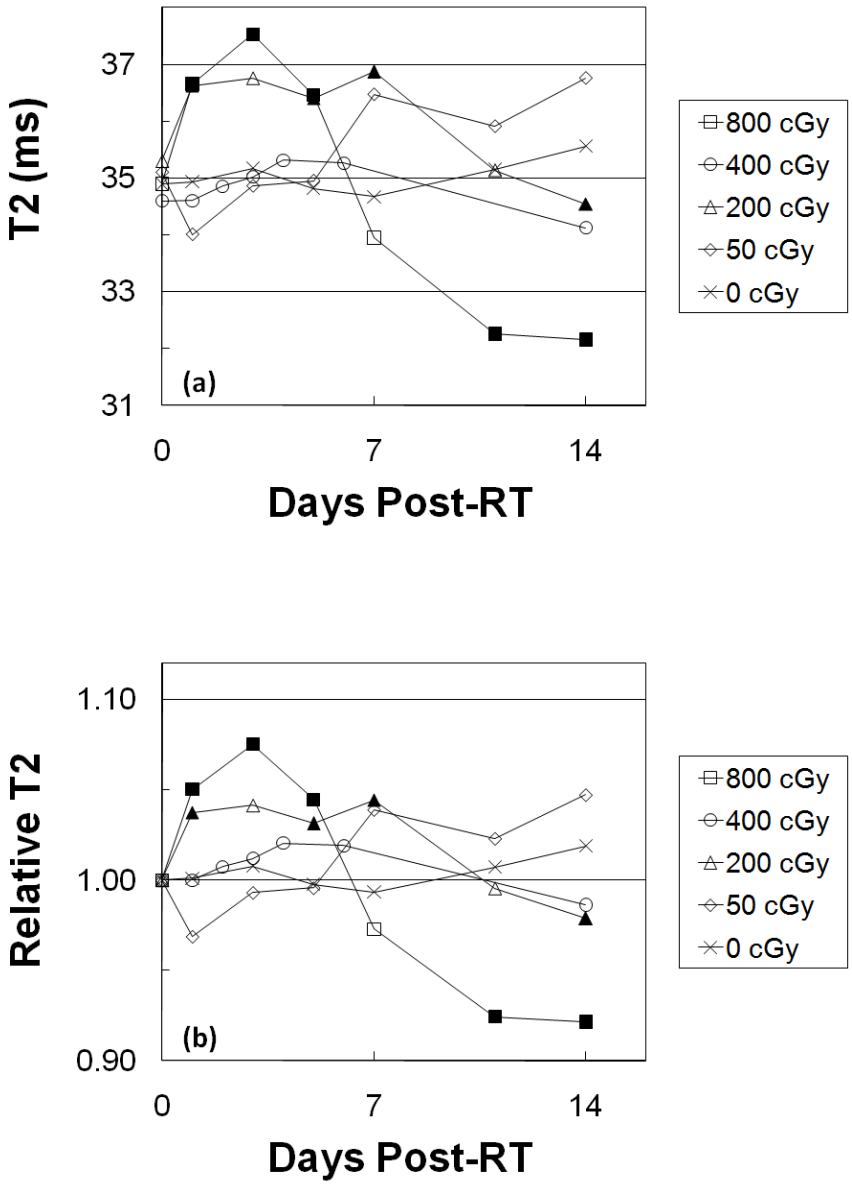

Figure 4.4. Time dependence of (a) average post-treatment tumour T2 and (b) average post-treatment T2 relative to the measured T2 pretreatment for five dose groups. Solid markers indicate data points that show statistically significant change according to a two-sample t-test ($p < 0.05$) relative to the untreated control group (×).

Fractional changes in ADC were larger than those in T2 for the highest dose level. ADC levels showed a statistically significant response ($p < 0.05$) at all dose levels. Figure 4.5 shows the changes in mean relative ADC after treatment. The 800 cGy group showed significant elevation of ADC at all time points after treatment. In this group there was a rapid increase in ADC seen 1 day post-treatment, which seemed to plateau at approximately 22% higher than the pre-treatment value by 7 days post-treatment. At 14 days post-treatment, the mean relative ADC had fallen slightly to approximately 16% greater than the pre-treatment value. The 400 cGy group showed statistically significant ADC elevation at 3 days post-treatment and all subsequent time points, as did the 200 cGy group. Although the group treated with 50 cGy appeared to have elevated ADC relative to the untreated control at all time points, only at the 7 day point did this difference become statistically significant. The highest mean relative ADC for the 800 cGy group occurred 7 days post-treatment, while for all other dose groups, the highest mean ADC was measured 14 days post-treatment.

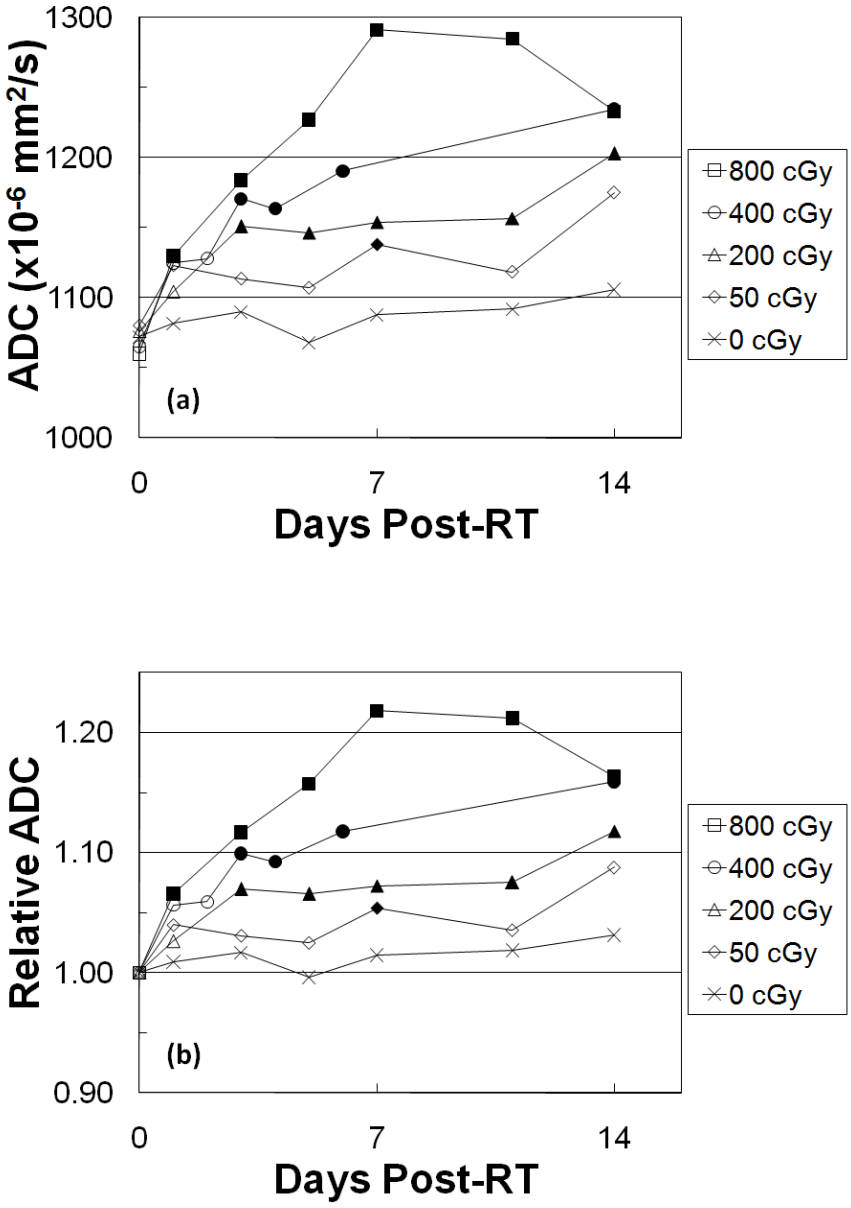

Figure 4.5. Time dependence of (a) average post-treatment tumour ADC and (b) average post-treatment ADC relative to the measured pretreatment ADC for five dose groups. Solid markers indicate data points that show statistically significant change according to a two-sample t-test ($p < 0.05$) relative to the untreated control group (×).

Normalized histograms were generated to investigate the nature of T2 and ADC response within tumours. Tumours from the control, 400 cGy, and 800 cGy groups whose individual ADC and T2 responses most closely resembled the mean responses from their group were identified. Figure 4.6 shows normalized T2 histograms from these tumours. Similarly, Figure 4.7 shows normalized ADC histograms from the same tumours.

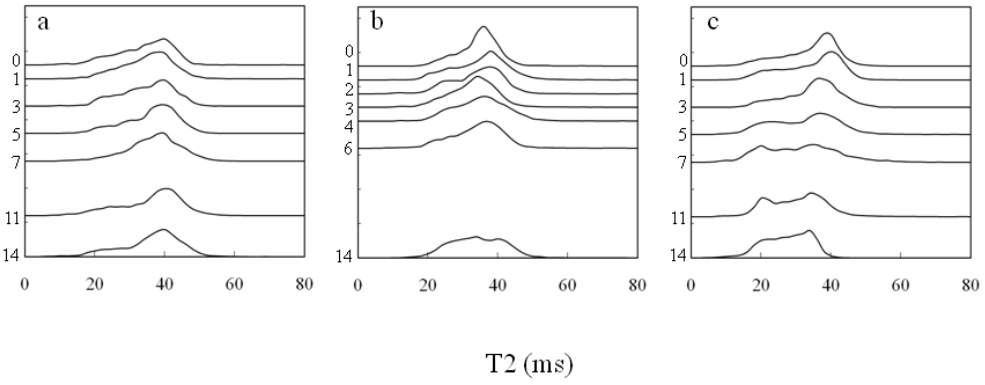

Figure 4.6. Representative T2 histograms for tumours receiving no radiation dose (a), 400 cGy delivered in a single fraction (b), and 800 cGy delivered in a single fraction (c). Each histogram is individually normalized. Histograms are vertically displaced proportional to the time in days relative to the final radiation treatment at which they were acquired.

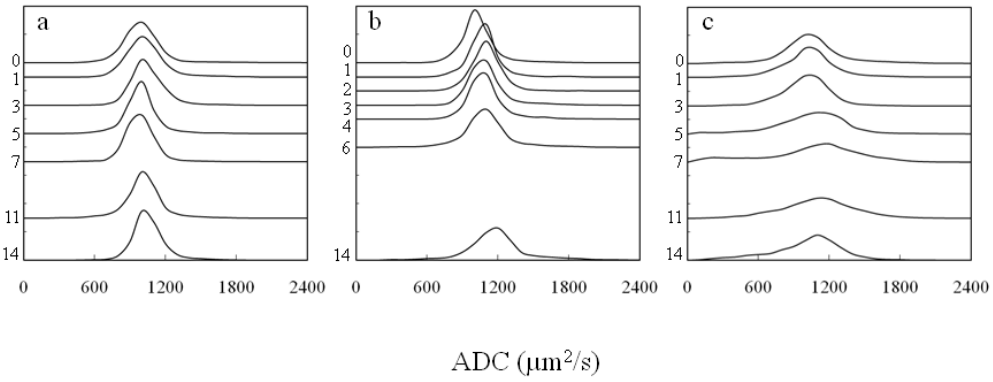

Figure 4.7. Representative ADC histograms for tumours receiving no radiation dose (a), 400 cGy delivered in a single fraction (b), and 800 cGy delivered in a single fraction (c). Each histogram is individually normalized. Histograms are vertically displaced proportional to the time in days relative to the final radiation treatment at which they were acquired.

There was a notable dose-dependence to the amplitude of ADC response at each time point. Figure 4.8 compares the dose dependence of relative ADC response when measured at 3 and 7 days post-treatment. At 7 days post-treatment, there was a nearly linear dose-dependence to the measured ADC response ($R^2 = 0.984$). At 3 days post-treatment, this dependence was not linear.

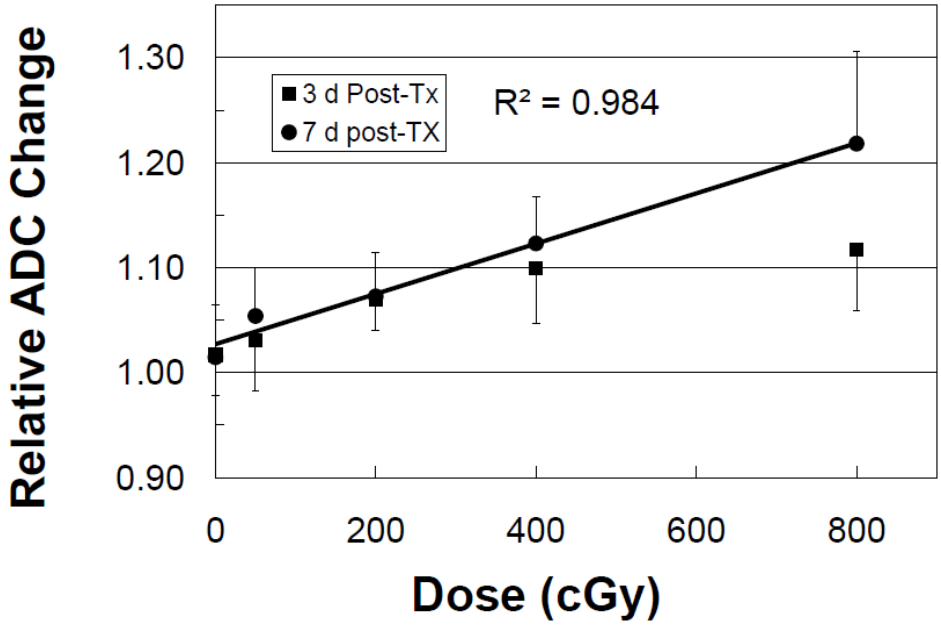

Figure 4.8. Dose-dependence of observed relative ADC response measured 3 and 7 days post-treatment. A linear best-fit line is shown for the data measured 7 days post-treatment.

Delivered radiation dose is negatively correlated with post-treatment growth rate and positively correlated with measured ADC response. Figure 4.9 shows the relationship between mean ADC response measured at seven days post-treatment and the estimated post-treatment linear growth rate. The negative correlation is strong (R^2 = 0.972) when comparing average values for each dose group, but this relationship is significantly weaker on the individual level.

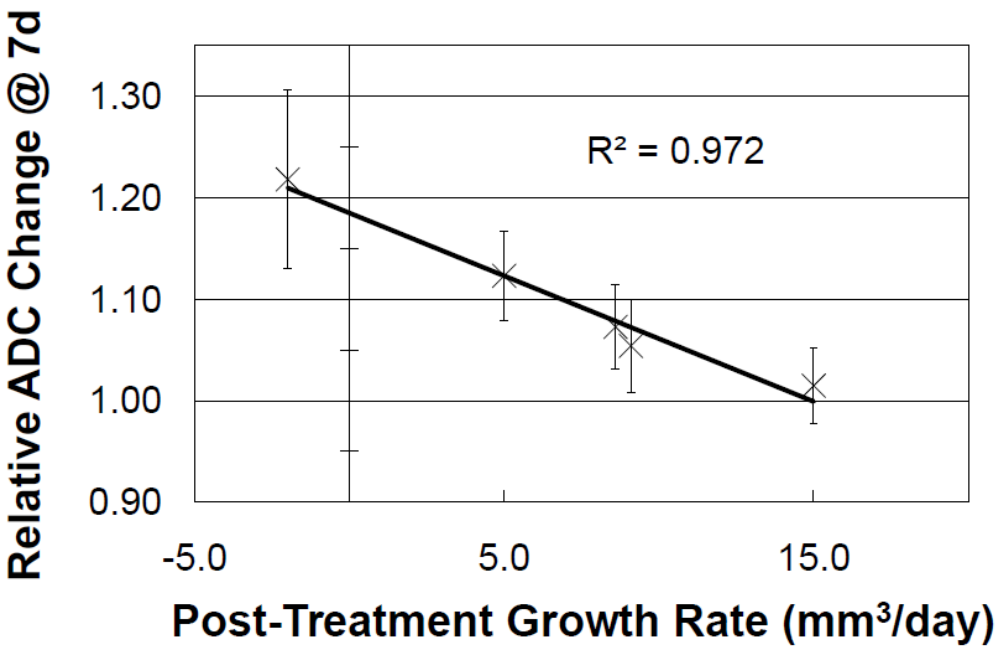

Figure 4.9. Correlation plot of average relative ADC change for each treatment group, as measured 3 days after treatment, versus post-treatment linear growth rate.

4.4 Discussion

Our results show that both ADC and T2 are sensitive to radiation therapy. Mean tumour ADC showed response at lower doses than did mean tumour T2, and showed larger relative changes at all doses compared to the untreated control. A greater relative change in ADC versus T2 has also been reported for tumour response to chemotherapy (9).

Descriptive statistics of observed T2 and ADC histograms are discussed in detail in chapter 5. The observed ADC histograms in Figure 4.7 are qualitatively similar to those reported by other groups (2,3,11).

An important feature of our data is the rate at which the mean tumour ADC responds to the radiation treatment. For all treatment groups, the tumours showed statistically significant ADC changes before mean tumour volume differed significantly from the control as determined by two-sample t-test. The tumours treated with 800 cGy showed differences in ADC 1 day after treatment, and differences in volume 2 days after treatment. Tumours treated with 400 cGy and 200 cGy showed significant ADC elevation 3 days after treatment, but neither group showed significant differences in mean tumour volume relative to untreated control group until 8 and 10 days after treatment, respectively. Tumours treated with 50 cGy had significantly elevated ADC at 7 days after treatment, but significant volume difference only at 10 days after treatment. In animal studies of tumour response to chemotherapies, ADC changes prior to changes in tumour volume have been repeatedly observed (9-12).

A limitation of this data set is that imaging time points are not identical for all groups. Chosen time points were adjusted after analysis of the initial treatment groups to better characterize the time-dependence of the response. Additional measurement of the 800 cGy response after publication of the initial data increased understanding of the subtleties of the response of this group, notably for the time period between 3 days and 14 days post-treatment, where three measurement time-points were added (5, 7, and 11 days post-treatment). This allowed better visualization of the peak ADC response measured at 7 days,

and the transition from elevated to depressed T2 between 5 and 7 days post-treatment.

A second important feature is the radiation dose-dependence of the induced ADC changes after radiation treatment. Our finding of a dose-dependent ADC response is consistent with the hypothesis that ADC increase after treatment reflects reduced cellularity and increased extracellular water content. Increasing radiation dose results in increasing cell kill, and as a consequence, higher tissue ADC is expected. *Zhao* (10) first reported a dose-dependent ADC response to chemotherapy, using two different doses of cyclophosphamide, which has since been confirmed using various chemotherapy agents (11,12).

Radiation dose-dependence is an important result because it suggests that ADC response is in some manner representative of the biological impact of radiation therapy on the tumour. There are recently published examples of studies attempting to show that early changes in ADC differ between responding and non-responding cancers (3,11,17,23).

Early, accurate evaluation of tumour response to therapy would help clinicians to make informed appraisals regarding prescribed treatments and to make changes to treatment plans based on the efficacy of the early stages of treatment, resulting in potentially better clinical outcomes.

References

1. Larocque MP, Syme A, Yahya A, Wachowicz K, Allalunis-Turner J, Fallone BG. Temporal and dose dependence of T2 and ADC at 9.4 T in a mouse model following single fraction radiation therapy. *Med Phys.* 2009: p. 2948-2954.

2. Ross BD, Moffat BA, Lawrence TS, Mukherji SK, Gebarski SS, Quint DJ, et al. Evaluation of cancer therapy using diffusion magnetic resonance imaging. *Mol Cancer Ther.* 2003: p. 581-586.

3. Hamstra DA, Rehemtulla A, Ross BD. Diffusion magnetic resonance imaging: a biomarker for treatment response in oncology. *J Clin Oncol.* 2007: p. 4104-4109.

4. Henning EC, Azuma C, Sotak CH, Helmer KG. Multispectral quantification of tissue types in a RIF-1 tumor model with histological validation. Part I. *Mag Reson Med.* 2007: p. 501-512.

5. Yezhelyev MV, Gao X, Xing Y, Al-Hajj A, Nie S, O'Regan RM. Emerging use of nanoparticles in diagnosis and treatment of breast cancer. *Lancet Oncol.* 2006: p. 657-667.

6. Zhao M, Beauregard DA, Loizou L, Davletov B, Brindle KM. Non-invasive detection of apoptosis using magnetic resonance imaging and a targeted

contrast agent. *Nature Med.* 2001: p. 1241-1244.

7. Gillies R, Morse D. In vivo magnetic resonance spectroscopy in cancer. *Annu Rev Biomed Eng.* 2005: p. 287-326.

8. Sun Y, Mulkern RV, Schmidt K, Doshi S, Albert MS, Schmidt NO, et al. Quantification of water diffusion and relaxation times of human U87 tumors in a mouse model. *NMR in Biomed.* 2004: p. 399-404.

9. Chenevert TL, McKeever PE, Ross BD. Monitoring early response of experimental brain tumors to therapy using diffusion magnetic resonance imaging. *Clin Cancer Res.* 1997: p. 1457-1466.

10. Zhao M, Pipe JG, Bonnett J, Evelhoch JL. Early detection of treatment response by diffusion-weighted 1H-NMR spectroscopy in a murine tumour in vivo. *Br J Cancer.* 1996: p. 61-65.

11. Chenevert TL, Stegman LD, Taylor JMG, Robertson PL, Greenberg HS, Rehemtulla A, et al. Diffusion magnetic resonance imaging: an early surrogate marker of theapeutic efficacy in brain tumors. *J Natl Cancer Inst.* 2000: p. 2029-2036.

12. Jennings D, Hatton BN, Guo J, Galons JP, Trouard TP, Raghunand N, et al. Early response of prostate carcinoma xenografts to docetaxel chemotherapy

monitored with diffusion MRI. *Neoplasia.* 2002: p. 255-262.

13. McConville P, Hambardzumyan D, Moody JB, Leopold WR, Kreger AR, Woolliscroft MJ, et al. Magnetic resonance imaging determination of tumor grade and early response to temozolomide in a genetically engineered mouse model of glioma. *Clin Cancer Res.* 2007: p. 2897-2904.

14. Roth Y, Tichler T, Kostenich G, Ruiz-Cabello J, Maier SE, Cohen JS, et al. High-b-value diffusion-weighted MR imaging for pretreatment prediction and early monitoring of tumor response to therapy in mice. *Radiology.* 2004: p. 685-692.

15. Stegman LD, Rehemtulla A, Hamstra DA, Rice DJ, Jonas SJ, Stout KL, et al. Diffusion MRI detects early events in the response of a glioma model to the yeast cytosine deaminase gene therapy strategy. *Gene Therapy.* 2000: p. 1005-1010.

16. Schepkin VD, Chenevert TL, Kuszpit K, Lee KC, Meyer CR, Johnson TD, et al. Sodium and proton diffusion MRI as biomarkers for early therapeutic response in subcutaneous tumors. *Mag Res Imaging.* 2006: p. 273-278.

17. Moffat BA, Chenevert TL, Lawrence TS, Meyer CR, Johnson TD, Dong Q, et al. Functional diffusion map: a noninvasive MRI biomarker for early stratification of clinical brain tumor response. *Proc Natl Acad Sci USA.* 2005: p. 5524-5529.

18. Mardor Y, Pfeffer R, Spiegelmann R, Roth T, Maier SE, Nissim O, et al. Early detection of response to radiation therapy in patients with brain malignancies using conventional and high b-value diffusion-weighted magnetic resonance imaging. *J Clin Oncol.* 2003: p. 1094-1100.

19. Lee KC, Moffat BA, Schott AF, Layman R, Ellingworth S, Juliar R, et al. Prospective early response imaging biomarker for neoadjuvant breast cancer chemotherapy. *Clin Cancer Res.* 2007: p. 443-450.

20. Hamstra DA, Galban CJ, Meyer CR, Johnson TD, Sundgren PC, Tsien C, et al. Functional diffusion map as an early imaging biomarker for high-grade glioma: correlation with conventional radiologic response and overall survival. *J Clin Oncol.* 2008: p. 3387-3394.

21. Henning EC, Azuma C, Sotak CH, Helmer KG. Multispectral tissue characterization in a RIF-1 tumor model: monitoring the ADC and T2 responses to single-dose radiotherapy. Part II. *Mag Reson Med.* 2007: p. 513-519.

22. Franko A, Parliament M, Allalunis-Turner J, Wolokoff B. Variable presence of hypoxia in M006 human glioma spheroids and in spheroids and xenografts of clonally derived sublines. *Br J Cancer.* 1998: p. 1261-1268.

23. Tomura N, Narita K, Izumi J, Suzuki A, Anbai A, Otani T, et al. Diffusion changes in a tumor and peritumoral tissue after stereotactic irradiation for brain tumors: possible prediction of treatment response. *J Comput Assist Tomogr.* 2006: p. 496-500.

Chapter 5: ADC and T2 Response after Fractionated Radiotherapy

The previous chapter investigated the response of tumours to single fraction radiotherapy. In the clinic, however, the vast majority of radiation therapy involves fractionated delivery in which the total dose is delivered over a large number of treatments. The work presented in this chapter expands on the previous results by investigating the temporal evolution of ADC and T2 in human glioma xenografts after radiotherapy using a variety of fractionation schemes. Like those of the previous chapter, the experimental findings discussed in this chapter have also been published (1).

5.1 Introduction

Quantitative measurement of multiple tissue parameters is being investigated for potential use as a bio-marker for treatment response including T2 and ADC. A limitation of many clinical studies is that the number of imaging sessions is small due to the required resources and demands on patient time. These factors make it difficult to study the time dependence of treatment response in humans with reasonable temporal resolution. The use of an animal model allows greater flexibility for serial MRI measurements, as well as allowing a more direct study of treatment response by controlling factors which might influence tumour sensitivity such as tumour type, tumour cell line, tumour location, and tumour volume at the start of treatment.

We recently published a study on the impact of dose on the temporal evolution of T2 and ADC in a mouse model after a single dose of radiation, where doses up to 800 cGy were administered (2). A limitation of the study, and other studies investigating T2 and ADC response to radiation, is that the therapeutic intervention was delivered in a single dose. Although there have been advances in single-dose external-beam radiation treatment, known as radiosurgery (3), the most common method of external-beam delivery is a fractionated treatment, where the total prescribed dose is divided into as many as 30 or more fractions, typically delivered on a daily basis.

Better understanding the response of ADC and T2 after fractionated therapy is important because a fractionated therapy more closely resembles what a patient would receive in the clinic. In this work we monitor a mouse model of cancer before, during, and after fractionated radiotherapy and compare the effects of multiple fractionation schemes on overall ADC and T2 response.

5.2 Methods

The experimental details closely follow those outlined in the previous chapter and discussed in detail in chapter 3.

NIH-iii nude mice of approximately 6 weeks of age were obtained from Charles River Laboratories (Wilmington, MA, USA). Human glioblastoma multiforme (GBM) cells of the line M006xLo (4) were used to initiate tumour xenografts as described in section 3.1.

Tumours were measured using digital caliper and tumour volumes were estimated assuming the tumour shape to be ellipsoid. Tumours were allowed to grow until they reached a volume of approximately 150 mm^3, at which point the tumours were slated for treatment using one of five fractionation schemes, with a total of six mice being treated per fractionation scheme. Data for an untreated control group had previously been obtained (2). All treatments were delivered

using 200 kVp x-rays from a Pantak orthovoltage unit (Pantak, Inc., Brantford, CT, USA) according to the procedure described in section 3.6.

All five fractionation schemes delivered the same total dose of 800 cGy, which is the highest dose delivered in our previous study (2). This dose was delivered in either one (n = 6 mice), two (n = 12), or three (n = 12) fractions. In the fractionated deliveries, the time between treatments was either 24 or 72 hours The 72 hour fraction spacing aligned with the length of time over which we observed significant increases in tumour ADC and T2, and the 24 hour fraction spacing is consistent with typical clinical fraction spacings.

Mice underwent MRI pretreatment and at multiple time points after treatment according to the imaging procedure described in detail in sections 3.3 and 3.4. All mice were imaged immediately preceding the delivery of each fraction of radiation. Mice treated with a single fraction of 800 cGy were imaged at 1, 3, 5, 7, 11, and 14 days after treatment. These mice are distinct from those initially treated with a single fraction of 800 cGy and whose responses were initially published (2). This dose group has been repeated with better timing of imaging sessions, as this will be an important group for comparison purposes, and their response is included in this chapter as well as in chapter 4. Mice that were given multiple treatments spaced 24 hours apart were imaged 24 hours after each fraction, with imaging sessions always preceding radiation delivery, as well as 1, 3, 5, 7, 11, and 14 days after the final fraction. Mice given fractions

spaced 72 hours apart were imaged at 24 and 72 hours after each fraction, with the imaging session at 72 hours immediately preceding radiation delivery, as well as 1, 3, 7, 11, and 14 days after the final fraction of radiation. The timings of imaging sessions and treatments are summarized in Figure 5.1.

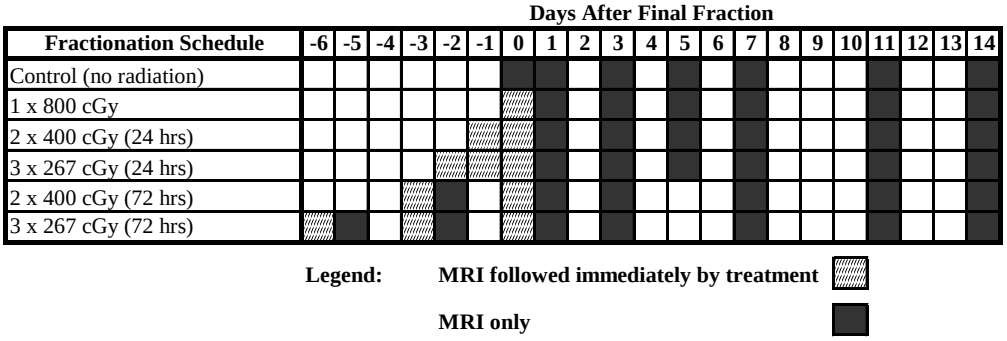

Figure 5.1. Summary of treatment and imaging schedule for all treatment groups as a function of days after the final fraction of radiotherapy. Hashed squares indicate days where MR images were acquired, followed by delivery of a radiotherapy fraction. Black squares indicate days where MR images were acquired but no treatment was delivered.

For all mice two series of images were acquired. The first series collected diffusion-weighted spin-echo (DW-SE) images with both low and high b-value. DW-SE images were acquired with the diffusion-sensitizing gradient applied along the three orthogonal axes of the magnet coordinate system. The second series of images were spin-echo (SE) images with increasing echo times (TEs) (increasing T2-weighting).

Image analysis was performed using code written in the MATLAB programming language (The MathWorks, Natwick, MA, USA) as described in section 3.5. ADC and T2 maps were generating by performing a pixel-by-pixel analysis. ADC maps were produced by fitting DW-SE data with a monoexponential decay of the form

$$S(b) = S(0) \cdot \exp(-b \cdot D), \tag{5.1}$$

where S(b) is the signal in a given pixel as a function of b-value, S(0) is the signal intensity expected in the pixel for an image with no diffusion-weighting (b = 0), and D is the diffusion coefficient measured in the voxel, along the axis of the applied diffusion sensitizing gradient. The ADC is then the linear average of the measured diffusion gradient in three orthogonal directions.

T2 maps were produced by fitting the T2-weighted data with a monoexponential decay of the form

$$S(TE) = S(0) \cdot \exp(-TE/T2), \tag{5.2}$$

where S(TE) is the signal in a given pixel as a function of TE, S(0) is the signal expected in the voxel for an image with TE = 0.

Contours were drawn on the SE images with shortest TE to define the volume of each tumour. The MATLAB program then extracted ADC and T2 values for all voxels within the tumour so that the characteristics of the distributions could be analyzed.

5.3 Results

Mean tumour T2 and ADC were calculated for each tumour for every MRI session. The values of T2 and ADC measured for individual tumours pretreatment were used to normalize all subsequent measurements. The average pretreatment values of mean tumour T2 and ADC for each treatment group are shown in Table 5.1.

Table 5.1. Pretreatment and post-treatment T2 and ADC data for each treatment group. All treatment groups received a total of 800 cGy. The highest fractional increase in ADC and T2, and lowest measured relative T2 is given for each treatment group, as well as the estimated number of days post-treatment at which mean tumour T2 transitions from above to below the pretreatment value and the minimum measured relative T2.

		Pretreatment		Post-treatment			
Fractions	Fraction Spacing (hours)	T2 (ms)	ADC ($\mu m^2/s$)	Max Relative ADC ± SD	Max Relative T2 ± SD	Min Relative T2 ± SD	Time T2 Crosses Baseline (Days after Last Fraction)
0 (Control)	---	34.9	1072	---	---	---	---
1	---	34.1	1065	1.22 ± 0.06	1.05 ± 0.03	0.92 ± 0.02	6.2
2	24	34.4	1071	1.18 ± 0.04	1.04 ± 0.03	0.93 ± 0.03	7.3
3	24	35.6	1066	1.17 ± 0.05	1.04 ± 0.03	0.98 ± 0.04	6.6
2	72	35.6	1085	1.24 ± 0.06	1.07 ± 0.03	0.91 ± 0.02	7.0
3	72	35.8	1063	1.21 ± 0.06	1.05 ± 0.04	0.89 ± 0.03	3.6

All treated groups showed increases in mean tumour ADC after the start of treatment. Relative ADC response for each group is shown in Figure 5.2, as a

function of time after the delivery of the last fraction. Plotting as a function of time after last fraction rather than time after first fraction allows a more clear comparison of the behavior of ADC response at the height of response. It is important to note that the control group was matched to the treated groups by starting MRI observation of the control tumours once they had reached the same predetermined size at which treatment was started for the treated groups (150 mm^3). In Figure 5.2 the control group is aligned with the start of treatment for the single fraction case, for the purpose of clarity. In the fractionated cases, mean tumour ADC increases over the course of treatment, peaks post-treatment and is returning towards baseline by the last time point. For each treated group, the highest ADC was measured during the MRI session 7 days after the last fraction of radiation was delivered. The highest measured ADC relative to pretreatment value is listed in Table 5.1.

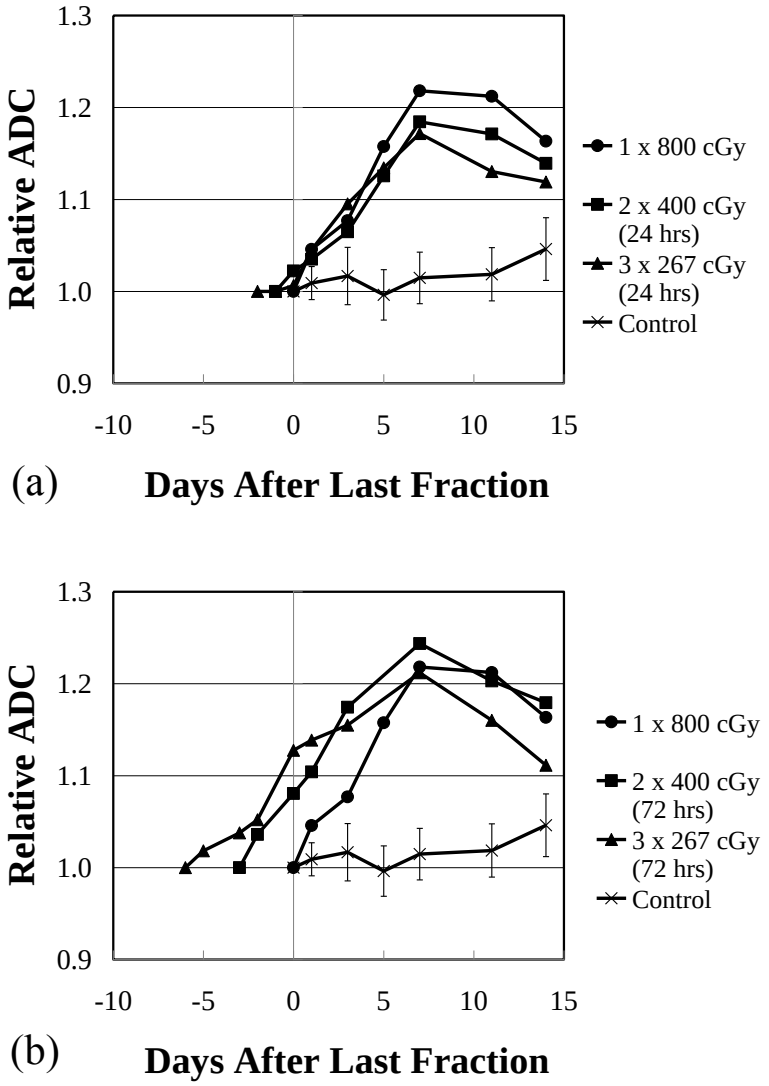

Figure 5.2. Mean relative ADC response for groups treated with either 2 or 3 fractions of radiotherapy, separated by either (a) 24 hours or (b) 72 hours plotted as a function of time after the last fraction of radiation. Single-fraction and untreated control data are also shown in both (a) and (b). The first plotted point for each curve is the data acquired from imaging immediately preceding the first fraction of radiation. For the purpose of clarity, error bars are only included for the control group, however these are generally representative of the error bars associated with all data presented in this figure. Maximum measured relative ADC ± SD for all treated groups is listed in Table 5.1.

Figure 5.3 is a plot of relative T2 response of the treated groups as a function of time after the last fraction of treatment. In all treated groups there is an increase in mean tumour T2 after treatment begins, followed by a transition to mean tumour T2 values below the baseline and the control at later time points. The maximum and minimum relative change in T2 for each group is listed in Table 5.1.

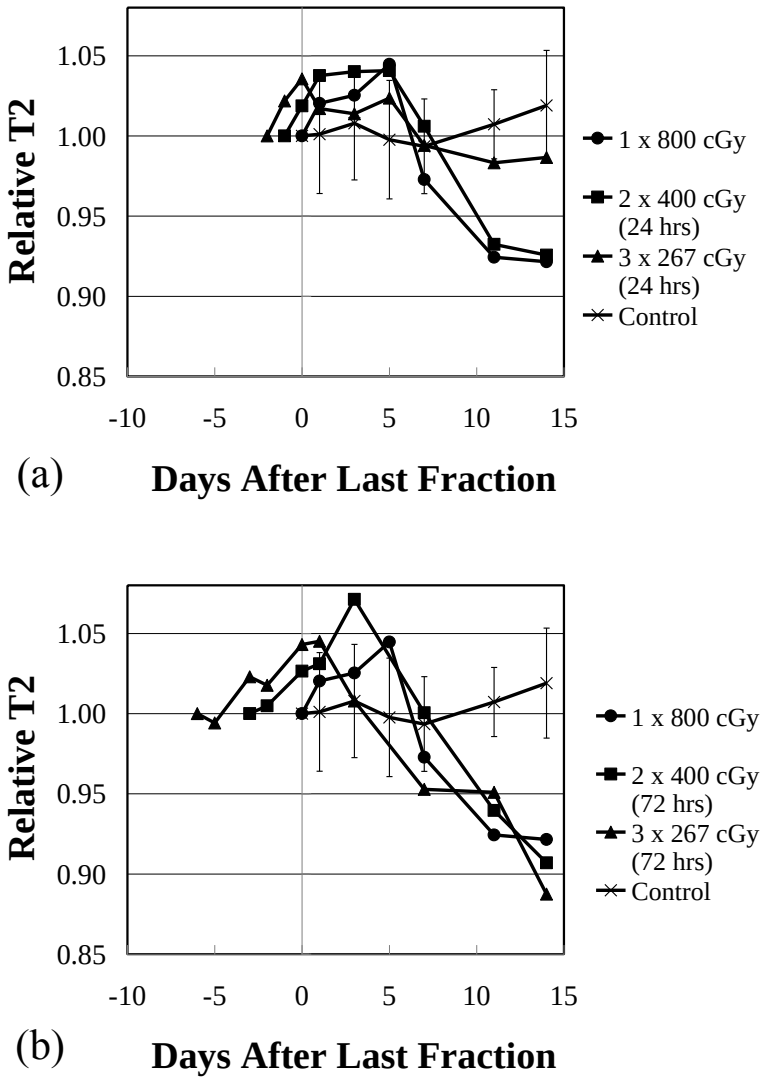

Figure 5.3. Mean relative T2 response for groups treated with either 2 or 3 fractions of radiotherapy, separated by either (a) 24 hours or (b) 72 hours plotted as a function of time after the last fraction of radiation. Single-fraction and untreated control data are shown in both (a) and (b). The first plotted point for each curve is the data acquired from imaging immediately preceding the first fraction of radiation. For the purpose of clarity, error bars are only included for the control group, however these are generally representative of the error bars associated with all data presented in this figure. Maximum and minimum measured relative T2 ± SD for all treated groups is listed in Table 5.1.

The noticeable difference in T2 transition time in the three fraction, 72 hour fraction separation group is due to the presence of two unusually responding tumours within the sample of six. Figure 5.4 is a plot comparing the relative T2 response for this group with all tumours included, or one or both of the outliers are excluded. One outlier (#1) had a significantly lower pretreatment T2 than the other tumours (28.6 ms; group average = 35.8 ms). This tumour had a minimal positive change in T2 after the first fraction, and had transitioned to permanent state of depressed T2 value relative to pretreatment value before the final fraction was administered. A second outlier (#2) had a normal pretreatment average T2 (35.3 ms; group average = 35.8 ms), but had a depressed T2 values at all measured time points after the administration of the first fraction.

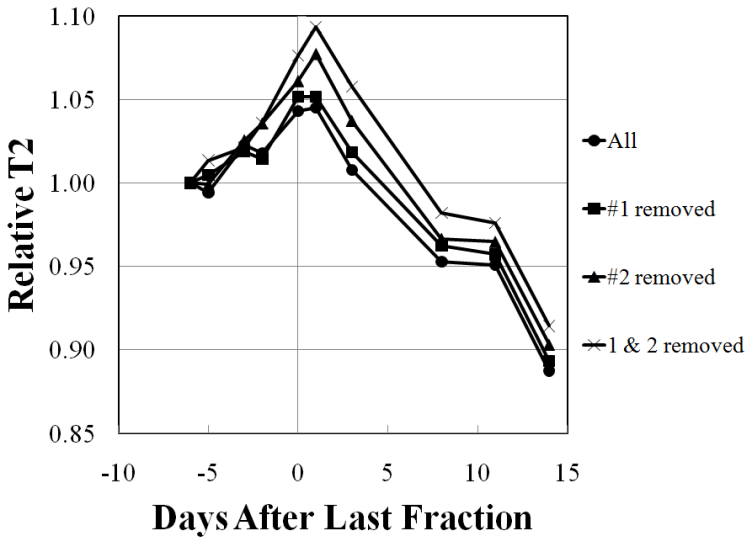

Figure 5.4. Mean relative T2 plotted as a function of time after last fraction for treatment group receiving three fractions of 267 cGy separated by 72 hours. The relative T2 response is plotted including all mice in the treatment group (n = 6), with outlier #1 removed (n = 5) or with outlier #2 removed (n = 5), or with both outliers removed (n = 4). There is pronounced increase in peak relative T2 response and delay in transition between elevated and depressed relative T2 with removal of the two outliers.

While removal of two tumours out of six greatly reduces the statistical power of the sample, when either of the tumours is removed, there is an increase in peak relative T2 response and a delay in the T2 transition time. When both of the outliers are removed, the T2 transition time shifts from 3.6 to 6.8 days after the last fraction, which is very similar to the T2 transition time observed for the other treatment groups. Group statistics with either one of or both of the two outliers removed from the sample are summarized in Table 5.2.

Table 5.2. Analysis of impact of removing outliers from three fraction, 72 hour fraction-spacing tumour group. Mean pretreatment T2 and time for T2 to cross baseline (based on linear interpolation) after removal of outlier #1, outlier #2, or both.

Outliers removed	# of tumours	Pretreatment T2 (ms)	Time T2 crosses baseline (days after last fraction)
none	6	35.8	3.6
only #1	5	37.2	4.6
only #2	5	35.9	5.6
#1 + #2	4	37.7	6.8

Normalized histograms of ADC and T2 distributions were prepared for tumours at all measured time points. Tumours from each treatment group whose individual ADC and T2 responses most closely resembled the mean responses from their group were identified. Figure 5.5 shows ADC distributions for these tumours from the untreated control group, the group treated with a single fraction, and from the fractionated group where the total dose was delivered over the longest period of time (3 fractions separated by 72 hours). Figure 5.6 similarly shows T2 distributions taken from the same tumours at the same time points.

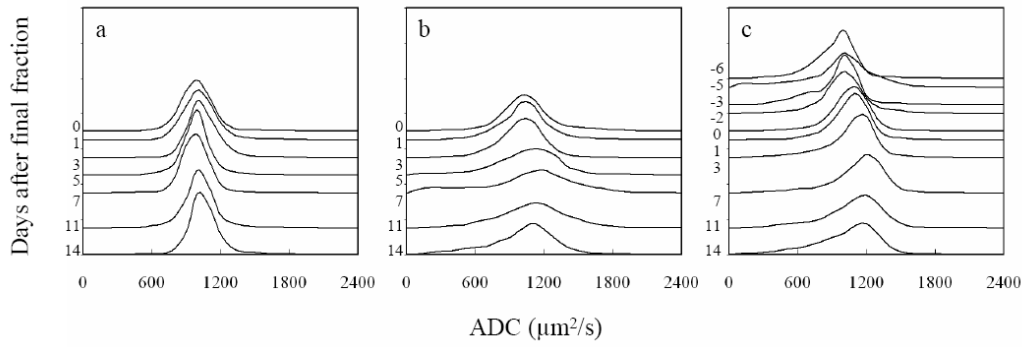

Figure 5.5. Representative ADC histograms for tumours receiving no radiation dose (a), 800 cGy delivered in a single fraction (b), and 800 cGy delivered over three fractions separated by 72 hours each (c). Each histogram is individually normalized. Histograms are vertically displaced proportional to the time in days relative to the final radiation treatment at which they were acquired. The histograms in (a) and (b) were previously shown in chapter 4, but are shown again here for the purpose of comparison.

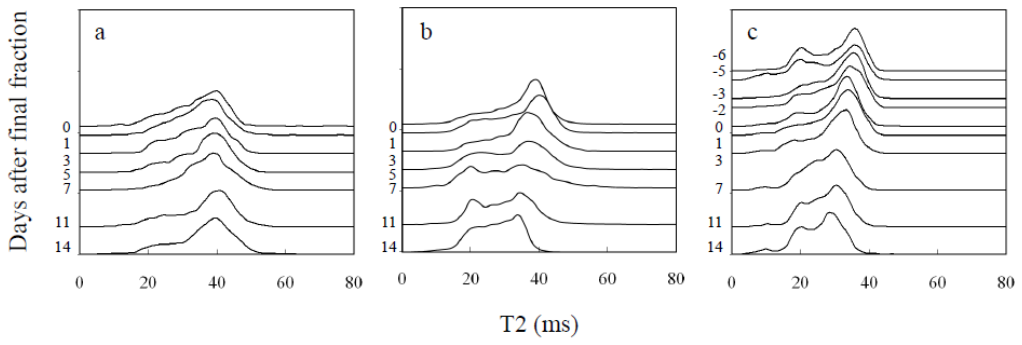

Figure 5.6. Representative T2 histograms for tumours receiving no radiation dose (a), 800 cGy delivered in a single fraction (b), and 800 cGy delivered over three fractions separated by 72 hours each (c). Each histogram is individually normalized. Histograms are vertically displaced proportional to the time in days relative to the final radiation treatment at which they were acquired. The histograms in (a) and (b) were previously shown in chapter 4, but are shown again here for the purpose of comparison.

Descriptive statistics were calculated for the ADC distributions of each tumour at every measurement time point using the data analysis package in Microsoft Excel (Version 11.8117.8107, Microscoft Inc., Redmond, WA, USA), in order to identify trends in the behavior of the distributions after treatment. In particular, the mean values of the variance, skewness and kurtosis of each treatment group were investigated. The mean variance in each treatment group was approximately constant with time. The mean skewness of ADC distributions for each treatment group ranged from 0.06 to 0.90 before treatment and ranged from -0.52 to 0.37 two weeks after the final fraction. The mean skewness in every treatment group decreased at later time points, but the distributions of calculated skewness values were too wide to assign significance to these trends.

Mean kurtosis for each treatment group at all measured time points is shown in Figure 5.7. The kurtosis of the distributions demonstrated some temporal correlation with ADC. A qualitative comparison between Figure 5.7 and Figure 5.2 indicates that kurtosis decreases as ADC increases. A more quantitative evaluation revealed that the correlation was relatively weak with an R^2 value of 0.36.

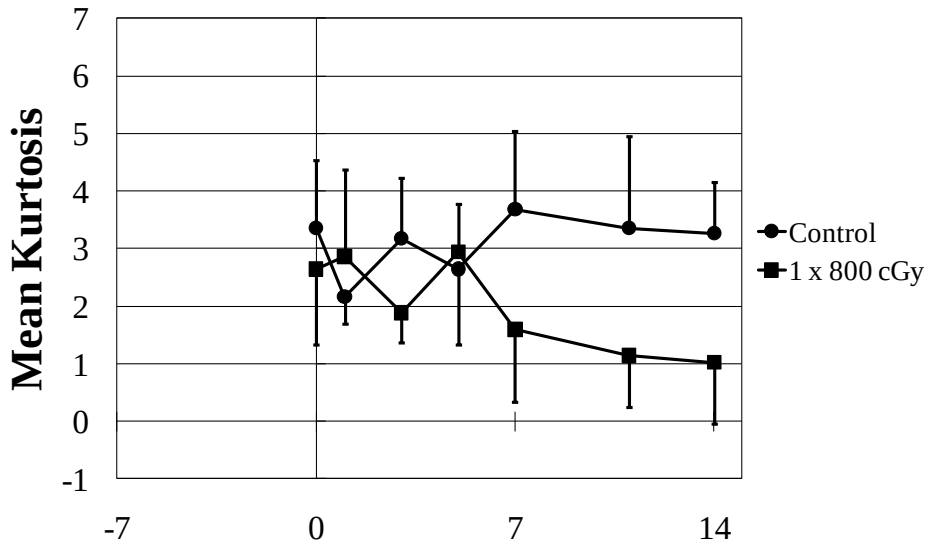

a)

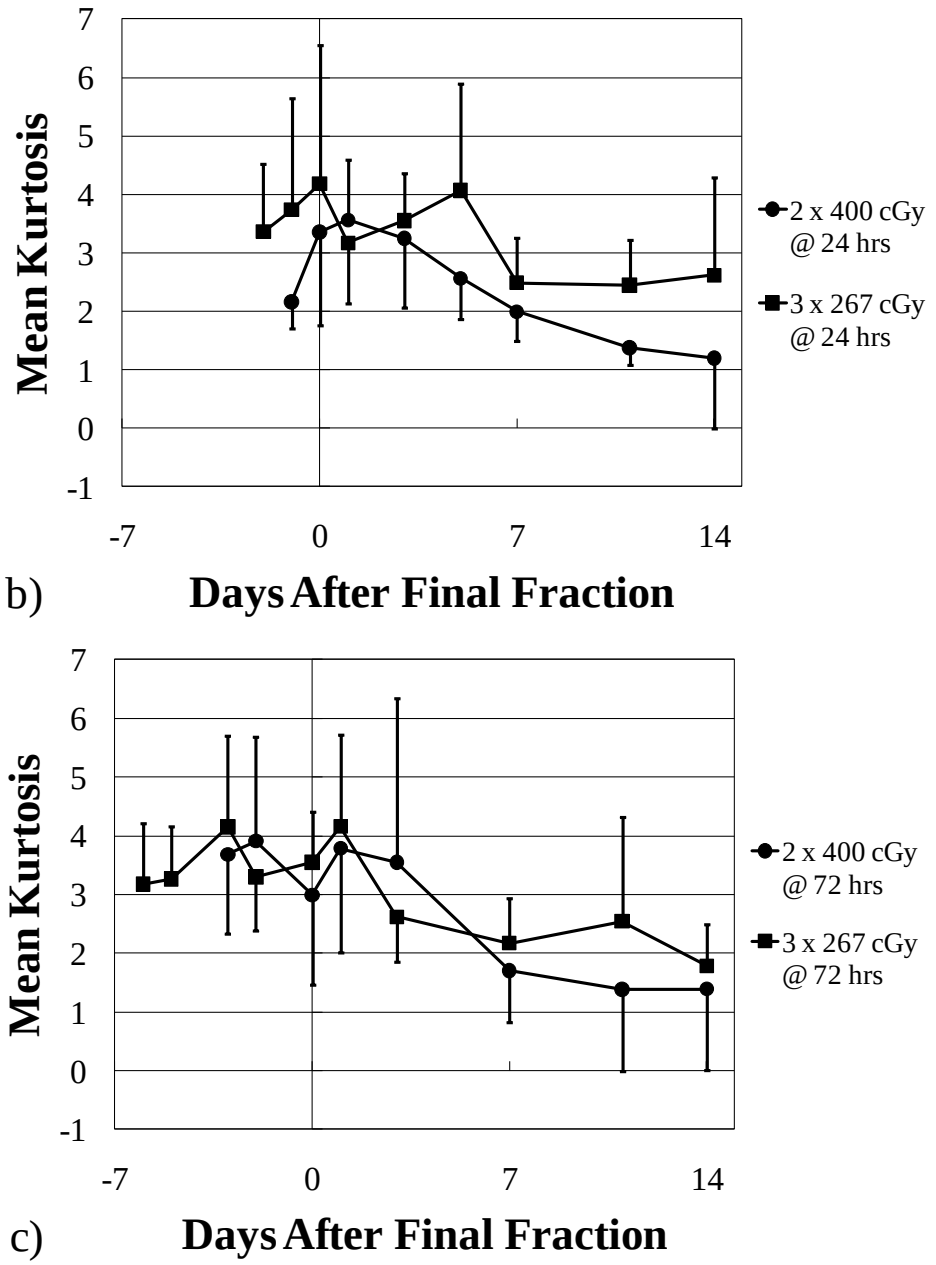

Figure 5.7. Mean kurtosis of ADC distributions for untreated control and single fraction groups (a), groups with fraction spacings of 24 hours (b), and groups with fraction spacings of 72 hours (c). Error bars indicate one standard deviation above or below the mean.

Analysis of the statistics describing the T2 distributions revealed no trends in the time-dependence of variance, skewness or kurtosis. The temporal

evolution of the T2 histograms is more complicated than that of the ADC histograms. In general, the T2 histograms featured a prominent peak at higher T2 values and a tail extending to lower T2 values. In some cases, the frequency of pixels with lower T2 values was such that the distributions appeared nearly bimodal. Although there were cases of clear high or low T2 features within individual tumours, in general we did not find structured patterns in the spatial distributions of T2 values within tumours.

5.4 Discussion

For all treatment groups, ADC increased 24 hours after the start of treatment. ADC continued to rise between fractions, and for all groups the highest ADC measured was 7 days after treatment had finished. Elevation in ADC after radiation treatment is consistent with our previous observations (2), and those of others (5,6) and is consistent with the hypothesis that ADC increases in response to reduced cellularity and increased extracellular water content, which is assumed to occur in response to radiation treatment.

As previously mentioned, elevation of ADC after radiation treatment has also been reported in multiple clinical studies. Direct comparison between animal models and the responses seen at these sites is difficult. In particular, the total radiation dose delivered in this study is significantly less than what is used in the clinic where doses in excess of 7000 cGy may be delivered (7). In this case, the total dose is limited by the impracticality of delivering as many as 30

fractions of radiation in a mouse model, which would require excessive anesthesia of the animals. We have chosen instead to fix the fraction sizes and spacings closer to a clinical model, where 200 cGy fractions separated by 24 hours could be expected.

The behavior of ADC in the treated groups illustrated in Figure 5.5 is similar to that which we have previously observed (2). There appears to be a global shift in the observed distributions without significant changes in the variance of these distributions. This histogram shift appears qualitatively similar to behavior reported in other animal models treated with chemotherapy agents (8,9). The positive pretreatment skewness of each treatment group indicates that on average, these distributions had a longer tail on the higher ADC side of the distribution. The histograms became more symmetrical after treatment. All treatment groups had positive kurtosis at all measurement points, indicating the distributions were more sharply peaked than a normal distribution. Decreases in kurtosis post-treatment suggest the distributions, on average, become closer to normal at later time points, although this trend is obscured by relatively large distributions in calculated kurtosis values within individual treatment groups. Any biological significance of these behaviors is not clear from the data obtained in this study.

Observed increases in T2 followed by a transition to decreased T2 are also consistent with our previous reporting (2) at this dose level. For each case,

the transition to decreased T2 occurred between 3.6 and 7.3 days after the final fraction of radiation. This transition occurred at a time either before or very close to the time at which the highest value of ADC was observed. At later measurement points, while T2 is still decreasing, values of ADC have reached their maximum and are returning back towards baseline. The observation that extremes of T2 and ADC response are not temporally correlated suggests that not all factors contributing to the observed response are common to both parameters. There have been studies into the pathophysiological nature of parameter response (5), particularly that of ADC (9,10), but further investigation into the sources of the observed responses is warranted. Henning *et al* (5) noted higher T2 in necrotic areas that were generally acellular, with lower T2 in necrotic regions that contained a sparse cellular population combined with the presence of red blood cells (RBCs), noting that RBCs with high deoxyhemoglobin/methemoglobin are paramagnetic and may shorten local T2. Increases in ADC have consistently been shown to correlate with decreases in cellular density and increased extracellular volume. Relevant histological data regarding the responses of ADC and T2 for this tumour line are reported in chapter 7.

It is unclear what T2 behavior to expect during treatment if dose and fractionation were to be extended beyond what is examined here to more clinically relevant values. There appear to be underlying pathophysiological

factors that drive both increases and decreases in T2. This may result in a less clear response observable by quantitative T2 measurements during treatment with higher doses and a greater number of fractions. ADC response is of greater magnitude and is unidirectional over the period of time studied here, though the trend in all groups indicates a return toward baseline values after a peak is reached 7 days after the end of treatment. Although we previously observed a strong dose dependence in the ADC response to single fraction radiotherapy (2), it is interesting to note that in this limited study, dose per fraction does not have a significant effect on peak ADC enhancement. This could suggest that the cumulative amount of radiobiological damage plays an important role in this parameter's response.

The absolute ADC and T2 values reported in this study are specific to this tumour model, and we have reported both inter- and intra-tumour variations in these values for this model. Additionally, ADC and T2 values may be dependent on measurement technique, therefore this type of analysis may be most useful when using pretreatment measurements to detect relative changes in tumour ADC and T2.

References

1. Larocque MP, Syme A, Yahya A, Wachowicz K, Allalunis-Turner J, Fallone BG. Monitoring T2 and ADC at 9.4 T following fractionated external beam

radiation therapy in a mouse model. *Phys. Med. Biol.* 2010: p. 1381-1393.

2. Larocque MP, Syme A, Yahya A, Wachowicz K, Allalunis-Turner J, Fallone BG. Temporal and dose dependence of T2 and ADC at 9.4 T in a mouse model following single fraction radiation therapy. *Med Phys.* 2009: p. 2948-2954.

3. Andrews DW, Bednarz G, Evans JJ, Downes B. A review of 3 current radiosurgery systems. *Surg Neurol.* 2006: p. 559-564.

4. Franko A, Parliament M, Allalunis-Turner J, Wolokoff B. Variable presence of hypoxia in M006 human glioma spheroids and in spheroids and xenografts of clonally derived sublines. *Br J Cancer.* 1998: p. 1261-1268.

5. Henning EC, Azuma C, Sotak CH, Helmer KG. Multispectral quantification of tissue types in a RIF-1 tumor model with histological validation. Part I. *Mag Reson Med.* 2007: p. 501-512.

6. Henning EC, Azuma C, Sotak CH, Helmer KG. Multispectral tissue characterization in a RIF-1 tumor model: monitoring the ADC and T2 responses to single-dose radiotherapy. Part II. *Mag Reson Med.* 2007: p. 513-519.

7. Kim S, Loevner L, Quon H, Sherman E, Weinstein G, Kilger A, et al. Diffusion-weighted magnetic resonance imaging for predicting and detecting early

response to chemoradiation therapy of squamous cell carcinomas of the head and neck. *Clin. Cancer Res.* 2009: p. 986-994.

8. Hamstra DA, Rehemtulla A, Ross BD. Diffusion magnetic resonance imaging: a biomarker for treatment response in oncology. *J Clin Oncol.* 2007: p. 4104-4109.

9. Chenevert TL, Stegman LD, Taylor JMG, Robertson PL, Greenberg HS, Rehemtulla A, et al. Diffusion magnetic resonance imaging: an early surrogate marker of theapeutic efficacy in brain tumors. *J Natl Cancer Inst.* 2000: p. 2029-2036.

10. Chenevert TL, McKeever PE, Ross BD. Monitoring early response of experimental brain tumors to therapy using diffusion magnetic resonance imaging. *Clin Cancer Res.* 1997: p. 1457-1466.

11. Mitchell DG, Burk DLJ, Vinitski S, Rifkin MD. The biophysical basis of tissue contrast in extracranial MR imaging. *Am. J. Roentgenol.* 1987: p. 831-837.

12. Sun Y, Mulkern RV, Schmidt K, Doshi S, Albert MS, Schmidt NO, et al. Quantification of water diffusion and relaxation times of human U87 tumors in a mouse model. *NMR in Biomed.* 2004: p. 399-404.

13. Ross BD, Moffat BA, Lawrence TS, Mukherji SK, Gebarski SS, Quint DJ, et al.

Evaluation of cancer therapy using diffusion magnetic resonance imaging. *Mol Cancer Ther.* 2003: p. 581-586.

14. Zhao M, Pipe JG, Bonnett J, Evelhoch JL. Early detection of treatment response by diffusion-weighted 1H-NMR spectroscopy in a murine tumour in vivo. *Br J Cancer.* 1996: p. 61-65.

15. Szafer A, Zhong J, Anderson AW, Gore JC. Diffusion-weighted imaging in tissues: theoretical models. *NMR in Biomed.* 1995: p. 289-296.

16. Jennings D, Hatton BN, Guo J, Galons JP, Trouard TP, Raghunand N, et al. Early response of prostate carcinoma xenografts to docetaxel chemotherapy monitored with diffusion MRI. *Neoplasia.* 2002: p. 255-262.

17. McConville P, Hambardzumyan D, Moody JB, Leopold WR, Kreger AR, Woolliscroft MJ, et al. Magnetic resonance imaging determination of tumor grade and early response to temozolomide in a genetically engineered mouse model of glioma. *Clin Cancer Res.* 2007: p. 2897-2904.

18. Roth Y, Tichler T, Kostenich G, Ruiz-Cabello J, Maier SE, Cohen JS, et al. High-b-value diffusion-weighted MR imaging for pretreatment prediction and early monitoring of tumor response to therapy in mice. *Radiology.* 2004: p. 685-692.

19. Stegman LD, Rehemtulla A, Hamstra DA, Rice DJ, Jonas SJ, Stout KL, et al. Diffusion MRI detects early events in the response of a glioma model to the yeast cytosine deaminase gene therapy strategy. *Gene Therapy.* 2000: p. 1005-1010.

20. Schepkin VD, Chenevert TL, Kuszpit K, Lee KC, Meyer CR, Johnson TD, et al. Sodium and proton diffusion MRI as biomarkers for early therapeutic response in subcutaneous tumors. *Mag Res Imaging.* 2006: p. 273-278.

21. Moffat BA, Chenevert TL, Lawrence TS, Meyer CR, Johnson TD, Dong Q, et al. Functional diffusion map: a noninvasive MRI biomarker for early stratification of clinical brain tumor response. *Proc Natl Acad Sci USA.* 2005: p. 5524-5529.

22. Mardor Y, Pfeffer R, Spiegelmann R, Roth T, Maier SE, Nissim O, et al. Early detection of response to radiation therapy in patients with brain malignancies using conventional and high b-value diffusion-weighted magnetic resonance imaging. *J Clin Oncol.* 2003: p. 1094-1100.

23. Hamstra DA, Galban CJ, Meyer CR, Johnson TD, Sundgren PC, Tsien C, et al. Functional diffusion map as an early imaging biomarker for high-grade glioma: correlation with conventional radiologic response and overall survival. *J Clin Oncol.* 2008: p. 3387-3394.

24. Lee KC, Moffat BA, Schott AF, Layman R, Ellingworth S, Juliar R, et al.

Prospective early response imaging biomarker for neoadjuvant breast cancer chemotherapy. *Clin Cancer Res.* 2007: p. 443-450.

25. Goldman M, Boxerman JL, Rogg JM, Norén G. Utility of apparent diffusion coefficient in predicting the outcome of Gamma Knife-treated Brain metastases prior to changes in tumor volume: a preliminary study. *J. Neurosurg.* 2006: p. 175-182.

26. Harry VN, Semple SI, Gilbert FJ, Parkin DE. Diffusion-weighted magnetic resonance imaging in the early detection of response to chemoradiation in cervical cancer. *Gynecol. Oncol.* 2008: p. 213-220.

27. Eccles C, Haider EA, Haider MA, Fung S, Lockwood G, Dawson LA. Change in diffusion weighted MRI during liver cancer radiotherapy: preliminary observations. *Acta Oncol.* 2009: p. 1034-1043.

28. Yankeelov TE, Lepage M, Chakravarthy A, Broome EE, Niermann KJ, Kelley MC, et al. Integration of quantitative DCE-MRI and ADC mapping to monitor treatment response in human breast cancer: intitial results. *Mag. Reson. Imaging.* 2007: p. 1-13.

Chapter 6: ADC and T2 Responses in Tumors with Reduced Radiosensitivity

The previous two chapters described changes in ADC and T2 response when external treatment factors are varied – in chapter 4 the total dose to the tumour is varied, while in chapter 5 the fractionation schedule is varied. In this chapter, a state of reduced oxygenation is induced in tumours to assess the impact of radiosensitivity differences on ADC and T2 response. The results of these experiments are being submitted for publication (1).

6.1 Introduction

A common feature of many animal studies attempting to demonstrate a correlation between the degree of biological effect and the magnitude of MR parameter changes is the variation of the dose of the therapeutic agent to facilitate the change in biological effect. In this study we investigate how a variation in radiation sensitivity affects the response of ADC and T2. To facilitate this we use a suture-based ligature to induce ischemia and a corresponding reduction of oxygenation during irradiation of human glioma xenografts located subcutaneously over the thigh of mice. The practice of inducing hypoxia through the use of a clamp or tourniquet has been widely used and well-documented (2-7). Hypoxia is known to reduce the radiosensitivity of cells, and the presence of such cells in solid tumours is believed to be a significant cause of failure of radiotherapy (8-11). Therapeutic approaches to limiting hypoxia and its effects is an area of active research, including attempts to increase blood oxygen content, delivery of blood to cells, and modulating the biological effects of hypoxia on cellular radiosensitivity (10).

If ADC is to be used as a biomarker of tumour response to therapy in clinical settings, it is important to understand its reaction to variations in response due to hypoxia-induced radiosensitivity differences. The purpose of this study is to compare relative changes in tumour growth rate, T2, and ADC when tumours are irradiated in hypoxic versus normal conditions.

6.2 Methods

The details of these experiments closely followed those used in the two preceding chapters, and are discussed in detail in chapter 3, including the procedure for application of the ligature discussed in section 3.7.

NIH-iii nude mice of approximately 6 weeks of age were obtained from Charles River Laboratories (Wilmington, MA, USA). Human glioblastoma multiforme (GBM) cells of the line M006xLo (12) were used to initiate tumour xenografts as described in section 3.1.

Tumours were measured using digital caliper and tumour volumes were estimated assuming the tumour shape to be ellipsoid. Tumours were allowed to grow until they reached a volume of approximately 150 mm^3, at which point the tumours were slated for treatment. Six tumours were treated using with 800 cGy of 200 kVp x-rays while oxygenation in the tumour tissue was reduced by use of a tourniquet-style ligature. An additional six mice had the ligature identically applied, but received no radiation dose. Data for tumours treated to the same dose under normal conditions, as well as for normal controls, had previously been acquired (13,14), and were discussed in chapters 4 and 5. The procedure for application of the ligatures is described in section 3.7.

To assess the safety of the method, the ligature procedure was first applied to two healthy mice. Three days later, the mice were examined by a

veterinary pathologist. The mice were euthanized, and tissue samples were taken for histological examination, which revealed no detectable damage from the ligature.

Mice underwent MRI pretreatment and at multiple time points after treatment according to the imaging procedure described in detail in sections 3.3 and 3.4. All mice were imaged immediately preceding the delivery of radiation, or application of the ligature for the unirradiated tumours. All mice were subsequently imaged 1, 3, 5, 7, 11, and 14 days after radiation and/or ligation, to match the imaging time points of previously acquired treatment groups.

Maps of ADC and T2 were produced for all tumours as described in section 3.5, and relevant statistics for all tumours were extracted.

6.3 Results

A plot of tumour growth is shown in Figure 6.1, with the volume of each experimental group normalized to 100% at the time of treatment. Tumours treated with ligation only (LO) grew slightly faster when compared to previously reported (13) data for untreated tumours, although at no point did the differences in mean volume become statistically significant as judged by a two-sample t-test ($p > 0.10$ at all time points). Tumours that were irradiated while the ligature was applied (ligation + radiation, L+R) showed reduced growth rate after irradiation compared to controls. Post-treatment growth for both LO and

L+R groups was approximately linear. A linear least-squares fit to the average volume data gives a linear growth rate for LO tumours of (16.4 ± 1.3) mm^3/day, compared to a previously measured (15.0 ± 1.3) mm^3/day for unirradiated controls. Similar analysis for the L+R tumours gives a linear growth rate of (4.1 ± 0.5) mm^3/day. Previously reported data (13) for a group receiving the same radiation dose without the tourniquet (radiation only, RO) showed a negative growth rate of (-2.0 ± 0.5) mm^3/day. By this measure, the L+R therapy had a reduced effectiveness compared to the RO therapy, indicating a change in radiosensitivity. By 8 days post-treatment, there is a statistically significant difference in average tumour volume between the L+R and RO groups. From Figure 6.1, it is clear the post-treatment growth rate of the L+R group falls somewhere between that of the previously acquired data for groups treated with 400 and 800 cGy under normal conditions. Applying a linear-least squares fit to reported (13) growth rates as a function of dose, the interpolated "effective" dose of the L+R group is (452 ± 190) cGy.

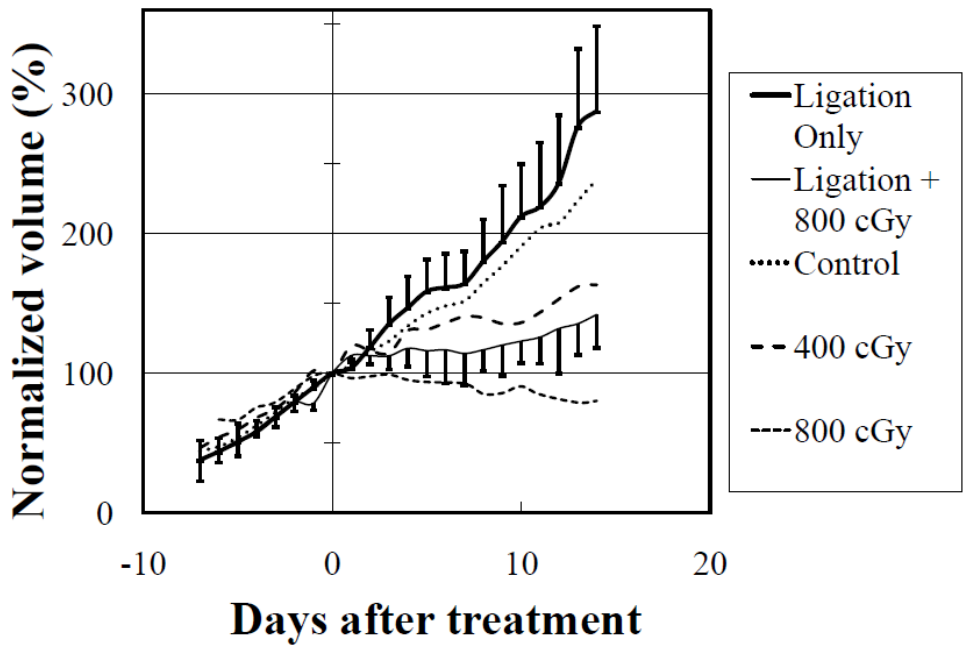

Figure 6.1. Tumour growth curves for tumours treated with 800 cGy while ligated, and tumours receiving ligation only. Previously reported data (13) showing growth curves for groups receiving 400 and 800 cGy without ligation, as well as for an untreated control group, are shown for the purpose of comparison. For clarity, error bars are shown only for ligation only and ligation + 800 cGy groups. At no time points was the difference between ligation only and control tumours statistically significant.

The time-dependent responses of mean tumour ADC are shown in Figure 6.2. Previously reported responses of the RO group (14) and an unirradiated control group are included for comparative purposes. Application of the ligature alone did not induce changes in mean tumour ADC. Tumours from the L+R group showed a significant (9.0%) increase in mean tumour ADC 24 hours after treatment. ADC remained elevated at all time points measured up to 14 days

after treatment. This elevation of ADC relative to both the LO group and the unirradiated control group was statistically significant ($p < 0.05$) for all measured time points post-treatment.

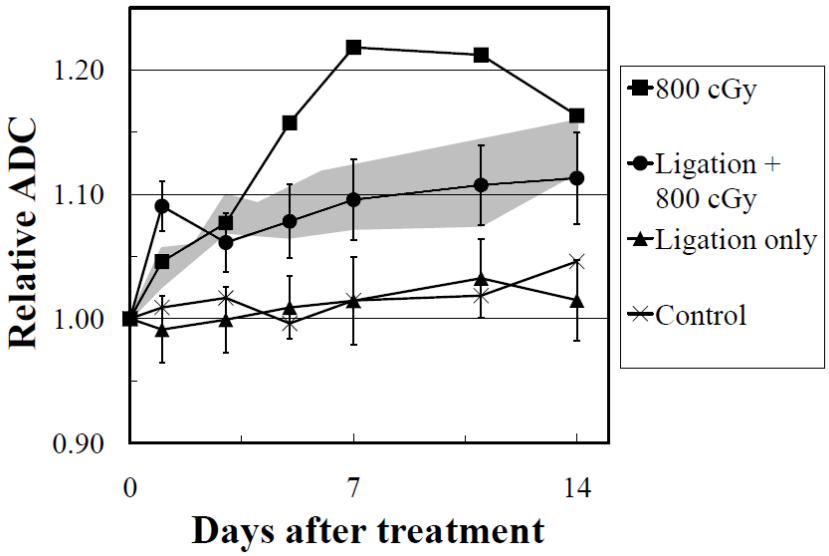

Figure 6.2. Time dependence of average post-treatment tumour ADC relative to the measured pretreatment value. Previously reported data (13) showing the response of groups receiving 800 cGy without ligation, as well as for an untreated control group, are shown for the purpose of comparison. The shaded region indicates the area between previously reported ADC response curves for groups treated with 200 and 400 cGy under normal conditions. For the purpose of clarity, error bars indicating one standard deviation are only included for the LO and L+R groups, but the size of these error bars are generally representative of those from other groups.

The relative ADC response in the L+R group is less than that of the RO group when measured 3, 5, 7, 11, and 14 days post-treatment. Only at 24 hours post-treatment is the response of the L+R group greater than that of the RO

group. At 5, 7, and 11 days post-treatment, the reduced ADC response of the L+R group is significantly different from the RO group ($p < 0.03$). By 14 days after treatment the mean tumour ADC of the RO group is returning to baseline and the difference in response is not significant ($p = 0.22$).

As shown in Figure 6.2, for the time period between approximately 3 and 14 days post-treatment, the ADC response falls in the region between that of previously acquired ADC response curves for groups irradiated with 200 and 400 cGy under normal conditions. We have previously found that for tumours treated with 800 cGy under normal conditions in 1, 2, or 3 fractions, the ADC response peaks at 7 days after the end of treatment. Applying linear-least squares fit to ADC values at this time point as a function of dose, the interpolated "effective" dose of the L+R group is (287 ± 141) cGy.

The time-dependent responses of mean tumour T2 are shown in Figure 6.3. Although the application of the ligature alone did not affect tumour growth rate or mean tumour ADC, it had a significant effect on mean tumour T2. The LO group shows a sharp reduction in T2 24 hours after application of the ligature, falling to 93.8% of the pretreatment value. Mean tumour T2 then returns toward both its value and the unirradiated control. The L+R group has a complicated T2 response – elevated 24 hours after treatment but depressed by 72 hours after treatment. After returning close to baseline 5 days post-

treatment, mean tumour T2 falls when measured 7, 11, and 14 days post-treatment.

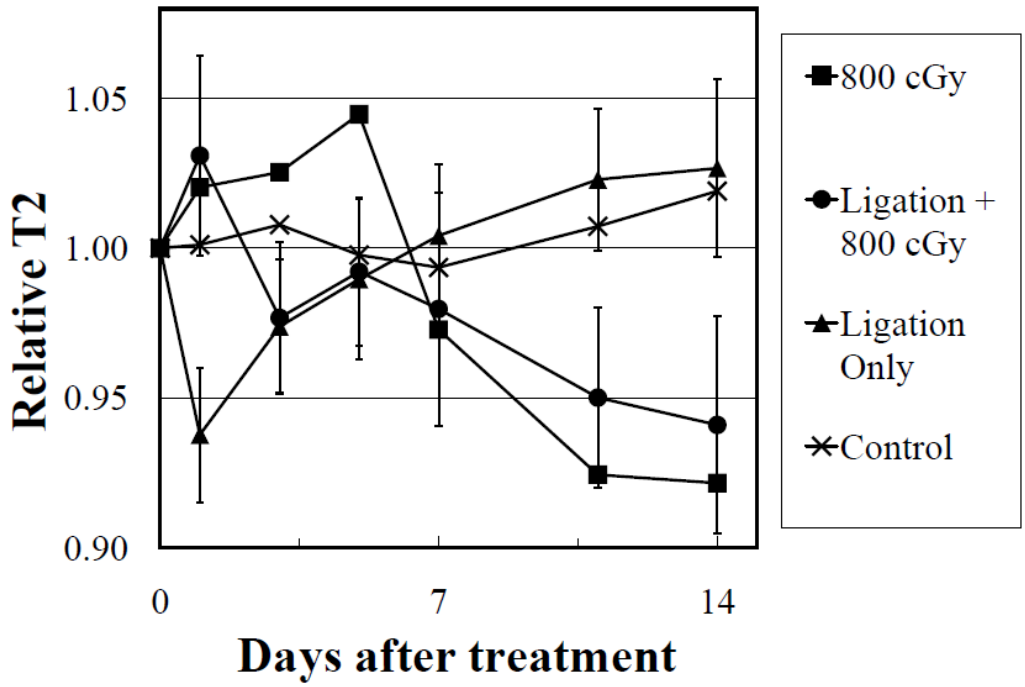

Figure 6.3. Time dependence of average post-treatment tumour T2 relative to the measured pretreatment value. Previously reported data (13) showing the response of groups receiving 800 cGy without ligation, as well as for an untreated control group, are shown for the purpose of comparison. For the purpose of clarity, error bars indicating one standard deviation are only included for the LO and L+R groups, but the size of these error bars are generally representative of those from other groups.

A time-series of histograms representing the ADC distributions within two tumours are presented in Figure 6.4. These tumours were chosen for having an individual ADC response similar to that of the average of their respective treatment groups. The difference histograms represent the normalized

pretreatment histogram subtracted from the normalized histogram at a given time point. For the tumour ligated but not irradiated there are no significant changes in ADC distribution until 11 days post-treatment, when the histogram shifts slightly towards greater ADC values. The tumour which was irradiated while ligated shows significant and sustained ADC response beginning 1 day post-treatment.

Descriptive statistics were calculated for each tumour at every measurement point. There were no significant changes in the group average variance, skewness, or kurtosis as a function of time in either the LO or the L+R groups.

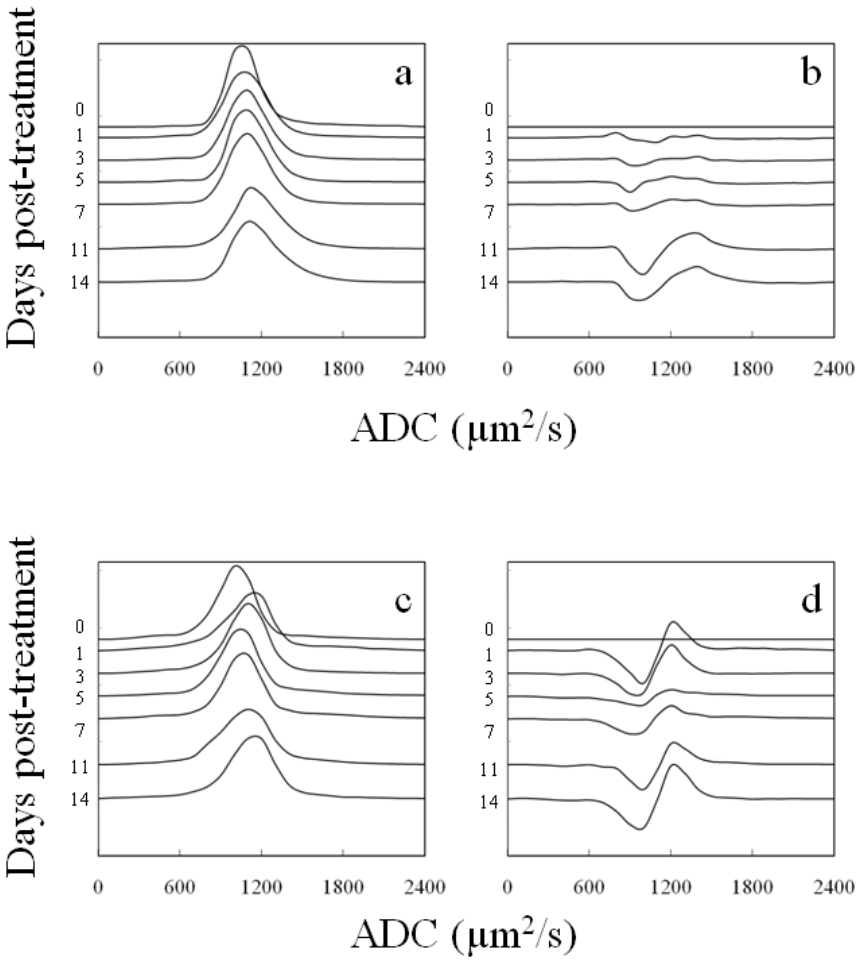

Figure 6.4. Histograms of ADC distributions (a,c) and associated difference histograms (b,d) for two representative tumours: one which had a ligature applied but no radiation (a,b) and one treated with 800 cGy while a ligature was applied (c,d). The area under each histogram is individually normalized, and all figures (a-d) are plotted on identical scale. Each histogram is vertically displaced proportional to the time between measurement of each histogram. The histogram labeled as zero days post-treatment was acquired immediately before treatment.

T2 histograms and difference histograms were generated for the same tumours, and are shown in Figure 6.5. The tumour that was ligated and not irradiated shows a shift to lower T2 values by the first day post-treatment. The

difference histograms at 11 and 14 days post-treatment show increased frequency of pixels at or above 50 ms. The tumour that was irradiated while ligated shows only minor fluctuations in the T2 histogram between 1 and 7 days post-treatment, and shows a more significant shift towards lesser T2 values 11 and 14 days post-treatment.

As with the ADC distributions, descriptive statistics were calculated for T2 distributions at all time points, but no trends were recognized in the average variance, skewness, or kurtosis values for either the LO or L+R group.

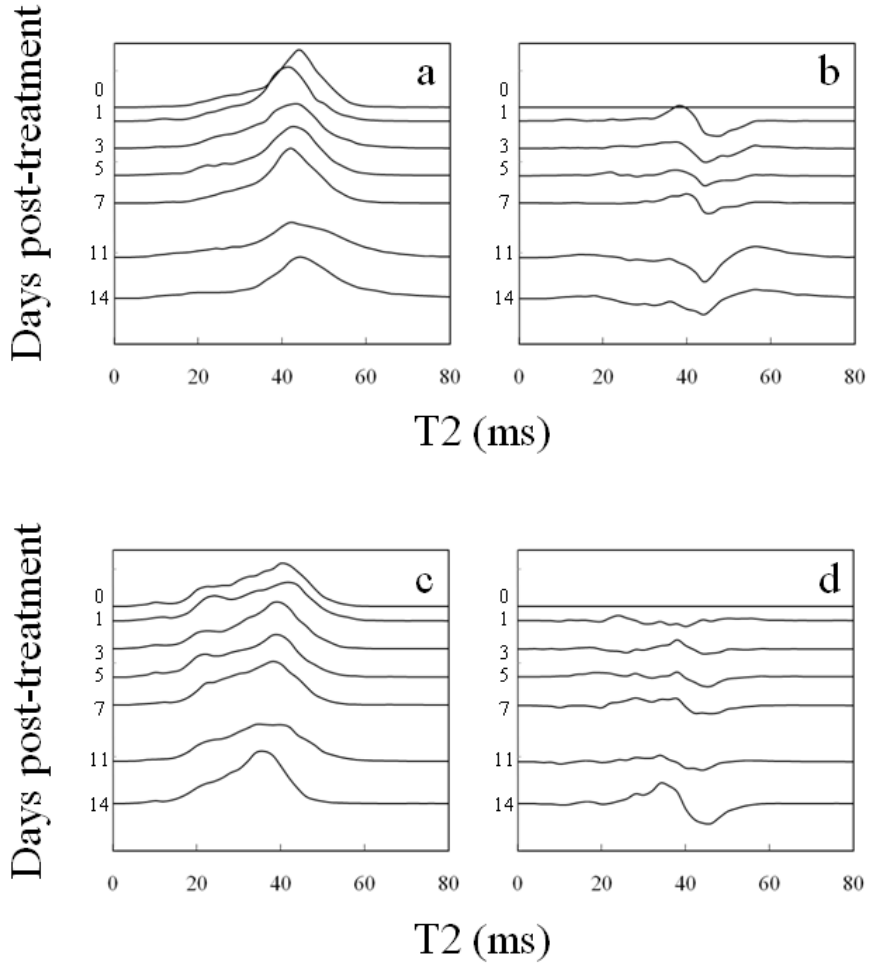

Figure 6.5. Histograms of T2 distributions (a,c) and associated difference histograms (b,d) for two representative tumours: one which had a ligature applied but no radiation (a,b) and one treated with 800 cGy while a ligature was applied (c,d). The area under each histogram is individually normalized, and all figures (a-d) are plotted on identical scale. Each histogram is vertically displaced proportional to the time between measurement of each histogram. The histogram labeled as zero days post-treatment was acquired immediately before treatment.

6.4 Discussion

In this study we use a ligature, applied above the tumor location on the leg, to restrict blood flow to the tumor and in turn reduce the oxygen supply of the cancerous cells. While we do not have a quantitative measure of the degree of hypoxia induced in tumours, a reduced effectiveness of radiation treatment was observed in tumours ligated during treatment, by way of a statistically significant difference in post-treatment growth rate compared to tumours unligated during treatment. This observation, combined with the observation of ligation alone not having a negative effect on tumour growth, strongly suggests tumour hypoxia being responsible for changes in radiosensitivity. Other indirect measures, such as cyanosis of the skin below the ligature, support this theory. We do not have quantitative information about the reproducibility of the induced hypoxia in all of the tumors used in this study, and so we rely on averaging the responses from multiple tumors.

A reduced effectiveness of radiation treatment for hypoxic tissues was measured both by post-treatment tumor growth and ADC response. Tumors irradiated under conditions of decreased oxygenation show a reduced growth rate relative to both untreated controls and ligated, but unirradiated tumors. The reduction in growth rate is smaller than that experienced by tumors irradiated to the same dose under normal conditions. Similarly, tumors irradiated under conditions of decreased oxygenation show a change in mean

tumor ADC relative to both control groups, but the increase in ADC is significantly less than that observed in tumors irradiated to the same dose while under normal conditions. Both of these observations are consistent with the fact that acute hypoxia reduces cellular radiosensitivity. Specifically, in the case of reduced radiosensitivity, reduced cell kill is expected. With reduced cell kill, smaller changes in cellularity and extracellular water content, and therefore ADC changes, are expected. Reduced ADC and growth rate response is also consistent with our previous observation that ADC response and post-treatment growth rate are negatively correlated (13).

It was also interesting to note that while application of the ligature did not affect tumor growth rate or tumor ADC, it did have a pronounced effect on tumor T2. The rapid onset of this T2 change is temporally correlated with the presence of petechial hemorrhage visible on the skin of the tumor and leg below the location of the ligature. Reduced T2 has previously been observed (15) in regions containing paramagnetic red blood cells (RBCs). This could partially account for the observed behavior in this case.

We have used a ligature to induce ischemia and hypoxia in order to create an altered response to radiotherapy, and have shown that ADC measurements are sensitive to this altered response. Tumors treated with 800 cGy while ligated had a post-treatment growth rate that fell between previously measured growth rates for tumors treated with 400 cGy and 800 cGy, while the

post-treatment ADC response fell between previously measured responses for tumors treated with 200 cGy and 400 cGy.

ADC is currently being tested as a biomarker for response to anticancer therapies. This is being done both in animal models and in clinical settings. Research on animal models often induces a varied response by comparing different dose levels of chemotherapy or radiation. Clinical research is often focused on the potential of ADC response to sort patient response versus non-response to therapy. Variation in response or non-response in the clinic depends on more than simply the physical radiation dose delivered to the tumor.

Demonstrating that ADC is a biomarker sensitive to varied response due to biological factors, as has been done here, is an important step in understanding the nature of ADC response as observed in the clinic. It is of interest to examine differential ADC responses due to variations in radiosensitivity, but comparison of ADC values between cell lines with known radiosensitivity differences may be complicated by other factors which vary between the tissues such as cellular density, interstitial pressure, and degree of vascularization. Here we have investigated the ADC response due to radiosensitivity differences present within a single tumor line when exposed to varied biological conditions.

References

1. Larocque MP, Syme A, Allalunis-Turner J, Fallone BG. ADC response to radiation therapy correlates with induced changes in radiosensitivity. *In press.*

2. Moulder JE, Rockwell S. Hypoxic fractions of solid tumors: experimental techniques, methods of analysis, and a survey of existing data. *Int. J. Radiat. Oncol. Biol. Phys.* 1984: p. 695-712.

3. Stevens G, Joiner M, Joiner B, Johns H, Denekamp J. Radiosensitization of mouse skin by oxygen and depletion of glutathione. *Int. J. Rad. Oncol. Biol. Phys.* 1995: p. 399-408.

4. Kataoka T, Mizuguchi Y, Yoshimoto M, Taguchi T, Yamaoka K. Inhibitory effects of prior low-dose x-irradiation on ischemia-reperfusion injury in mouse paw. *J. Radiat. Res.* 2007: p. 505-513.

5. Lu X, Hamilton JA, Shen J, Pang T, Jones DL, Potter RF, et al. Role of tumor necrosis factor-a in myocradial dysfunction and apoptosis during hindlimb ischemia and reperfusion. *Crit. Care Med.* 2006: p. 484-491.

6. Kuroda M, Inamura K, Tahara S, Kurabayashi Y, Akagi T, Asaumi J, et al. A new experimental system for irradiating tumors in mice using a linear accelerator under specific pathogen-free conditions. *Acta. Med. Okayama.* 1999: p. 111-

118.

7. Urano M, Nishimura Y, Kuroda M, Reynolds R. Are hypoxic cells critical for the outcome of fractionated radiotherapy in a slow-growing mouse tumor? *Radiother. Oncol.* 1998: p. 221-228.

8. Moulder JE, Rockwell S. Tumor hypoxia: its impact on cancer therapy. *Cancer Metastasis Rev.* 1987: p. 313-341.

9. Koutcher JA, Alfieri AA, Devitt ML, Rhee JG, Kornblith AB, Mahmood U. Quantitative changes in tumor metabolism, partial pressure of oxygen, and radiobiological oxygenation status postradiation. *Cancer Res.* 1992: p. 4620-4627.

10. Moeller BJ, Richardson RA, Dewhirst MW. Hypoxia and radiotherapy: opportunities for improved outcomes in cancer treatment. *Cancer Metastasis Rev.* 2007: p. 241-248.

11. Vaupel P, Mayer A. Hypoxia in cancer: significance and impact on clinical outcome. *Cancer Metastasis Rev.* 2007: p. 225-239.

12. Franko A, Parliament M, Allalunis-Turner J, Wolokoff B. Variable presence of hypoxia in M006 human glioma spheroids and in spheroids and xenografts of clonally derived sublines. *Br J Cancer.* 1998: p. 1261-1268.

13. Larocque MP, Syme A, Yahya A, Wachowicz K, Allalunis-Turner J, Fallone BG. Temporal and dose dependence of T2 and ADC at 9.4 T in a mouse model following single fraction radiation therapy. *Med. Phys*. 2009: p. 2948-2954.

14. Larocque MP, Syme A, Yahya A, Wachowicz K, Allalunis-Turner J, Fallone BG. Monitoring T2 and ADC at 9.4 T following fractionated external beam radiation therapy in a mouse model. *Phys. Med. Biol.* 2010: p. 1381-1393.

15. Henning EC, Azuma C, Sotak CH, Helmer KG. Multispectral quantification of tissue types in a RIF-1 tumor model with histological validation. Part I. *Mag. Reson. Med.* 2007: p. 501-512.

Chapter 7: Histological Analysis

In the previous three chapters, data were presented to describe the response of the tissue parameters ADC and T2 to a series of radiation therapy experiments. In an effort to explain the underlying physiological mechanisms responsible for these behaviors, a series of tumour xenografts were prepared for histological evaluation. Tumours were treated using the same technique described in chapters 4, 5, and 6, and were sacrificed at various time points. Other tumours were used as untreated controls, and sacrificed when their volume reached the typical pretreatment size, or when they had grown very large and changes in ADC or T2 were observed. Microscope slides were prepared for all tumours using a variety of commonly-used staining methods, as well as a stain for a hypoxia marker.

These slides were reviewed a pathologist from the Department of Laboratory Medicine and Pathology at the Cross Cancer Institute. The purpose of this chapter is to present these histological results and discuss the implications of these findings on the interpretation of observed ADC and T2 behaviors after radiation treatment.

7.1 Introduction

The hematoxylin and eosin (H&E) stain is the most widely used diagnostic stain in pathology (1). The basis for the popularity of the H&E stain is a result of the relative simplicity of preparation, cost-effectiveness, and "ability to demonstrate clearly an enormous number of different tissue structures" (2). A combination stain, H&E stained slides are stained with both hematoxylin, which stains nucleic acids dark blue, and eosin, which stains proteins and amino acids shades of red. In effect, H&E-stained cells have a dark blue nucleus with cytoplasm and extracellular connective structures stained red. Virtually all of the available literature discussing histological analysis of ADC and/or T2 changes in post-treatment tumours include H&E stained sections in their analysis. Along with a multitude of other features, H&E sections can be used to identify areas of necrosis, edema, and cells undergoing apoptosis or mitosis.

Hypoxyprobe is a commercially available preparation that is used to identify regions of hypoxia in tissue. As discussed in section 3.8.1, the hypoxia marker, injected before euthanization, forms covalent bonds with proteins,

peptides, and amino acids within hypoxic cells. The resulting adducts can be stained after dissection using an antibody-based assay. Cells that were hypoxic at the time of hypoxia marker circulation are stained brown/black against a light blue counterstain.

Periodic acid-Schiff (PAS) staining identifies carbohydrate macromolecules (1) by staining them dark red. A PAS stain with diastase (PAS+D) stain can be used as a negative control for glycogen. The added diastase digests glycogen present in the section, resulting in glycogen staining positive in the PAS section, but being absent in the PAS+D section. Extracellular glycogen accumulation has been previously observed in irradiated brain tissue (3,4). Possible explanations for this accumulation include release of normal glycogen content and structural carbohydrates from damaged cells, and/or inhibition of aerobic glycolisis.

As previously discussed, tissue ADC is known to be sensitive to cellular size, extracellular volume, membrane permeability, and temperature (5). Multiple studies have shown increases in tumour ADC to be associated with a decrease in cellular density, increase in tumour extracellular space, pleomorphism (change of the size and shape of cells), appearance of giant cells and increased cells undergoing apoptosis (6-9).

Multiple investigators have performed histological analysis in an effort to explain T2 distributions within tumour tissue. T2 has been shown to be sensitive

to multiple aspects of tissue physiology including free water abundance, macromolecular content, and necrotic fraction (10,11). Water molecules bound to large proteins are associated with rapid T2 decay (12). One study observed decreases in tumour cell density and T2 in chemotherapy-treated tumours, as well as a decrease in mitotic cells and an increase in apoptotic cells (13). A study that measured both ADC and T2 found two distinct necrotic regions within a single tumour – one region with elevated ADC and T2, and a second region with elevated ADC but reduced T2 (9). The region with elevated ADC and T2 had advanced necrosis and was noted as "generally acellular" and relatively homogeneous with properties close to that of bulk water. The region with elevated ADC but reduced T2 showed a reduced population of cells intermixed with red blood cells (RBCs). Also observed were neutrophils (a type of white blood cell) likely recruited by the presence of RBCs. The authors of the study hypothesize that protein accumulation via neutrophils action and the presence of the paramagnetic RBCs contribute to the shortened T2 values in this region. The existence of many known physiological factors driving increases and decreases in T2 makes interpretation of observed T2 changes difficult. A purpose of this chapter is to use histological methods to better understand the T2 behavior observed in our tumour model after treatment with radiation.

7.2 Methods

Time points for extraction of histological samples were chosen based on the previously observed time-dependent responses of ADC and T2 after treatment. A total of five tumours served as untreated controls. Three of these tumours were taken from mice euthanized when the tumour had reached the volume at which treatment would typically be started (150 mm^3). Two more tumours were sacrificed at significantly later time points, when natural tumour growth had begun to induce changes in ADC, which had been similarly observed in previous control tumours. Figure 7.1 shows the specific ADC and T2 behaviors of the two late-time-point tumours sacrificed for histology.

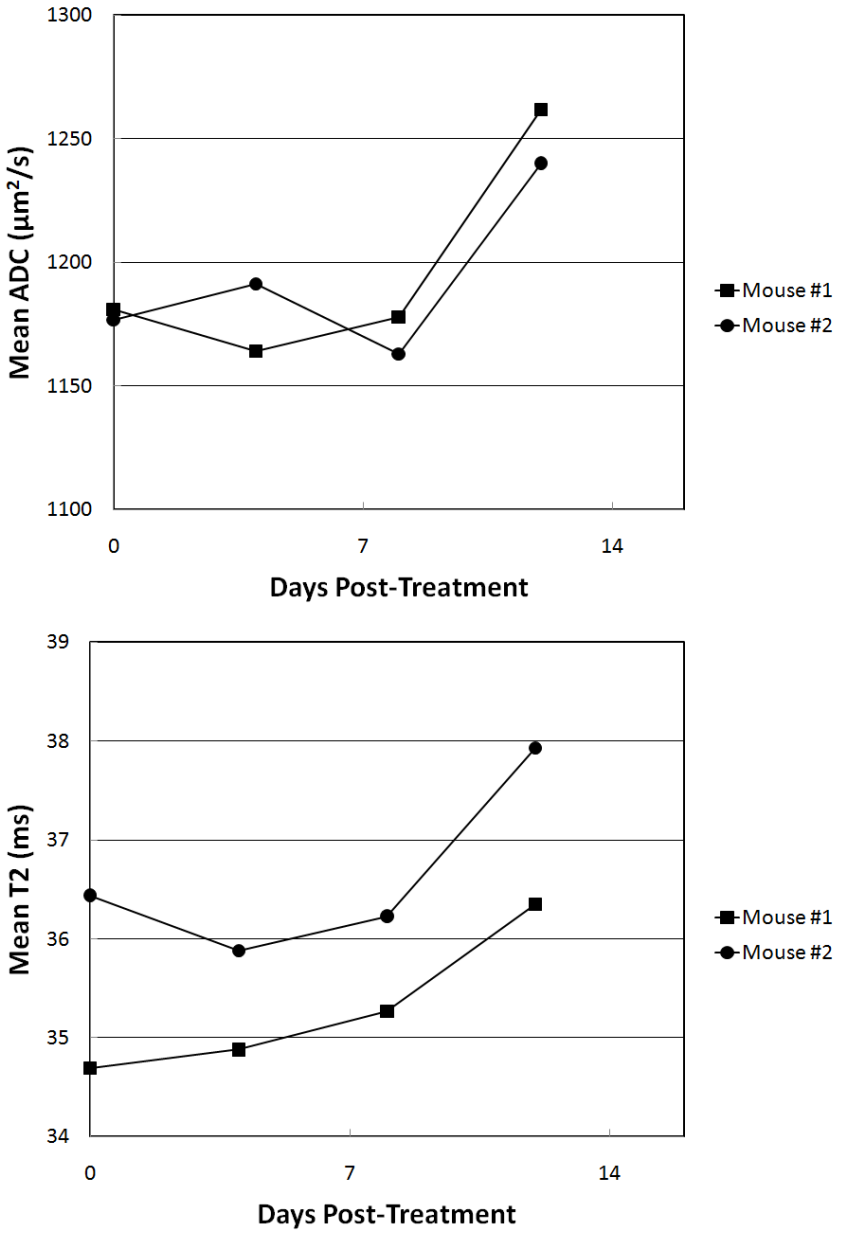

Figure 7.1. Individual responses of two untreated tumours sacrificed for histology. Increased ADC had been previously observed in untreated tumours with increasing volume. For all untreated tumours "days post-treatment" refers to the number of days after arrival at the predetermined treatment volume.

A total of six tumours were sacrificed after treatment with a single fraction of 800 cGy. Three of these tumours were taken 3 days after treatment, when both ADC and T2 values were elevated relative to pretreatment values. The other three tumours were taken 14 days after treatment, when ADC remained elevated, but T2 was significantly less than the pretreatment value. Figure 7.2 shows the average ADC and T2 response for all tumours in the treatment group, with the times at which samples from treated tumours were taken for histology highlighted.

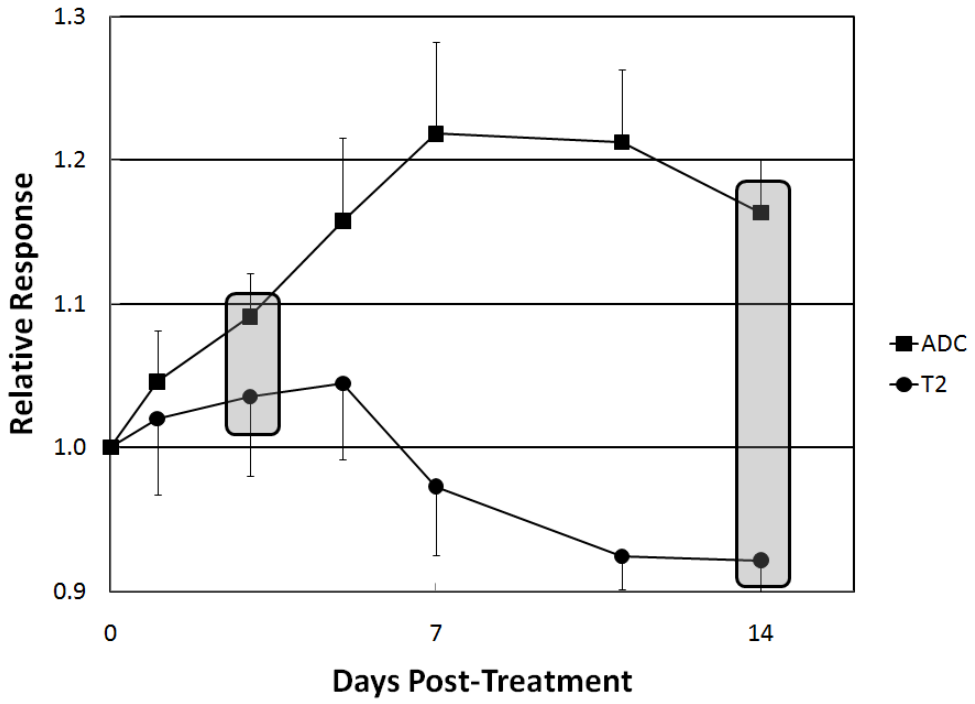

Figure 7.2. Average time-dependent responses of ADC and T2 for tumours treated with a single fraction of 800 cGy. Shaded boxes highlight the time points at which three tumour-bearing mice were euthanized for histology.

A total of 12 tumours were sacrificed for histology after ligation or treatment with radiation while ligated, as described in chapter 6. Tumours treated with ligation only had shown a decreased T2 24 hours after ligation, which then returned to baseline, while ADC values were unaffected. Three ligation-only tumours were sacrificed at the 24 hour time-point, and three tumours were sacrificed 14 days after ligation. The same number of tumours was sacrificed at matching time points after irradiation while being ligated. Figure 7.3 shows the group average ADC and T2 responses for these groups with the time points at which tumours were sacrificed highlighted.

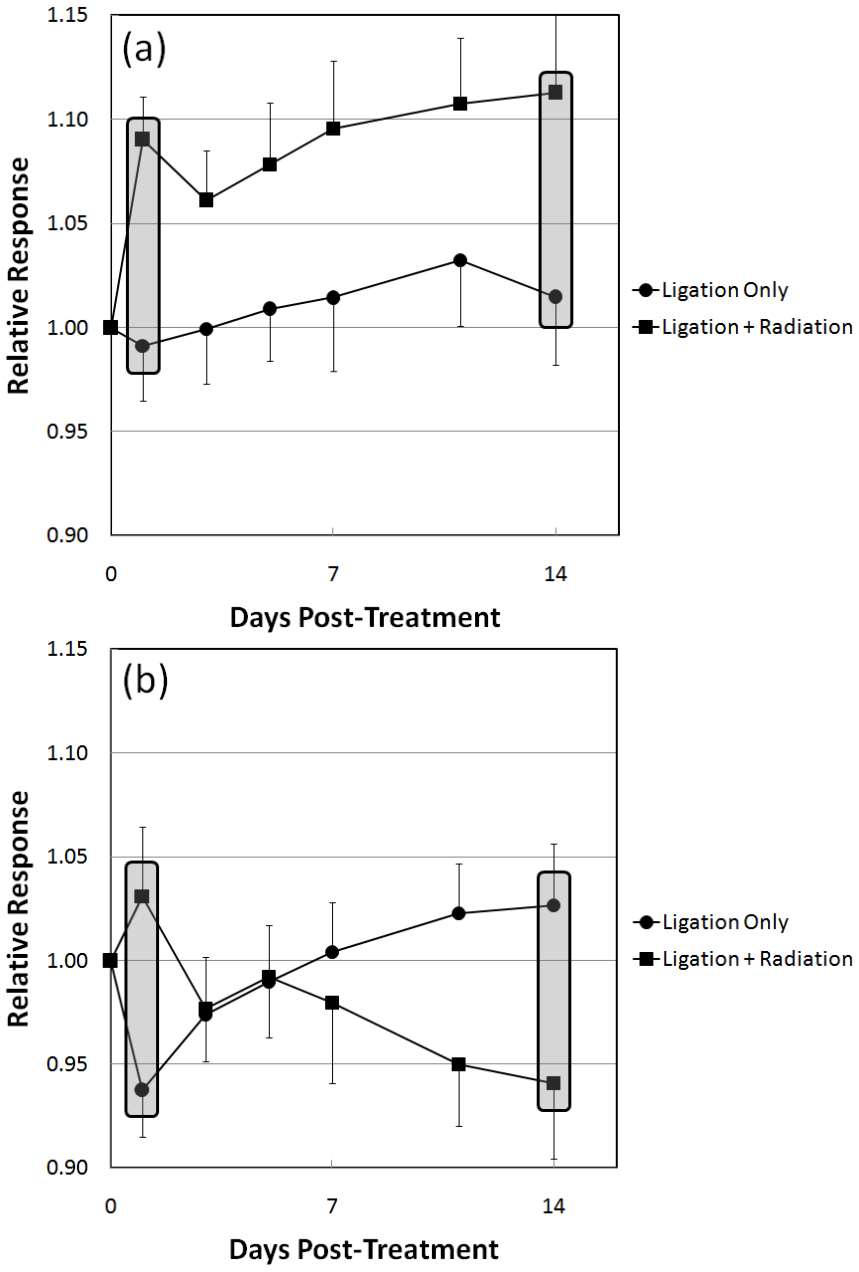

Figure 7.3. Average time-dependent responses of ADC (a) and T2 (b) for tumours temporarily ligated, and tumours irradiated with 800 cGy while ligated. Shaded boxes highlight the time points at which three tumour-bearing mice were euthanized for histology.

Reading of the histological data was performed by a pathologist at the Cross Cancer Institute. All slides were reviewed in a blinded manner. To establish a scoring system for the slides, a sample of slides from the different groups were reviewed to allow the pathologist to observe the range of values the various parameters of the tests could take. Based on this initial review, the various stains were used to evaluate the following properties of each tumour:

- necrosis as a function of percent of total tumour area using the H&E-stained sections
- edema as a function of percent of total tumour area using the H&E-stained sections
- approximate mitotic cell count (estimated number of cells undergoing mitosis in viable tumour tissue on H&E section as viewed with a 40x ocular lens)
    - scored as <5, 5-10, 10-15, or >15
- hypoxia marker staining as a function of total tumour area using the Hypoxyprobe-1-stained sections
- relative presence of identifiable extracellular glycogen granules in PAS-stained sections, viewed with a 40x ocular lens, on a scale of 0 to 3, with the following interpretations:
    - 0 = very few or no readily detectable glycogen granules
    - 1 = a low number of small granules are detectable

- 2 = moderate number of granules detectable, most small in size
- 3 = moderate or high number of granules, with some large in size

On each PAS-stained section, five distinct locations were randomly selected for evaluation under a 40x ocular lens by the pathologist. Each location was assigned an independent score. The scoring of the PAS-stained sections was the most subjective set of readings.

7.3 Results

7.3.1 Features of interest

As suggested by the scoring system, several pathological features of interest were identified among the samples. Figure 7.4 shows a tissue section comprised of mostly viable, densely packed tumour cells. Cell density is approximately uniform, with relatively little intercellular space.

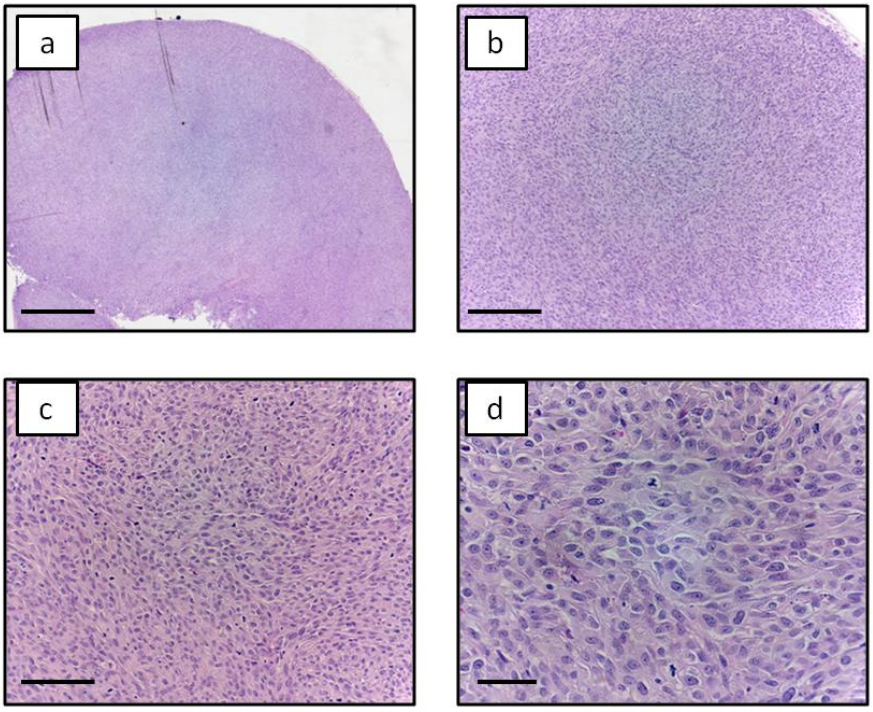

Figure 7.4. Photomicrographs of H&E-stained tumour sections at increasing magnifications. Scale bars are 1.0 mm (a), 250 µm (b), 125 µm (c), and 50 µm (d). Densely packed, viable cells are shown.

In contrast to sections of viable cells, obvious features of many tumours were regions of necrotic tissue. Figure 7.5 shows a tissue section with a clearly visible necrotic region, highlighted by arrows. The necrotic region is largely devoid of cells, and some cellular remnants are visible. These regions were typically filled with a combination of fluid, cellular debris, and some connective tissue.

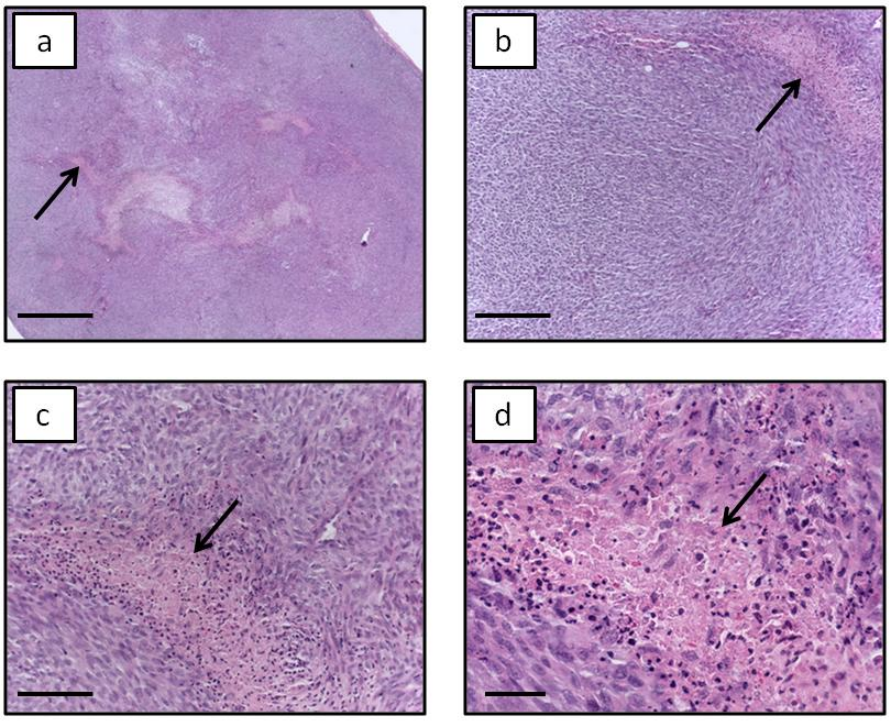

Figure 7.5. Photomicrographs of H&E-stained tumour sections at increasing magnifications. Scale bars are 1.0 mm (a), 250 µm (b), 125 µm (c), and 50 µm (d). The section contains a necrotic region, which is highlighted by the arrows.

Some tumour samples were identified as having widespread edema, where the extracellular space was enlarged and fluid-filled. Figure 7.6 shows a tumour in which a localized region of edema is present.

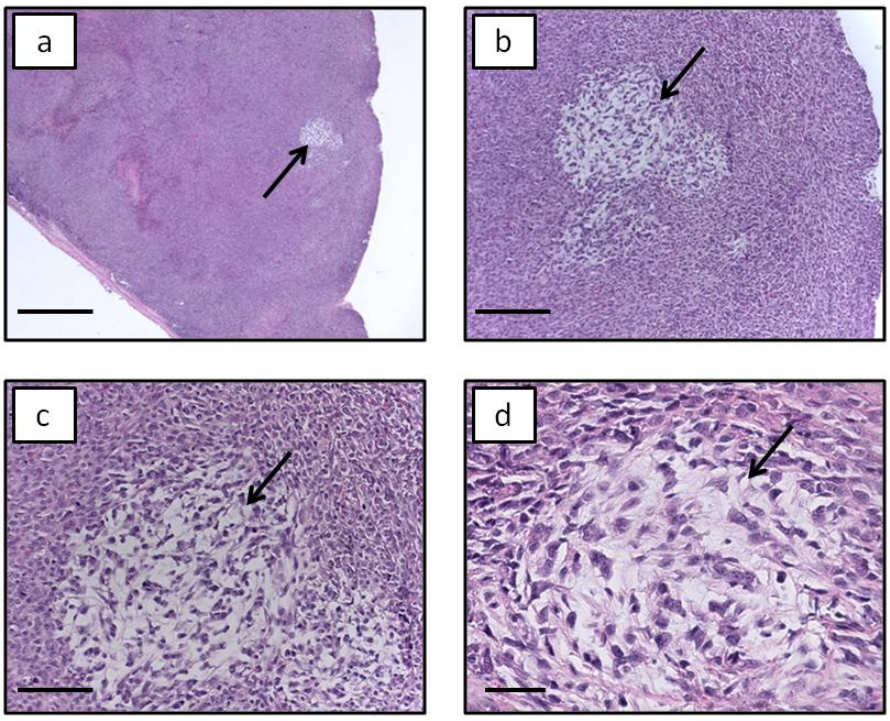

Figure 7.6. Photomicrographs of H&E-stained tumour sections at increasing magnifications. Scale bars are 1.0 mm (a), 250 µm (b), 125 µm (c), and 50 µm (d). The section contains a region of edema, which is highlighted by the arrows.

Another recurrent feature of several tumours was the accumulation of granules detectable using high-magnification views of the PAS-stained sections. These granules appeared red in the PAS sections, but were not present in either the H&E or PAS+D stained sections, leading the pathologist to identify them as glycogen. Figure 7.7 shows sections from two tumours – one with the glycogen granules, and one without.

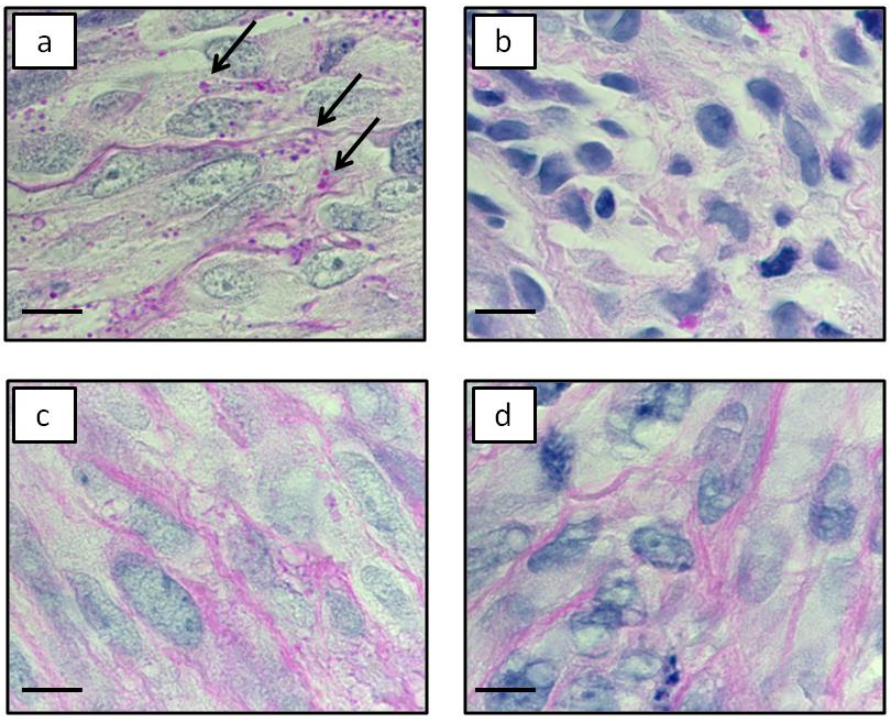

Figure 7.7. Photomicrographs of tumour sections at high magnification. Scale bars are 10 µm. A PAS-stained slide shows accumulated glycogen granules highlighted by arrows (a) which are absent in a corresponding PAS+D-stained slide (b). Also shown is a PAS-stained slide from a tumour without accumulated glycogen (c), and the corresponding PAS+D slide (d), which is also negative for glycogen.

7.3.2 Identifiable patterns

Ranges of observed values for necrosis, edema, mitotic cell counts, and hypoxia marker are given in Table 7.1. The reported ranges encompass the minimum and maximum reported score over all tumours for the listed treatment group. When the pathologist reported a range of values for a particular tumour (for example, "necrosis by area is 5-10% for sample A"), then the reported range

includes the full range for this tumour. Figure 7.8 shows the same data plotted in bar graph form. For this figure, if a particular tumour was scored as a range of values, the mean value is plotted.

Table 7.1. Range of observed values for tumour samples from multiple treatment groups at multiple time points after treatment, including tumours receiving radiation only (RO), ligation only (LO), and radiation while ligated (L+R).

Treatment Group	Necrosis % area	Edema % area	Mitotic Cell # per 40x field	Hypoxia % area
Control	10-15	0-5	15-20	10-15
XL Control	40	0-10	15	20-30
3 d RO	0-20	20-30	5-10	0-10
14 d RO	5-10	30	5-10	0-10
1 d LO	5-20	0-10	10-15	0-10
14 d LO	30-40	0-10	10-15	5-30
1 d L+R	0-20	5-10	5-15	0-15
14 d L+R	0-10	20-40	5-15	0-10

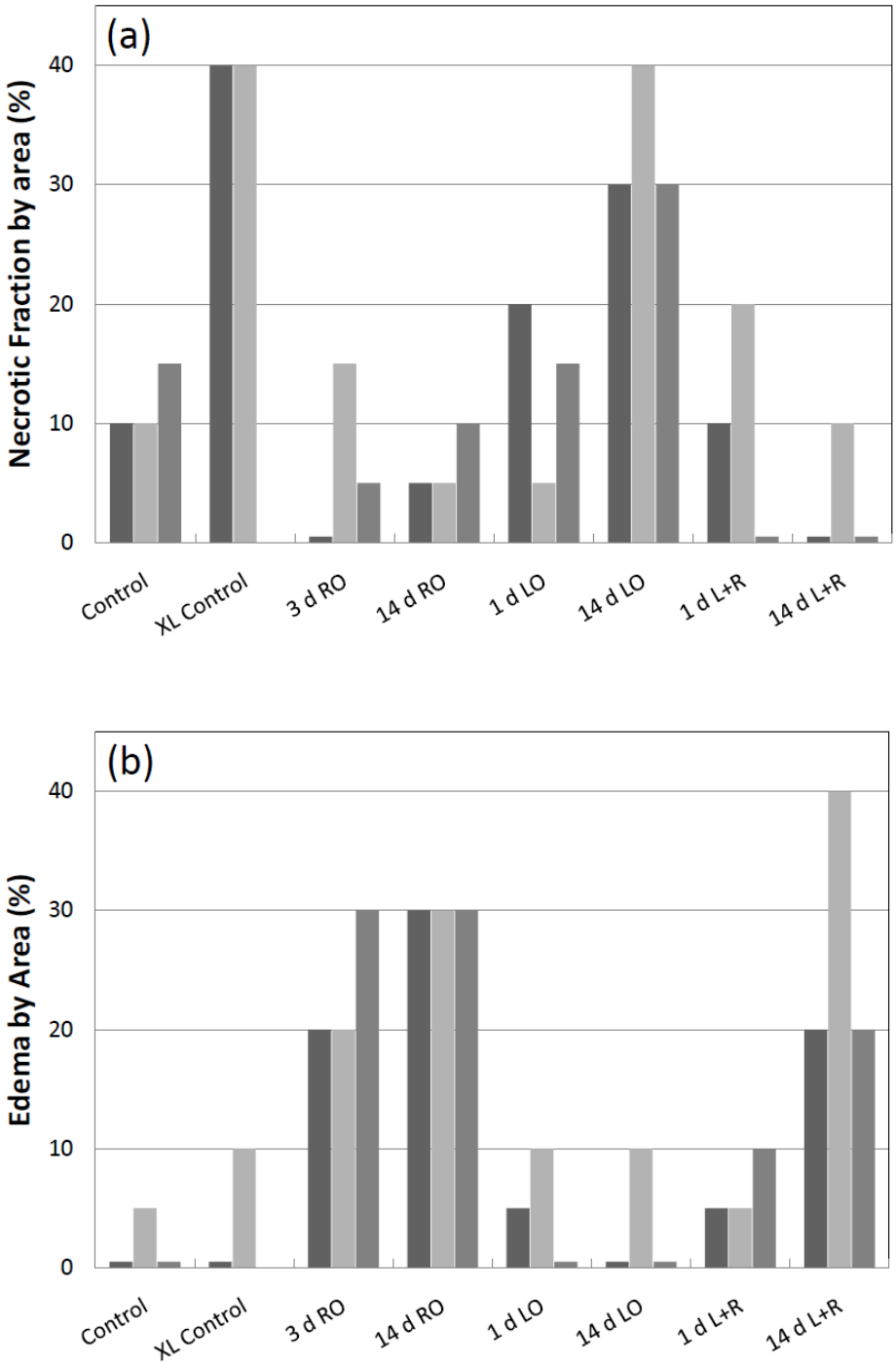

Figure 7.8. (caption follows on next page)

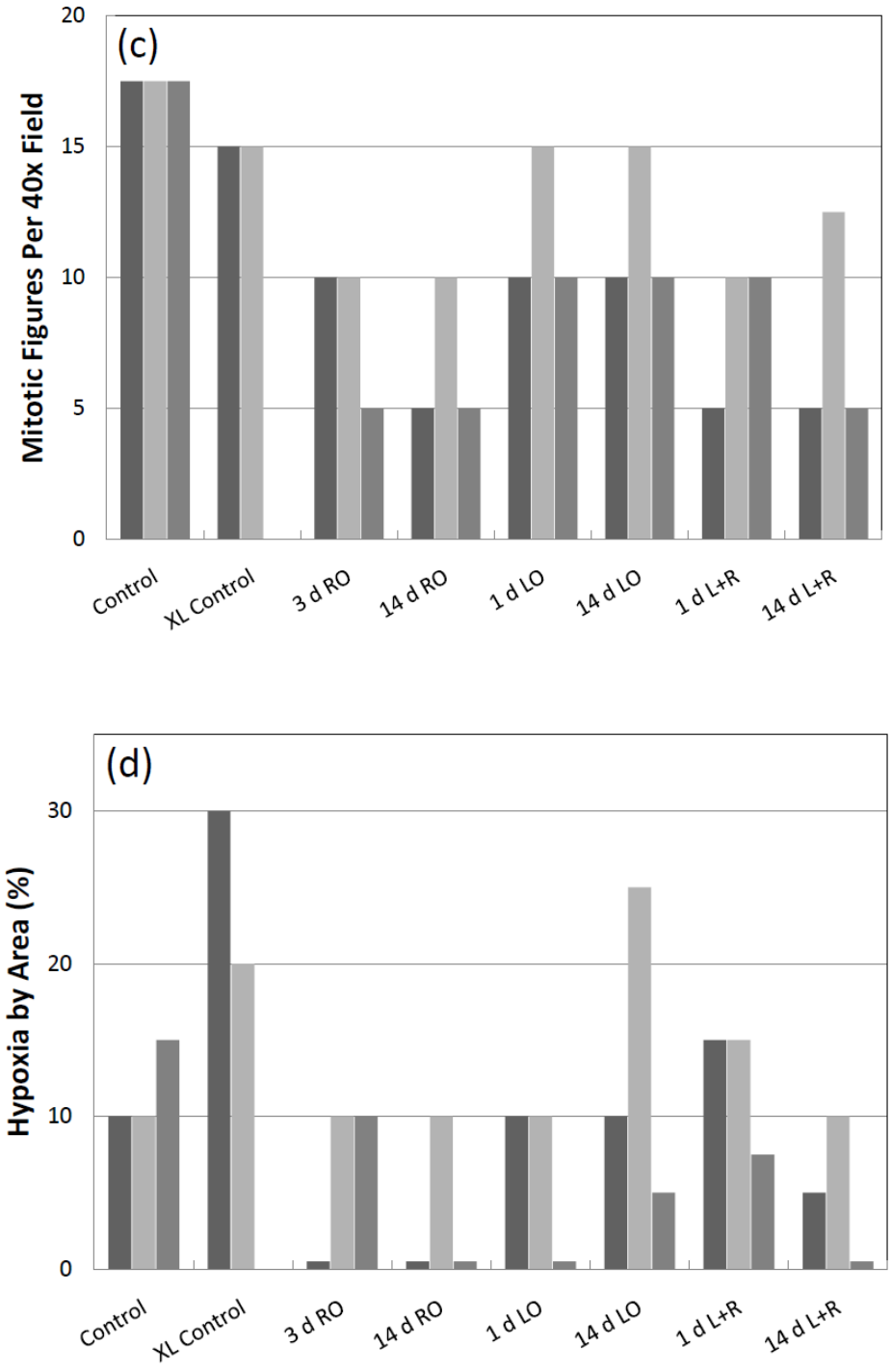

Figure 7.8. Bar charts showing scores for all tumours in each treatment group for necrosis by area (a, previous page), edema by area (b, previous page), mitotic cells per 40x field (c), and hypoxia by area (d). Where ranges of values were reported, the mean score is plotted.

Low-magnification images of H&E-stained tissue sections from three untreated tumours sacrificed at normal treatment volume are shown in Figure 7.9. Pathological analysis of these sections characterized them as being composed of densely-packed viable cells, with relatively small, localized regions of necrosis (approximately 10% of section area). Mitotic cell count was consistently 15-20 mitotic cells per 40x field, and there was a relatively low presence of extracellular glycogen.

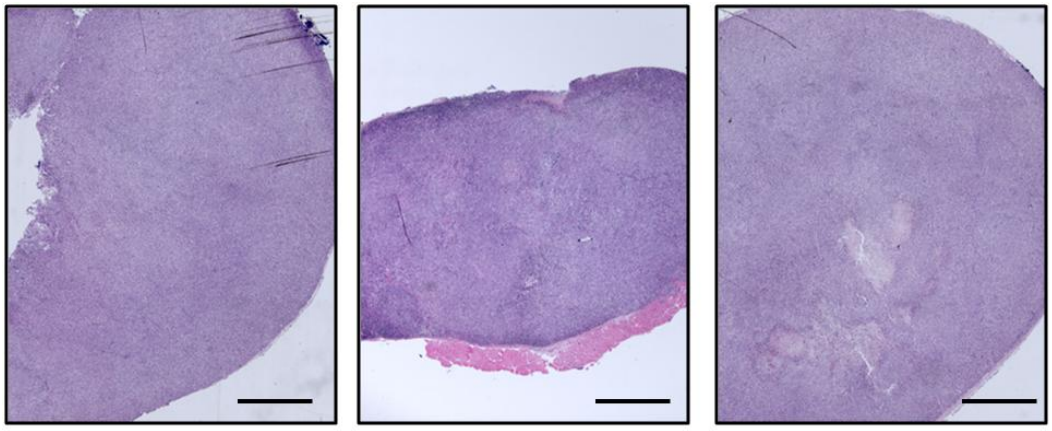

Figure 7.9. Photomicrographs of H&E-stained tissue sections from three untreated tumours. Tumour volumes at time of dissection were approximately 150 mm^3. The tumour sections are largely composed of dense, viable cells, although localized regions of necrosis are visible in two of the three sections (centre, right). Scale bars in each image are 1.0 mm long.

Identical images from two untreated tumours sacrificed at larger volumes, shown in Figure 7.10, reveal a significantly higher percentage of non-viable tissue. These tumours were assessed as having approximately 40%

necrotic tissue by area. Large, completely acellular necrotic regions are visible. Large regions of dense, viable cells are still present, and in these regions, mitotic cell count is still high (approximately 15 mitotic cells per 40x field), and glycogen accumulation remains low.

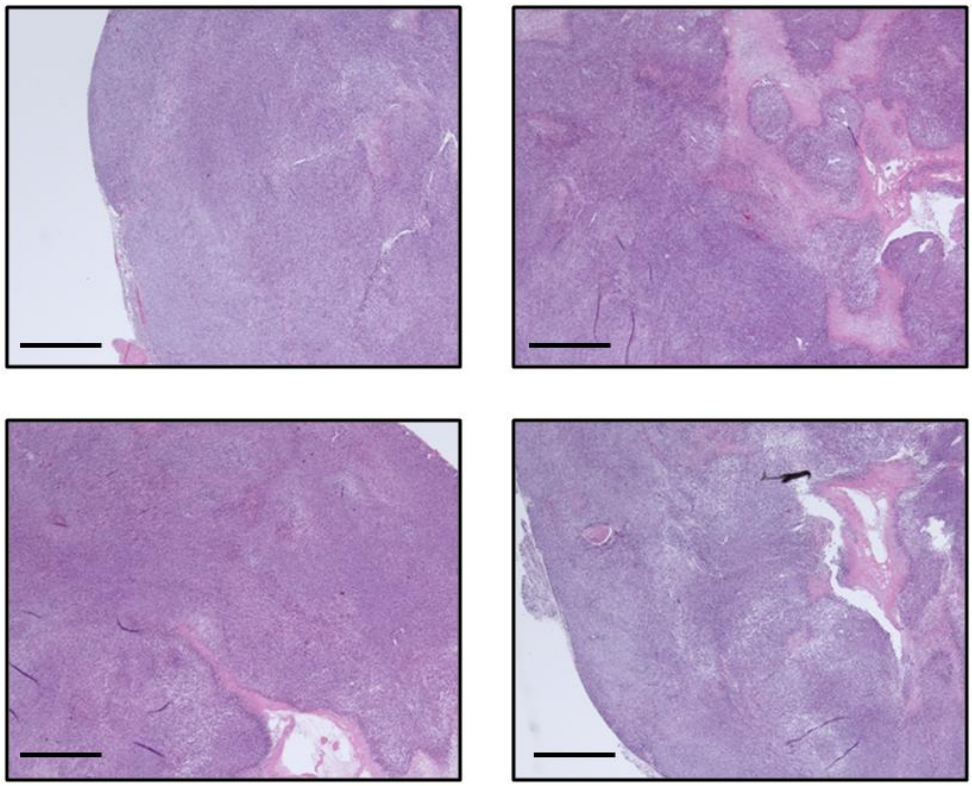

Figure 7.10. Photomicrographs of H&E-stained tissue sections from two untreated tumours, sacrificed at large volume. Tumour volumes at time of dissection were approximately 600 mm^3 (top images) and 700 mm^3 (bottom images). The tumour sections contain regions of dense, viable cells and distinct regions of extreme necrosis (stained pink or completely accelular). Scale bars in each image are 1.0 mm long.

Figure 7.11 shows three tumours dissected three days after treatment with 800 cGy of 200 kVp photons. Widespread edema is clearly visible in all

three cases. Pathological analysis scored these three tumours with 20% - 30% edema by area, and approximately 10% necrotic tissue by area. Mitotic cell count was reduced (5-10 mitotic cells per 40x field), and glycogen accumulation was elevated.

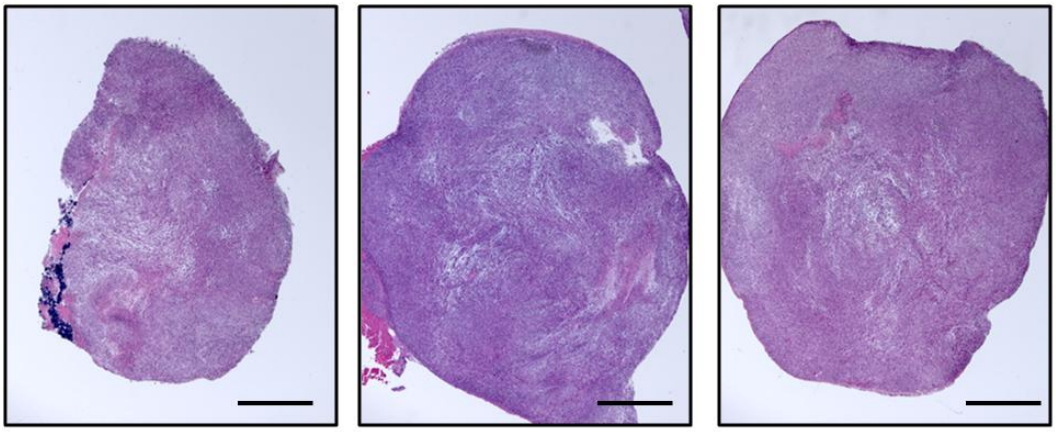

Figure 7.11. Photomicrographs of H&E-stained tissue sections from three tumours treated with 800 cGy of 200 kVp photons, and dissected three days post-irradiation. The tumour sections contain some regions of dense, viable cells, but show large regions of reduced cellular density and edema. Scale bars in each image are 1.0 mm long.

Figure 7.12 shows three tumours dissected 14 days after treatment with 800 cGy of 200 kVp photons. As with Figure 7.11, widespread edema is clearly visible, and was rated as approximately 30% by area. Necrotic tissue was rated between 5% and 10% by area. Glycogen accumulation was elevated relative to the control and the samples taken 3 days post-treatment.

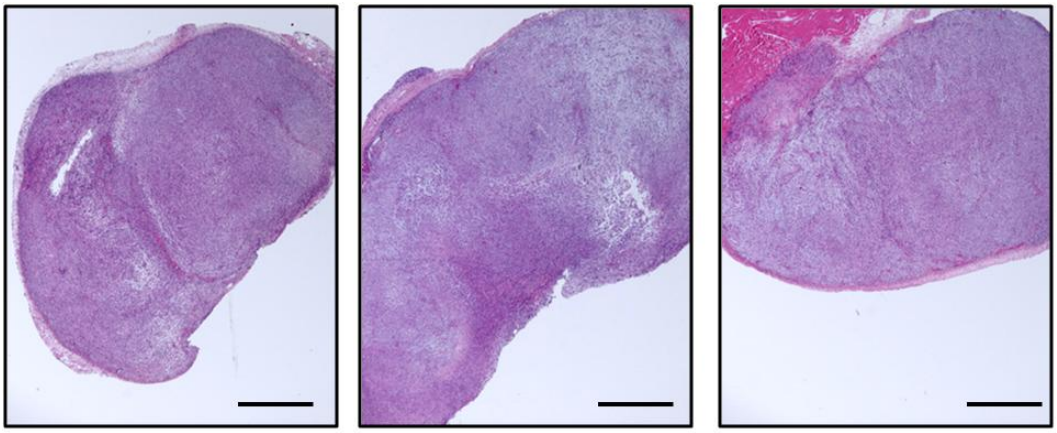

Figure 7.12. Photomicrographs of H&E-stained tissue sections from three tumours treated with 800 cGy of 200 kVp photons, and dissected fourteen days post-irradiation. The tumours show reduced cellular density relative to both controls and tumours dissected three days post-irradiation. Viable cells are still present, but dense populations are limited to relatively small areas. Scale bars in each image are 1.0 mm long.

The PAS-positive granule scores are shown for the control cases and 3 day and 14 day post-treatment cases in Figure 7.13. The PAS scoring system used categories, rather than quantitative analysis, therefore chi-square statistics were generated to test for significant variation in the distribution of observed scores between the three cases shown in Figure 7.13. The chi-square test requires that not more than 20% of the expected frequencies be less than 5, and no single expected frequency be less than 1 (14). In this case, the expected frequencies are the observed scores in the control. Of all of the observed locations in all control tumours, only four of the locations were assigned a score of 2, and only one location a score of 3. Therefore, the expected frequencies for scores in category “2” and category “3” are both less than 5. For this reason, the

two adjacent categories were combined, such that all scores of 2 and 3 were put in the catagory “2+”, which now has an expected frequency of 5 and meets the criteria.

While ideally all observations should be independent, in this case the observations consist of multiple randomly observed fields within the same tumours. The chi-square method, even if not ideally applied in this case, gives a sense of the differences between control and post-treatment cases. A significant change in the frequency of scores was observed for both the 3 day post-treatment (χ^2 = 10.0, degrees of freedom = 2, $p < 0.01$) and 14 day post-treatment (χ^2 = 30.0, degrees of freedom = 2, $p < 0.0001$) cases relative to the control. This suggests elevated extracellular glycogen accumulation in both the post-treatment cases relative to the control. When comparing the 14 day post-treatment cases to the 3 day post-treatment cases, the lowest two scoring categories were combined, and the chi-square test indicated a significant increase in glycogen accumulation in the 14 day post-treatment cases relative to those 3 days post-treatment (χ^2 = 7.6, degrees of freedom = 2, $p = 0.02$).

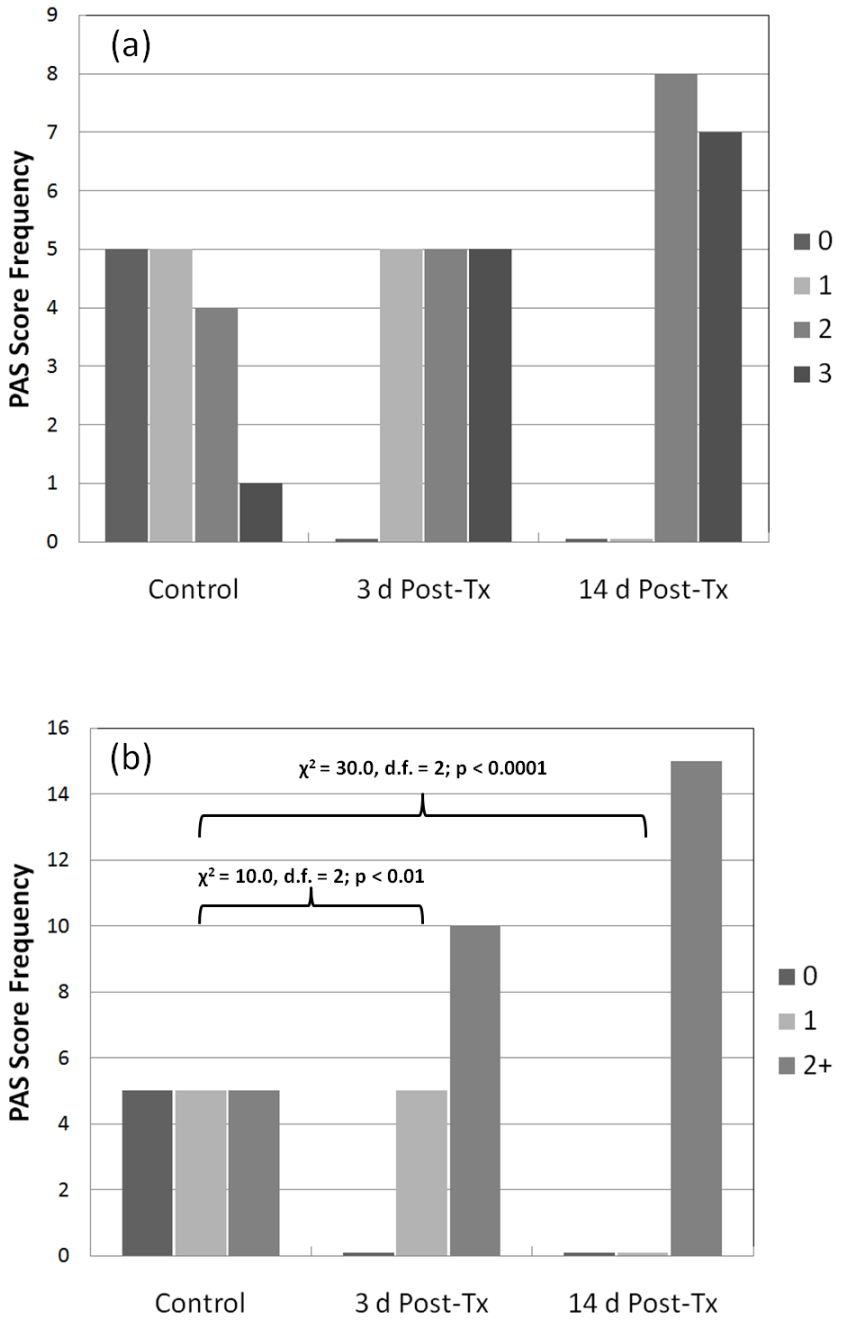

Figure 7.13. (caption follows on next page)

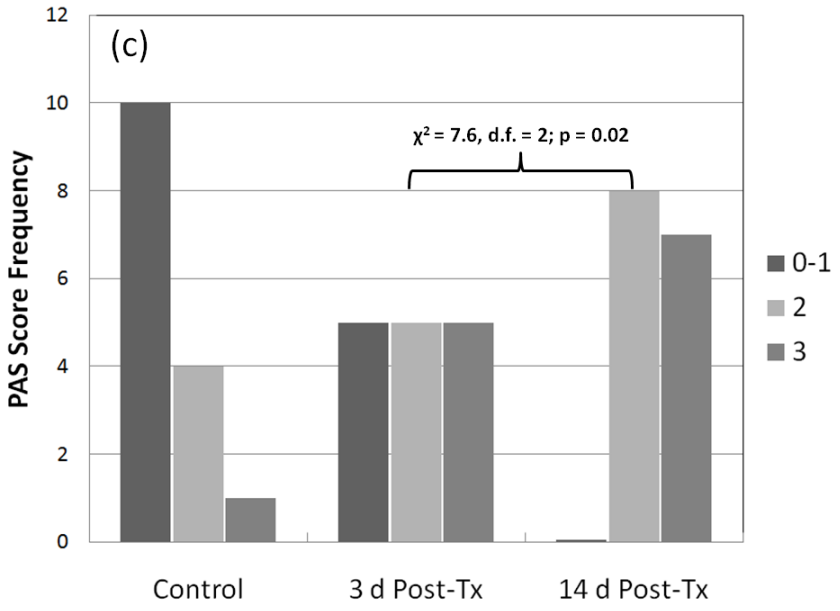

Figure 7.13. Bar charts showing frequency of fields scoring on PAS scoring scale for control and two post-treatment cases. Frequencies of all four scoring categories are shown in (a). For χ^2-testing, categories 2 and 3 are combined, as shown in (b). Both post-treatment cases show significant changes in scoring pattern, indicated increased glycogen accumulation in these samples. For χ^2-testing of the 14 day post-treatment cases against the 3 day post-treatment cases, categories 0 and 1 are combined, as shown in (c). A significant change in pattern between the two cases indicated increased glycogen accumulation in the 14 day cases relative to the 3 day post-treatment cases.

Ligation-only tumours did not have significant edema present at either sampled time point (between 0 and 10% by area). Chi-square tests showed no significant change in glycogen accumulation relative to control tumours at either time point. Necrosis was relatively high in the samples taken 14 days post-treatment (30-40% by area).

In comparison, ligation + radiation tumours showed significant edema (20-40% by area) in the samples 14 days post-treatment. Samples 1 day post-treatment did not show significant edema (5% by area). Chi-square tests did not show a significant increase in glycogen accumulation ($p = 0.07$) at 1 day post-treatment, but did show a significant increase by 14 days post-treatment ($p < 0.0001$). PAS scores for ligation-only and ligation + radiation groups are shown in Figure 7.14. Samples from both time points showed relatively low presence of necrosis (0-20% by area).

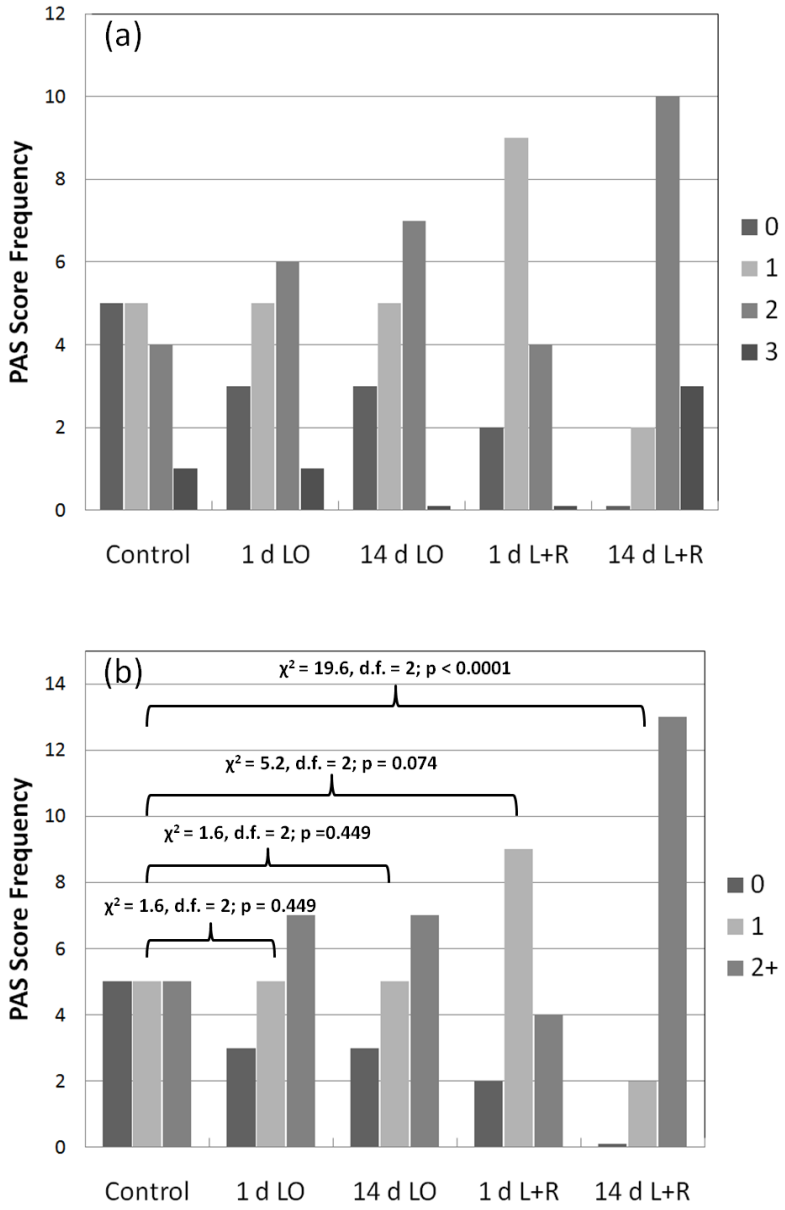

Figure 7.14. Bar charts showing frequency of fields scoring on PAS scoring scale for control and post-treatment cases. Frequencies of all four scoring categories are shown in (a). For χ2-testing, categories 2 and 3 are combined, as shown in (b). Samples taken 14 days after ligation+radiation treatment showed significant changes in scoring pattern, indicating increased glycogen accumulation in these samples.

Patterns of hypoxia did not correlate with treatment. Hypoxia was most elevated in the control tumours sacrificed at large volume, as well as the ligation-only tumours sacrificed 14 days after ligation. The patterns of hypoxia in these cases were noted by the pathologist to be spatially correlated with patterns of necrosis.

7.4 Discussion

Increased necrotic fraction was consistently observed in unirradiated tumours which had reached larger volumes – notably the untreated controls intentionally sacrificed at larger volume, and the ligation-only tumours sacrificed 14 days after application of the ligature. The uninterrupted growth of the ligation-only tumours was shown in Figure 6.1. The observation that areas of necrosis correlated with bound hypoxia marker is consistent with chronic hypoxia in larger tumours being a cause of the necrosis. This increase in necrotic fraction with volume may be a cause of observed increases in ADC and T2 in untreated control tumours, as shown in Figure 7.1.

Several notable pathologies were observed in the tumours treated with radiation alone. A decrease in mitotic cell count is consistent with the observations of Haung *et al* (13). This is also consistent with an observed decrease in tumour growth rate for this treatment group, as was shown in Figure 4.1. Edema in the treated tumours is a plausible mechanism for observed increases in ADC and T2 observed 3 days post-treatment, and the continued

elevation of ADC 14 days post-treatment. A correlation between increased ADC and edema or increased extracellular space has been repeatedly observed (6-9).

Observation of extracellular glycogen accumulation is consistent with previous reports (3,4), and potentially explains the late decreases in T2 observed in treated tumours. Although there was significant accumulation of glycogen 3 days post-treatment, when T2 was elevated, the accumulation by 14 days post-treatment was significant relative to the 3 day time-point. Accumulation of similar glycogen granules has been shown to cause decreased T2 in diseased liver (15). This is consistent with the idea that water bound to large macromolecules experiences a greatly shortened T2.

The findings of this study were not able to explain the decrease in T2 observed in the ligation-only group 1 day after application of the ligature. There did not seem to be significant edema or glycogen accumulation in either the ligation-only or ligation + radiation groups 1 day post-treatment. The possibility of increased presence of RBCs being a cause of these decreases, as was observed by Henning *et* al (9), was considered, but was ultimately not supported by the pathological observations of these tumours.

The observation of edema and glycogen accumulation in the ligation + radiation samples 14 days post-treatment are consistent with the observed pathology of the radiation-only group at this time point. This observation also supports the hypotheses of edema being responsible for sustained ADC

elevation, and later T2 depression, based on observed ADC and T2 responses at this time point.

The use of only three tumour samples at each time point is a limitation of this analysis. These results, however, are still useful in that they illuminate several plausible explanations of observed ADC and T2 behaviors. Significant edema in radiation-treated tumours suggests that it plays an important role in both ADC and T2 changes post-treatment. Post-treatment accumulation of extracellular glycogen may explain decreases in tumour T2 several days after treatment. These data help to put the results of this dissertation in context and suggest future directions for research into the understanding of the mechanisms behind ADC and T2 behaviors in post-treatment tumour tissue.

References

1. Bancroft JD, Cook HC. Manual of histochemical techniques and their diagnostic application. New York, NY: *Churchill Livingstone*; 1994.

2. Bancroft JD, Gamble M. Theory and practice of histological techniques. 6th ed. Philadelphia, PA: *Churchill Livingstone Elsevier*; 2008.

3. Miquel J, Haymaker W. Astroglial reactions to ionizing radiation: with emphasis on glycogen accumulation. In de Robertis EDP, Carrea R, editors. Biology of Neuorglia: Progress in Brain Research. New York, NY: *American*

Elsevier Publishing Company, Inc.; 1963. p. 89-114.

4. Miquel J, Klatzo I, Menzel DB, Haymaker W. Glycogen changes in x-irradiated rat brain. *Acta Neuropathol.* 1963: p. 482-490.

5. Le Bihan D. Molecular diffusion, tissue microdynamics and microstructure. *NMR in Biomed.* 1995: p. 375-386.

6. Chenevert TL, McKeever PE, Ross BD. Monitoring early response of experimental brain tumors to therapy using diffusion magnetic resonance imaging. *Clin. Cancer Res.* 1997: p. 1457-1466.

7. Chenevert TL, Stegman LD, Taylor JMG, Robertson PL, Greenberg HS, Rehemtulla A, et al. Diffusion magnetic resonance imaging: an early surrogate marker of theapeutic efficacy in brain tumors. *J. Natl. Cancer Inst.* 2000: p. 2029-2036.

8. Lee KC, Moffat BA, Schott AF, Layman R, Ellingworth S, Juliar R, et al. Prospective early response imaging biomarker for neoadjuvant breast cancer chemotherapy. *Clin. Cancer Res.* 2007: p. 443-450.

9. Henning EC, Azuma C, Sotak CH, Helmer KG. Multispectral quantification of tissue types in a RIF-1 tumor model with histological validation. Part I. *Mag. Reson. Med.* 2007: p. 501-512.

10. Mitchell DG, Burk DLJ, Vinitski S, Rifkin MD. The biophysical basis of tissue contrast in extracranial MR imaging. *Am. J. Roentgenol.* 1987: p. 831-837.

11. Rofstad EK, Steinsland E, Kallhus O, Chang YB, Hovik B, Lyng H. Magnetic resonance imaging of human melanoma xenografts in vivo: proton spin-lattice and spin-spin relaxation times versus fractional tumour water content and fraction of necrotic tumour tissue. *Int. J. Radiat. Biol.* 1994: p. 387-402.

12. Nishimura DG. Principles of Magnetic Resonance Imaging Palo Alto, CA: *Stanford University Press*; 1996.

13. Huang MQ, Pickup S, Nelson DS, Qiao H, Xu HN, Li LZ, et al. Monitoring response to chemotherapy of non-Hodgkin's lymphoma xenografts by T2-weighted and diffusion-weighted MRI. *NMR in Biomed.* 2008: p. 1021-1029.

14. Daly LE, Bourke GJ. Interpretation and uses of medical statistics. 5th ed. Oxford, UK: *Blackwell Science Ltd.*; 2000.

15. Kirota S, Sugimoto K, Matsumoto S, Kono M, Harada Y. MR imaging of the liver and complicating hepatic tumors in type Ia glycogen storage disease. *Int. J. Clin. Oncol.* 1997: p. 1-5.

Chapter 8: Conclusions

A 9.4 T MRI system was used to serially measure the ADC and the T2 of human GBM tumours grown as xenografts in NIH-iii nude mice. Measurements were taken before, and at multiple points after, treatment of the tumours with 200 kVp x-rays. Multiple experiments were used to characterize the response of tumour ADC and T2 to treatment.

In chapter 4 the temporal and dose dependence of mean tumour ADC and T2 were measured after a single fraction of radiation. Delivered dose ranged from 50 cGy to 800 cGy, with an untreated control group also measured. There was clear dose dependence to the observed ADC response. The observed ADC response was negatively correlated with post-treatment growth rate. For the highest dose group, maximum ADC response was measured seven days post-treatment, where the ADC peaked 22% higher than the pre-treatment value.

Relative T2 peaked 7.5% above the pre-treatment value, and had transitioned to a state of reduced T2 by 14 days post-treatment, where T2 had dropped to 7.9% below the pre-treatment value.

In chapter 5 tumour treatment was expanded beyond single fractions to include treatments involving two and three fractions, with fraction spacings of 24 or 72 hours. In all cases a total dose of 800 cGy was used. Fractionation did not have a statistically significant effect on the maximum ADC response. For all groups, the maximum ADC response was measured seven days after delivery of the final treatment fraction. In all groups, an initial post-treatment increase in T2 was seen, followed by a transition to depressed T2. The time of transition ranged from 3.5 to 7.5 days after the final fraction of treatment.

The work presented in chapter 6 examined the effect of radiosensitivity changes on ADC and T2 response. A state of reduced oxygenation was induced in tumours using an externally-applied, suture-based ligature. Two control groups were used – a group receiving no intervention, and a group which had a ligature applied, but were not irradiated. When compared to the same tumours treated under normal conditions, the hypoxic tumours showed a reduced sensitivity to radiation as measured by both post-treatment growth rate and changes in mean tumor ADC. The T2 response of the tumors to radiation was complicated by a negative T2 response in the ligated, but unirradiated tumours. The demonstration of ADC sensitivity to radiobiologically-induced variations in

response is important as hypoxia is an extremely important prognostic indicator in the clinic. These results suggest that interpretation of ADC data in clinical patients would be improved with some understanding of the oxygenation status of the tumour.

In chapter 7 the pathophysiological nature of the ADC and T2 responses seen in the previous chapters is investigated. Treated and untreated tumours were dissected at various time points, and microscope slides prepared. All slides were reviewed by a pathologist in a blinded manner. Increases in necrotic fraction were observed in tumours growing significantly beyond their pretreatment volumes. This increase in necrotic fraction may explain late increases in ADC and T2 in the untreated controls. Edema was observed in radiation-treated tumours, which may explain early increases in ADC and T2, as well as sustained ADC elevation until at least 14 days post-treatment. Granules of glycogen accumulated in the extracellular space of treated tumours, with the accumulation being greater 14 days post-treatment compared to 3 days post-treatment. The presence of glycogen may explain why depressed T2 was observed at later post-treatment time points.

This work is significant in that it adds to the body of literature that describes tumour ADC and T2 response to anticancer therapy, and adds to the understanding of ADC and T2 response to radiation therapy in particular. This

data supports other work that suggests the use of ADC and T2 as biomarkers for tumour response to treatment.